SYNTHESIS AND CHARACTERIZATION OF RARE EARTH-BASED MAGNETOCALORIC PHASES

SYNTHESIS AND CHARACTERIZATION OF RARE EARTH-BASED MAGNETOCALORIC PHASES

By

FANG YUAN, B.Sc, M.Sc.

A Thesis

Submitted to the School of Graduate Studies

in Partial Fulfillment of the Requirements

For the Degree

Doctor of Philosophy

McMaster University

Doctor of Philosophy (2017) McMaster University

(Chemistry) Hamilton, Ontario

TITLE: Synthesis and Characterization of Rare Earth-based Magnetocaloric Phases

AUTHOR: Fang Yuan

SUPERVISOR: Dr. Yurij Mozharivskyj

NUMBER OF PAGES: xxiii, 180

Abstract

In search of novel magnetocaloric materials, a number of rare earth-based phases were designed, synthesized and investigated. These compounds were prepared by arc-melting or sintering, followed by annealing at high temperature to obtain phase-pure materials. Single crystal and powder X-ray diffraction were employed for phase identification, purity assessment, structure solution and refinement. Energy dispersive X-ray spectroscopy (EDS) was used to determine sample compositions. A Quantum Design SQUID magnetometer equipped with an alternating current (ac) transport controller (model 7100) was employed to measure magnetic data and evaluate magnetocaloric properties. The crystal structure and physical properties were analyzed via electronic structure calculations.

In this thesis work, the RE_5Ga_3 and $RECo_2$ (*RE* = rare earth) materials were chosen as a starting point for structural modifications. Specifically, substitution of Co for Ga (and vice versa) or rare earth replacement was used to design new materials. In total, four families were investigated: $Ho_5Ga_{3-x}Co_x$ (x = 0, 0.1, 0.2, 0.3, 0.4, 0.5, 1), $Er_5Ga_{3-x}(Fe/Co)_x$ (x = 0, 0.4), $RE(Co_{0.667}Ga_{0.333})_2$ (*RE* = Gd, Tb, Dy, Ho, and Er), and $Gd(Co_{1-x}Ga_x)_2$ (x = 0, 1/6, 1/3, 1/2, 2/3, 5/6, and 1). The samples were prepared by arc-melting, wrapped in Ta foil, sealed in evacuated silica tubes and annealed at temperatures higher than 800 ^oC.

The $Ho_5Ga_{3-x}Co_x$ and $Er_5Ga_{3-x}(Fe/Co)_x$ systems features a Mn_5Si_3-type-to-Cr_5B_3-type structural transformation, driven by geometric factors. On the other hand, the

structural transformation in the *RE*($Co_{0.667}Ga_{0.333}$)$_2$ and Gd($Co_{1-x}Ga_x$)$_2$ systems appears to be controlled by the valence electron count (VEC). The *RE*($Co_{0.667}Ga_{0.333}$)$_2$ (*RE* = Gd, Tb, Dy, Ho, and Er) phases adopt a hexagonal $MgZn_2$-type structure ($P6_3/mmc$). Structural and magnetic properties of the $MgZn_2$-type *RE*($Co_{0.667}Ga_{0.333}$)$_2$ materials were investigated via single crystal and powder X-ray diffraction, powder neutron diffraction (PND), and magnetic measurements. In addition to the hexagonal $MgZn_2$-type structure, four other structures were discovered in the Gd($Co_{1-x}Ga_x$)$_2$ system: cubic $MgCu_2$- ($Fd\bar{3}m$), orthorhombic MgSrSi- (*Pnma*), orthorhombic $CeCu_2$- (*Imma*), and hexagonal AlB_2-type structure (*P*6/*mmm*). When Ga content increases, the structure moves from a "condensed cluster-based arrangement" to a "3D Network" to a "2D Network". Meanwhile, coordination number (CN) of Co or Ga atoms changes from 6 to 4, and then to 3.

Magnetic properties of many of the *RE*-based phases were evaluated via temperature- and field-dependent magnetization measurement. $Ho_5Ga_{2.7}Co_{0.3}$, $Ho_5Ga_{2.6}Co_{0.4}$, and Gd($Co_{0.667}Ga_{0.333}$)$_2$ exhibited a sharp ferromagnetic transition and their MCE in terms of the isothermal magnetic entropy change, ΔS_{mag}, was explored. Unfortunately, relatively low ΔS_{mag} values suggest a conventional magnetocaloric effect and absence of first-order coupled magnetostructural transitions.

Preface

Chapter 1 of this dissertation is an introduction to magnetism and magnetocaloric effect (MCE). It starts with the background of magnetism and outlines different magnetic phenomena, origin of magnetism, and theoretical treatment of different magnetic behaviors. Next, the history of magnetocaloric effect (MCE) and magnetic refrigeration is presented. Conventional MCE, giant MCE and mechanism of magnetic refrigeration are examined. The current status of magnetocaloric research is also summarized; advantages and disadvantages of the present magnetocaloric materials are analyzed. Lastly, materials researched in this work are discussed.

Chapter 2 describes the experimental techniques used and outlines the role of each technique for the material study. Chapter 3-5 present the results on the *RE*-based magnetocaloric materials. The three chapters are papers that are either published or to be submitted to a peer-reviewed journal. In particular, Chaper 3 looks at the phase transition, magnetic and magnetocaloric properties in the $Ho_5Ga_{3-x}Co_x$ (x = 0, 0.1, 0.2, 0.3, 0.4, 0.5, 1) and $Er_5Ga_{3-x}(Fe/Co)_x$ (x = 0, 0.4) systems. The research results were published in the Journal of Alloys and Compounds (*J. Alloys Comp.* **2015,** 620, 376–382). Chapter 4 introduced a few new hexagonal Laves phases: $MgZn_2$-type $RE(Co_{0.667}Ga_{0.333})_2$ (*RE* = Gd, Tb, Dy, Ho, and Er). The structural characteristics and magnetic properties of $RE(Co_{0.667}Ga_{0.333})_2$ (*RE* = Gd, Tb, Dy, Ho, and Er) were investigated through X-ray diffraction and magnetic measurements, respectively. Chapter 5 looks into the factors responsible for the structural transformation in the $Gd(Co_{1-x}Ga_x)_2$ series (x = 0, 1/6, 1/3,

1/2, 2/3, 5/6, and 1). By varying Co/Ga ratio, five structures were obtained in the $Gd(Co_{1-x}Ga_x)_2$ system. The electronic structure calculations suggest that changes in the valence electron counts (VEC) promote the sequential transitions in $Gd(Co_{1-x}Ga_x)_2$.

As a conclusion, Chapter 6 lists the summary of the important characteristics of the investigated materials in terms of the composition, structures, and physical properties. Future studies to improve the magnetocaloric effect in the existed materials, as well as to develop the new materials, are proposed.

In Appendix, structural and physical property studies on Ta_5P_3 (*P* = Si and Ge) and preliminary neutron powder diffraction studies on $RE(Co_{0.667}Ga_{0.333})_2$ (*RE* = Ho and Er) are presented. The results on Ta_5P_3 (*P* = Si, and Ge) have been published in the Journal of Alloys and Compounds. The Cr_5B_3-type Ta_5Ge_3 was obtained by sintering the Ta and Ge powders, while the Cr_5B_3-type Ta_5Si_3 phase was synthesized by arc-melting Ta and Si pieces. The magnetization and electrical resistivity were measured; electronic structure calculations were employed to clarify the relationship between the composition and physical properties. Neutron diffraction studies on the $MgZn_2$-type $RE(Co_{0.667}Ga_{0.333})_2$ (*RE* = Ho and Er) were used to refine the Co/Ga occupancies and determine the ground magnetic state of these Laves phases. The magnetic structure of $Ho(Co_{0.667}Ga_{0.333})_2$ is significantly different from that of $Er(Co_{0.667}Ga_{0.333})_2$. Co magnetic moments are absent in $RE(Co_{0.667}Ga_{0.333})_2$, which contracts with the results for the cubic $RECo_2$ phases. In addition, some interesting small angle neutron scattering (SANS) was discovered.

Acknowledgement

There are a lot of people that I want to express my thankfulness. In the first place, my supervisor, Dr. Yurij Mozharivskyj, who allows me to study and work in his group. Thanks him for always being greatly patient and nice with me when experimental results failed to be the expected ones. And I appreciate him so much for all the guidance, encouragement and helpfulness over the years of my study at McMaster University. Also, I want to offer great gratefulness to my supervisory committee members, Dr. John Greedan and Dr. Gillian Goward, thanks both of them for the invaluable helpfulness and suggestions through my graduate study.

I would like to thank the former group members Dr. Jinlei Yao, Dr. Peng Wang and Ms. Yan Yin Janice Cheung for the training and support during the beginning of my graduate study. I am so grateful to all my current research group members, thank you so much for all the support and helpfulness in my study, as well as in the daily life. Great thankfulness to all our collaborators, especially Dr. Alex V. Morozkin, Dr. Krishna Kumar Ramachandran, Dr. Asa Toombs, Dr. Gordon J Miller, and Dr. Volodymyr Svitlyk, several papers would not be published without your wisdom and insight. I am very grateful to all the member of the BIMR, Especially Dr. Paul Dube, Dr. Hanna Dabkowska, Dr. Anton Dabkowski, Dr. Jim Britten and Mr. Jim Garrett, for all the support and assiatance.

Special thanks to all of my dear friends and family for their support, companionship, and encouragements. Whenever I doubt my abilities or feel frustrated,

you can always help me out of the situation and regain confidence in my research and life. And of course, without the understanding and assistance of my family, especially my grandparents, parents, and boyfriend, it is definitely impossible to achieve my goals. Thanks you so much for raising me up, even to more than I could be by myself.

Table of Contents

List of Figures

List of Tables

Chapter 1. Introduction

1.1 Magnetism

Magnetism has attracted attention for millennia. Magnetism is intrinsic to all materials and exhibits itself with an applied magnetic field.

1.1.1 Magnetic Field

Magnetic fields arise from magnetic dipoles. Magnetic monopoles do not exist, all magnets have both a south and a north pole. The Earth itself can be treated as a giant bar magnet.

The pole strength, *p*, is introduced to describe magnetic poles of magnets. One magnetic pole will interact with another one and the force, *F*, between them can be formulated as:

$$F = \frac{p_1 p_2}{4\pi\mu_0 r^2} \tag{1.1}$$

where *p* is the pole strength, μ_0 is the permeability of free space, and *r* is distance between the two magnetic poles. To better understand the interaction force, Equation 1.1 could be rewritten as

$$F = \left(\frac{p_1}{4\pi\mu_0 r^2}\right) p_2 = \boldsymbol{H} p_2 \tag{1.2}$$

where $\boldsymbol{H}$ is the magnetic field generated by the first magnetic pole, p_1. On the other hand, the interaction force can be rewritten as:

$$F = \left(\frac{p_2}{4\pi\mu_0 r^2}\right) p_1 = \boldsymbol{H} p_1 \tag{1.3}$$

where $\boldsymbol{H}$ is the magnetic field generated by the second magnetic pole, p_2. Therefore, the magnetic field of a magnetic pole, p, is defined as:

$$\boldsymbol{H} = \left(\frac{p}{4\pi\mu_0 r^2}\right) \tag{1.4}$$

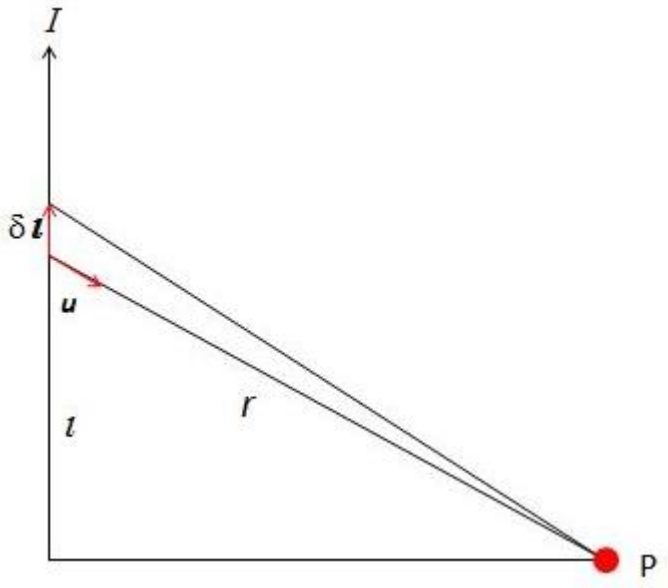

Figure 1.1. Magnetic field at point P generated by a straight wire with a current of *I* (Biot-Savart law).

Magnetic field can also be generated by electrical currents. There are two methods to calculate the magnetic field of an electrical circuit: Biot-Savart law and Ampère's

circuital law. The Biot-Savart law gives the magnetic field contribution, $\delta \boldsymbol{H}$, of a conductor with a current of I at the distance of r:

$$\delta \boldsymbol{H} = \left(\frac{I}{4\pi r^2} \right) \delta \boldsymbol{l} \times \boldsymbol{u} \tag{1.5}$$

where $\delta \boldsymbol{l}$ is limited length of the conductor, and $\boldsymbol{u}$ is the unit vector (**Figure 1.1**).

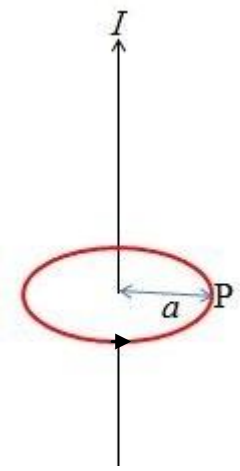

Figure 1.2. The magnetic field at *P* point generated by a long straight wire with a current of *I*.

Amp*è*re's circuital law can be expressed as:

$$\oint \boldsymbol{H} \cdot d\boldsymbol{l} = I \tag{1.6}$$

where I is the current through the circuit and $d\boldsymbol{l}$ is the unit vector along a closed path. The Amp*è*re's circuital law is equivalent to the Biot-Savart law, but can be more easily applied to some electric circuit with a particular symmetry. A long straight wire with a

current of I is a better example. The magnetic field at a point P with a distance of a from the long wire can be obtained via Ampère's circuital law (**Figure 1.2**):

$$\boldsymbol{H} = \frac{I}{2\pi a} \tag{1.7}$$

Biot-Savart law gives the same result, but the solution is more complicated. Equation 1.6 defines the unit of magnetic field as A/m in SI system, while it is Oe in the cgs system.

1.1.2 Magnetic Moment

Magnetic moment, $\boldsymbol{\mu}$, can be defined as the moment exerted on either a bar magnet or a current loop under an applied magnetic field. Therefore, there are two different expressions of magnetic moment. For a bar magnet:

$$\boldsymbol{\mu} = pl \tag{1.8}$$

For a current loop:

$$\boldsymbol{\mu} = IA \tag{1.9}$$

where p is the pole strength, l is the length of a bar magnet, I is the current, and A is the area of current loop.

The magnetic moment per unit volume is called magnetization, $\boldsymbol{M}$. When exposed to an external magnetic field $\boldsymbol{H}$, the total response of the material, including the magnetization and external magnetic field, is called magnetic induction B,

$$\boldsymbol{M} = \frac{\boldsymbol{\mu}}{V} \tag{1.10}$$

$$\boldsymbol{B} = \mu_0 (\boldsymbol{H} + \boldsymbol{M}) \tag{1.11}$$

where V is the volume of material.

Both the magnetic field and magnetic moment can be generated by either magnets or electrical circuits carrying current. It is reasonable to conclude that there is a close relationship between the two different sources. In search of this relationship, Ampère found a electrical current loop is equivalent to a small magnet with magnetic poles. In turns, the magnetic field of magnets is caused by special "molecular current". This is remarkably important for discovering the origin of magnetism, which will be discussed later.

1.1.3 Origin of Magnetism

The magnetism of an atom arises from the electrons, although nuclei also have magnetic moments. And the properties of an electron are determined by five quantum numbers: principal quantum number n, orbital angular momentum quantum number l, orbital magnetic quantum number m_l, spin angular momentum quantum number s, and spin magnetic quantum number m_s. s is ½ and m_s can be +½ or -½, while the other three quantum numbers are integers and follow some compulsory rules: 1) $n \geq 1$; 2) $0 \leq l \leq n\text{-}1$; 3) $-l \leq m_l \leq l$. The total angular momentum of an electron is composed of orbital ($\boldsymbol{l}$) and spin ($\boldsymbol{s}$) angular momenta.

$$|\boldsymbol{l}| = \sqrt{l(l+1)}\,\hbar \tag{1.12}$$

where $|\boldsymbol{l}|$ is the magnitude of the orbital angular momentum, and ħ is Dirac constant.

$$|\boldsymbol{s}| = \sqrt{s(s+1)}\,\hbar \tag{1.13}$$

where $|\boldsymbol{s}|$ is the magnitude of the spin angular momentum. Based on the classic point of view, the orbital and spin motions of an electron generate the orbital (μ_l) and spin (μ_s) magnetic moments, respectively. In addition, $\boldsymbol{l}$, $\boldsymbol{s}$, μ_l and μ_s will be quantized along the orientations of magnetic field. (**Figure 1.3**)

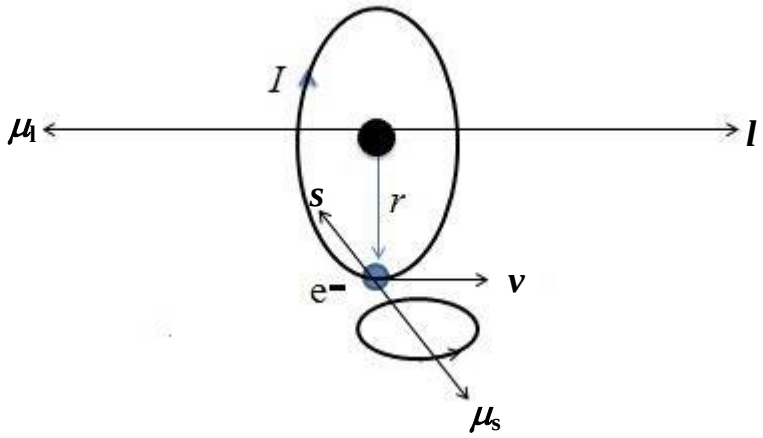

Figure 1.3. The orbital angular momentum ($\boldsymbol{l}$), spin angular momentum ($\boldsymbol{s}$), orbital magnetic moment (μ_l), and spin magnetic moment (μ_s) of an electron (e^-), where *r*, $\boldsymbol{v}$, and *I* are orbiting radius, speed, and current, respectively.

A moving electron around a nucleus is equivalent to a circulating current *I*. if *r* denotes the orbital radius of the electron,

$$I = \frac{ev}{2\pi r} \tag{1.14}$$

$$A = \pi r^2 \tag{1.15}$$

where *v* and *e* is the velocity and charge of the electron, respectively. Therefore, the orbital magnetic moment of the electron can be deduced by Equation 1.9,

$$\boldsymbol{\mu_l} = \frac{evr}{2} \tag{1.16}$$

The orbital angular momentum of the electron equals $m_e vr$, here m_e is the mass of the electron, combining Equation (1.12),

$$m_e vr = \sqrt{l(l+1)}\hbar \tag{1.17}$$

The velocity, *v*, is equal to

$$v = \frac{\sqrt{l(l+1)}\hbar}{m_e r} \tag{1.18}$$

Therefore Equation (1.16) will be

$$\boldsymbol{\mu_l} = \frac{e\sqrt{l(l+1)}\hbar}{2m_e} \tag{1.19}$$

The natural unit of magnetic moment arising from the orbital or spin angular momentum is called Bohr magneton, μ_B, which is a positive physical constant.

$$\mu_B = \frac{e\hbar}{2m_e} \tag{1.20}$$

Therefore, the magnetic moment of orbital angular momentum can be written as:

$$\boldsymbol{\mu_l} = \mu_B \sqrt{l(l+1)} \tag{1.21}$$

The quantized projection of the orbital magnetic moment onto the magnetic field axis is:

$$\boldsymbol{\mu_l} = \mu_B m_l \tag{1.22}$$

Analogous to the orbital magnetic moment, the magnetic moment originating from the spin angular momentum is

$$\boldsymbol{\mu_s} = g_e \mu_B \sqrt{s(s+1)} \tag{1.23}$$

The quantized projection of the spin magnetic moment along the direction of applied magnetic field is

$$\boldsymbol{\mu_s} = g_e \mu_B m_s \tag{1.24}$$

where g_e is the g-factor of an electron, which is approximately 2. In fact, most elements have more than one electron, so the spin and orbital angular momenta will interact with each other, which is called spin-orbit coupling. Eventually, the total angular momentum will be formed. For all the filled shells, the total angular momentum equals to zero and there is no contribution to the magnetic moment. As a result, atoms with all shells filled by electrons are diamagnetic.

To form the total angular momentum, the electrons in the incomplete shells will interact via either *S*-*L* or *j*-*j* coupling. In light atoms such as 4*f* and 3*d* elements, the coupling between individual orbital angular momenta and the individual spin angular momenta is very strong. Therefore, the total spin angular momenta, ***S***, and the total orbital angular momenta, ***L***, are formed by combining all the individual orbital angular momenta and all the individual spin angular momenta, respectively. Then the total angular momenta, ***J***, is formed from the coupling of ***S*** and ***L*** (Equation 1.25).

$$\boldsymbol{J} = \boldsymbol{L}+\boldsymbol{S}, \boldsymbol{L}+\boldsymbol{S}-\mathbf{1}, \ldots, |\boldsymbol{L}-\boldsymbol{S}| \tag{1.25}$$

Therefore, the total angular momentum, ***J***, is,

$$|\boldsymbol{J}| = \sqrt{J(J+1)}\,\hbar \tag{1.26}$$

here $|\boldsymbol{J}|$ is the magnitude of the total angular momentum, *J* is the total quantum number.

The total magnetic moment, $\boldsymbol{\mu_J}$, can be obtained by analogy with the orbital magnetic moment,

$$\boldsymbol{\mu_J} = g_J \mu_B \sqrt{J(J+1)} \tag{1.27}$$

And the quantized projection of the total effective magnetic moment along the direction of the applied magnetic field is,

$$\boldsymbol{\mu_J} = g_J \mu_B m_J \tag{1.28}$$

where m_J = *-J, -J+1, …, J* and $g_J = \frac{3}{2} + \frac{S(S+1)-L(L+1)}{2J(J+1)}$ is the Lande *g*-factor.

In heavy atoms like actinides, the coupling between the spin and orbital angular momenta of individual electrons is much stronger than the coupling between angular momentum of different electrons. Firstly, an individual total angular momentum, $\boldsymbol{j_i}$, will be formed for each electron. In the next step, the individual $\boldsymbol{j_i}$s interact with each other to form a total angular momentum, ***J*** (Equation 1.29).

$$\boldsymbol{J} = \sum_i \boldsymbol{j_i} \tag{1.29}$$

1.1.4 Classification of Magnetization

When an external magnetic field is applied, materials will experience magnetization. Depending on the orientation and quantities, the magnetization of most materials can be classified into five common types: diamagnetism, paramagnetism, ferromagnetism, antiferromagnetism, and ferrimagnetism. The susceptibility, χ, is introduced to describe the magnetic response when exposed to an external magnetic field.

$$\chi = \frac{\boldsymbol{M}}{\boldsymbol{H}} \tag{1.30}$$

Diamagnetism is intrinsic to all materials. However, diamagnetism is so weak that it can be easily masked by other competing magnetic behaviors in a material. Therefore, only materials with no unpaired electrons display diamagnetic response. Diamagnetic effect could be attributed to the change of orbital angular momentum, which creates an additional magnetic moment. By Lenz's law, the additional magnetic moment arising from the diamagnetic effect opposes the external magnetic field, so the diamagnetic susceptibility has a negative value. Each electron in a many electron atom contributes to the diamagnetic response by virtue of its orbital motion.

On the other hand, all of the materials with net magnetic moment due to the unpaired electrons exhibit a positive susceptibility. The magnetic state with a weak coupling between the neighboring magnetic moment is called paramagnetism. Otherwise, it could be ferromagnetism, antiferromagnetism, or ferrimagnetism. (**Figure 1.4**). By plotting the $1/\chi$-T curves, the significant differences could be observed between ferromagnetism, antiferromagnetism, ferrimagnetism, and paramagnetism. (**Figure 1.5**)

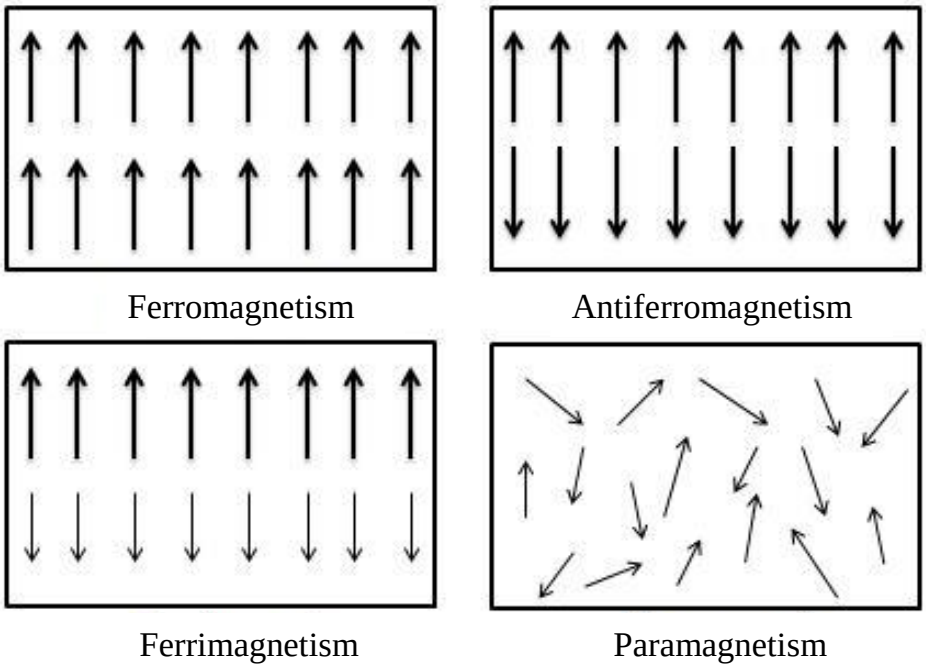

Figure 1.4. Four basic magnetisms with the positive susceptibility.

Paramagnetism is very common, and occurs in all the paramagnetic materials, or ferrimagnetic and ferromagnetic materials above the Curie temperature (T_C), or antiferromagnetic materials above the Neel temperature (T_N). In paramagnetic materials with localized magnetic moments susceptibility follows the Curie law (Equation (1.31)), or the Curie-Weiss law (Equation (1.32**)**).

$$\chi = \frac{C}{T} \tag{1.31}$$

$$\chi = \frac{C}{T - \theta} \tag{1.32}$$

where C and θ are the proportionality constant and the Weiss temperature, respectively.

Actually, the Curie law can be seen as a specific example of Curie-Weiss law with a Weiss temperature of zero. The θ temperature represents the magnetic (i.e. exchange) interactions in the paramagnetic state and is negative for antiferromagnetism and ferrimagnetism, while it is positive for ferromagnetism. Therefore, θ could be used to distinguish the antiferromagnetism and ferrimagnetism from the ferromagnetism. However in case of the rare-earth containing materials, the θ temperature represents rather the crystal field effects than the exchange interactions.

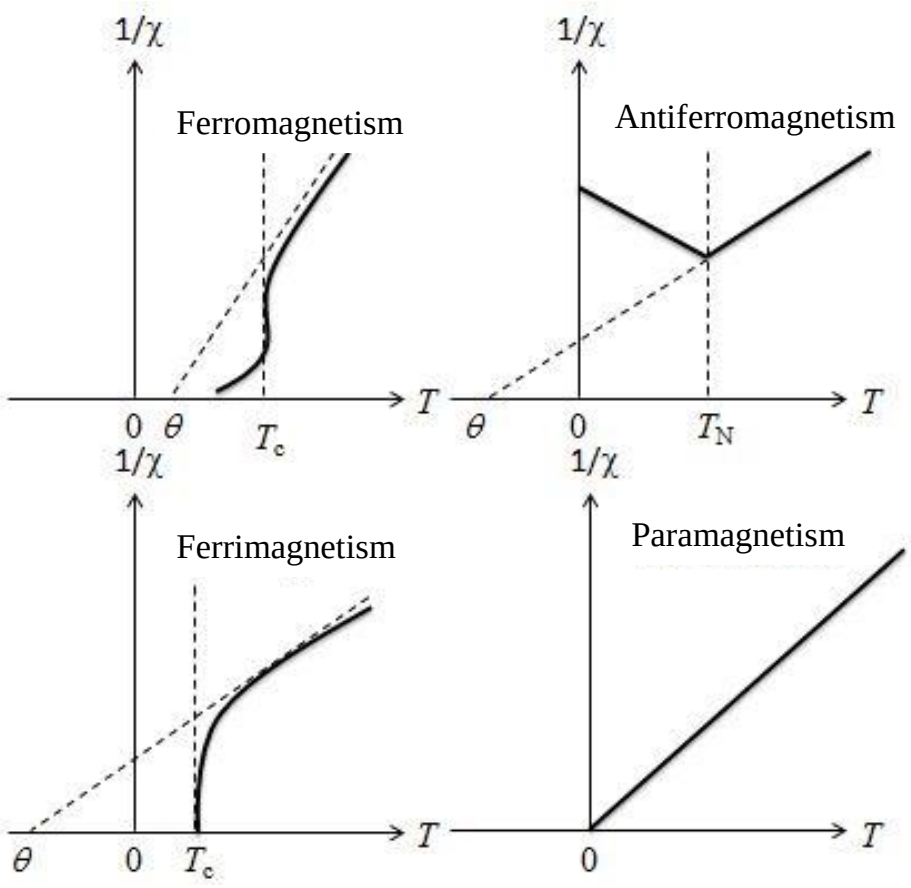

Figure 1.5. The inverse susceptibility of four basic magnetisms with the positive susceptibility.

A magnetic state for which all the magnetic moments align parallel to each other under an applied magnetic field is called ferromagnetism. Ferromagnetism only exists with the presence of the spontaneous magnetization below Curie temperature. On the other hand, the magnetic moments start to orient in the random directions due to the thermal disorder above T_C, therefore, the ferromagnetic materials become paramagnetic. In ferromagnetic state, the susceptibility is a few orders higher than that of the paramagnetic state.

Antiferromagnetism is a state in which the adjacent moments couple antiparallel to each other, in other words, it is composed of two magnetic sublattices with the opposite magnetizations. Herein, the two magnetic sublattices are both spontaneously magnetized but in the opposite direction, therefore, the net magnetization is nearly zero due to the same amount of magnetization in the two sublattices. A Néel temperature is the critical temperature above which the spontaneous magnetization is destroyed by the thermal disorder and the material becomes paramagnetic. Below T_N, the susceptibility increases with the increase of temperature, and is determined by the relative directions of the external magnetic field and spontaneous magnetizations in the magnetic sublattices. For powder samples with randomly oriented crystallites, the susceptibility is the average of the vector addition of the magnetizations of crystallites in all the possible directions,

$$\chi = \frac{1}{3}\chi_{||} + \frac{2}{3}\chi_{\perp} \tag{1.33}$$

where $\chi_{||}$ and $\chi_{\perp}$ is the parallel and vertical magnetic susceptibility, respectively.

Ferrimagnetism is closely related to both ferromagnetism and antiferromagnetism. For one thing, ferrimagnetism has a spontaneous magnetization similar to that in ferromagnetism below the critical temperature, T_C. On the other hand, the adjacent magnetic moments are aligned antiparallel like in antiferromagnetism. But the amount of magnetizations along the two opposite directions are not identical, therefore, the net magnetization is present.

Five magnetic behaviors were introduced in this section. In terms of susceptibility, the values of paramagnetism and diamagnetism are very small due to the absence of spontaneous magnetization. On the other hand, the other three magnetic responses are significant, and among them, the ferromagnetism is typically the strongest.

1.1.5 Magnetic Exchange

In a paramagnetic state, magnetic moments do not interact with each other at any temperature, but partial ordering of magnetic moments can be obtained with the application of magnetic field. To form a ferromagnetic, ferrimagnetic, or antiferromagnetic state, the neighboring magnetic moments need couple to each other. There are three ways to realize the coupling: direct, superexchange, and indirect exchange interaction. The direct exchange interaction suggests that coupling between nearest neighbor magnetic moment occurs directly, which is usually found in pure 3*d* transition metals, i.e. Fe, Co, Ni, Cr, and etc. The superexchange interaction is the coupling between nearest neighbor magnetic moments through a non-magnetic anion. It occurs commonly in magnetic oxides, where magnetic ions couple to each other via O^{2-} ions. The indirect

exchange interaction is a conduction electron-mediated one, which is called RKKY[1–3] interaction and commonly occurs in metallic *RE*-based magnetic materials.

For metallic *RE*-based magnetic materials involving the RKKY interaction, exchange interaction exists between the localized 4*f* electrons of magnetic ions and the itinerant conduction electrons, which unbalances the spins of other ions. The imbalance decreases oscillatorily with the increase of distance from the magnetic ion. A given ion experiences a sum interaction arising out of all the surrounding ions. In the molecular field approximation Weiss constant, θ, could be used to measure the interaction experienced by a given ion. De Gennes[4] derived the expression of θ for magnetic systems with RKKY interaction:

$$\theta = -\left[\frac{3\pi Z\Gamma^2\left(g_J-1\right)^2 J(J+1)}{4kE_F}\right]\sum F(x) \qquad (1.34)$$

Where Z is number of conduction electrons, Γ the effective exchange integral, E_F is the free electron Fermi energy, $\sum F(x)$ is the quantity obtained by summing all the RKKY function. Ordering temperature, i.e. T_N and T_C, should be identical with θ in the molecular field approximation. Therefore, magnetic ordering is ferromagnetic if $\sum F(x)$ is negative, while it is antiferromagnetic if $\sum F(x)$ is positive.

1.2 Magnetocaloric Effect

The advent of environmental awareness in the past few decades has increased the attention to minimizing the use of chemicals and techniques harmful to environment, as

well as reducing the energy consumption. As the most commonly-used refrigeration technique nowadays, the conventional vapor-cycle refrigeration has low energy efficiency and the cooling agents used still pose some environmental problems.[5] Therefore, the exploration of the environmentally friendly and more efficient refrigeration methods is of great importance. One promising substitution for the conventional vapor-cycle refrigeration is magnetic refrigeration, which utilizes the magnetocaloric effect (MCE) of materials. Compared with other competing techniques, magnetic refrigeration offers several advantages, i.e. high efficiency, small volume, low noise, little environmental impact, as well as long service life.[6,7]

1.2.1 Discovery of Magnetocaloric Effect

In 1881, Warburg noticed a temperature rise in pure iron with the application of a magnetic field, which was the first discovery of MCE.[8] To understand the mechanism of MCE, studies on the total entropy of a system (S) is required. If an external field is applied adiabatically to a magnetocaloric material, the total entropy change, ΔS, equals zero. S consists of magnetic (S_{mag}), lattice (S_{lat}), and electronic (S_{el}) entropies, therefore, the sum of magnetic entropy (ΔS_{mag}), lattice entropy (ΔS_{lat}), and electronic entropy changes (ΔS_{el}) is zero,

$$\Delta S_{mag} + \Delta S_{lat} + \Delta S_{el} = 0 \qquad (1.35)$$

Since the applied magnetic field aligns the magnetic moments, the magnetic entropy decreases, i.e. ΔS_{mag} has a negative value. As a result, the sum of ΔS_{lat} and ΔS_{el} should be

positive. Using the $(\Delta S_{\text{lat}} + \Delta S_{\text{el}})T_{\text{ad}} = C_p \Delta T_{ad}$ relationship and remembering that C_{p} must be positive, ΔT_{ad} should be positive too. Therefore, the temperature of the system will increase. Otherwise, it will decrease with the removal of applied magnetic field. (**Figure 1.6**).

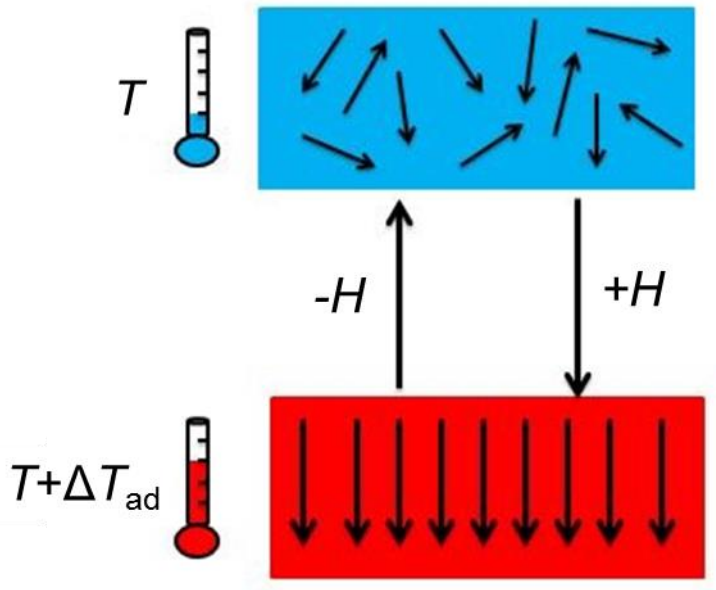

Figure 1.6. The explanatory chart of magnetocaloric effect (MCE).

1.2.2 Two Characteristics of Magnetocaloric Effect

In a magnetocaloric system, both the isothermal entropy change, ΔS_{iso}, and the adiabatic temperature change, ΔT_{ad}, can be used to evaluate the MCE of materials.

1) Under isothermal condition, $\Delta T = 0$, the isothermal entropy change is,

$$(\Delta S_{\text{iso}})_T = \int_{Hi}^{Hf} (\frac{\partial M}{\partial T})_{H,P}\, dH \qquad (1.36)$$

2) Under adiabatic condition, the total entropy change is 0,

$$(\Delta T_{ad})_S = -\int_{Hi}^{Hf} (\frac{T}{C})_{H,P} (\frac{\partial M}{\partial T})_{H,P} \, dH \tag{1.37}$$

where C is the heat capacity under the constant pressure. ΔS_{iso} is an indirect measure of the cooling capacity of magnetocaloric materials, while ΔT_{ad} is an direct measure of the temperature change upon application of magnetic field.

1.2.3 Theories of Conventional Magnetocaloric Effect

In the case of conventional MCE, there is only second-order magnetic transition. The entropy change of conventional MCE is continuous at the transition point (**Figure 1.7**) and can be described by the Boltzmann equation. If the number of possible states is known, the entropy of a system can be calculated,

$$S = R ln \Omega \tag{1.38}$$

where R is the universal gas constant, and Ω is the number of possible states. By analogy, the magnetic entropy can be expressed by the number of all possible magnetic states, Ω_{mag},

$$S_{mag} = R ln \Omega_{mag} = R ln(2J + 1) \tag{1.39}$$

where J is the total quantum number. The S_{mag} values are determined by the number of possible magnetic states, i.e. J. Upon application and removal of magnetic field, the number of possible magnetic states changes, subsequently the magnetic entropy changes as well. Under some limiting conditions, e.g. a ferromagnetic material is subjected to such

a large external magnetic field that all the magnetic moments align in the same direction, the number of possible magnetic states is 1 and the corresponding magnetic entropy equals 0. For such a paramagnetic-to-ferromagnetic ordering, the magnetic entropy change is,

$$\Delta S_{mag} = R(ln1 - ln(2J+1)) = -Rln(2J+1) \quad (1.40)$$

$$(\Delta T_{ad})_S = -\frac{T}{C_{H,P}}(\Delta S_{mag})_T \quad (1.41)$$

Since the paramagnetic-to-ferromagnetic ordering occurs at the Curie temperature, the magnetic entropy change reaches the maximum value.

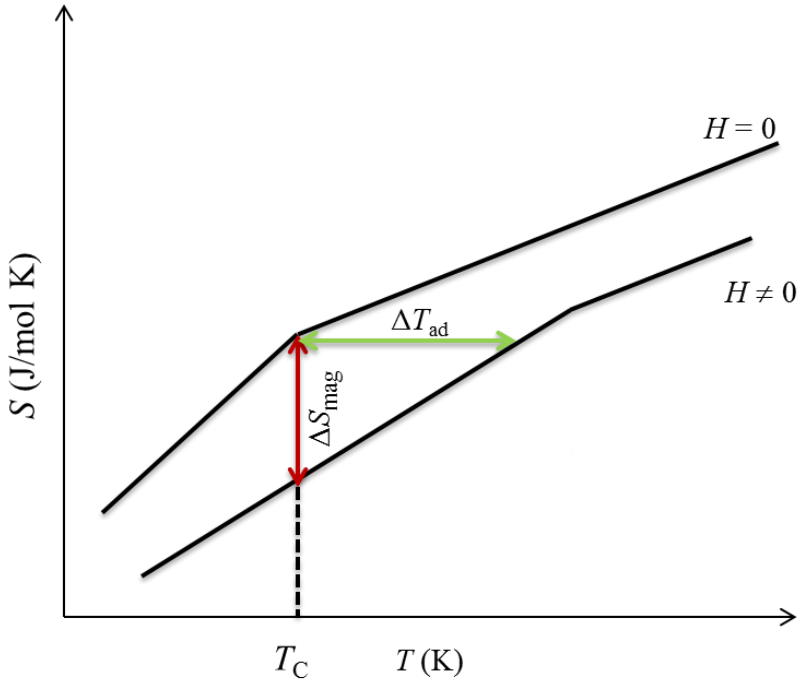

Figure 1.7. The Entropy (*S*) vs. temperature (*T*) and applied magnetic field (*H*) for the conventional MCE.

1.2.4 Theories of Giant Magnetocaloric Effect

If a first-order phase transition associated with the magnetic transition occurs in the magnetocaloric materials, the MCE will be improved significantly, and in this case, it is called giant magnetocaloric effect (GMCE). Compared with conventional MCE, the entropy change is discontinuous at the transition temperatures, i.e. T_{t1} and T_{t2} (**Figure 1.8**). T_{t1} is the transition temperature of first-order phase transition without magnetic field, while T_{t2} is the transition temperature of first-order phase transition under an applied magnetic field (H). In addition, T_{t1} is lower than $T_{t2.}$ Since both of the entropies at T_{t1} and T_{t2} are discontinuous, the isothermal entropy changes between T_{t1} and T_{t2} consist of two parts,

$$\Delta S_{iso} = \int_0^T \frac{C_P(T,H_2)-C_P(T,H_1)}{T} dT - \Delta S(T_{t1}, H=0) \quad (1.42)$$

The enthalpy of a first-order phase transition at T_{t1} is,

$$\Delta E(T_{t1}, H=0) = \Delta S(T_{t1}, H=0) T_{t1} \quad (1.43)$$

Therefore, the isothermal entropy change of GMCE could be rewritten,

$$\Delta S_{iso} = \int_0^T \frac{C_P(T,H)-C_P(T,H=0)}{T} dT - \frac{\Delta E(T_{t1},H=0)}{T_{t1}} \quad (1.44)$$

And the corresponding adiabatic temperature change is,

$$(\Delta T_{ad})_S = -\frac{T}{C_{H,P}} (\Delta S_{iso})_T \quad (1.45)$$

When a first-order phase transition is absent, the enthalpy change equals zero, therefore, the isothermal entropy change is only composed of the magnetic contribution, which is the convenient MCE.

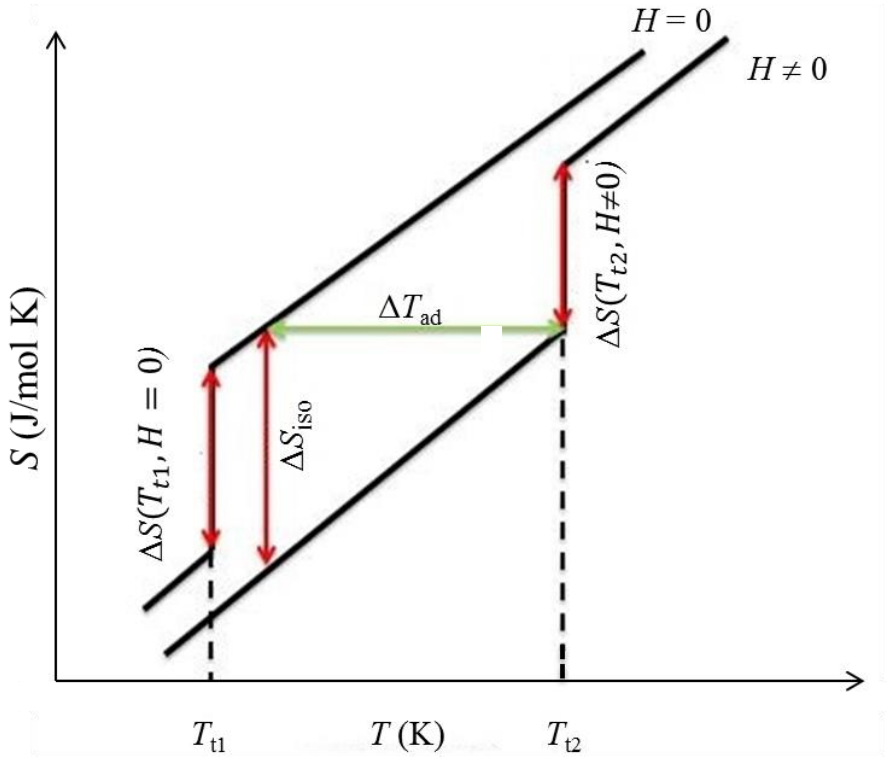

Figure 1.8. The Entropy (*S*) vs. temperature (*T*) and applied magnetic field (*H*) for the giant MCE.

1.2.5 Magnetic Refrigeration

The first MCE-based magnetic refrigeration takes advantage of gadolinium metal as refrigerant, and the corresponding refrigeration efficiency is about 60%.[9] The MCE-based magnetic refrigeration cycle (**left in Figure 1.9**) is analogous to a conventional

vapor-based one (**right in Figure 1.9**), but the refrigeration efficiency of the latter is only 30-40%, and below 60% of the magnetic refrigeration cycle.[10]

During the conventional refrigeration cycle, the refrigeration is achieved by compressing and decompressing the cooling agent via the external pressure under the adiabatic condition. In addition, two isothermal processes are also included in a conventional refrigeration cycle. Analogous to the conventional vapor-pressure refrigeration cycle, the magnetic refrigeration cycle also consists of two adiabatic and two isothermal processes. At the beginning, a magnetic field is applied adiabatically to the MCE material, therefore, the magnetic moments align along the magnetic field and the system's temperature rises. In the following isothermal process, the heat is expelled into the surroundings and the system goes back to its initial temperature, *T*. At this point, the magnetic field is removed adiabatically, which causes the magnetic moments to become disoriented and the system's temperature to decrease. Subsequently, the system experiences the second isothermal process. To return to the initial state and complete the refrigeration cycle, the magnetocaloric system needs absorb some heat from a targeted object, where a cooling process occurs and the magnetocaloric system is called the refrigerant. In the practical application, the refrigeration cycle is repeated over and over again in order to achieve the continuous cooling.

Although there is a large potential for household and industrial cooling, e.g. air-conditioning and food refrigeration, magnetic refrigeration units are still not practical since many crucial issues have not been resolved yet. For example, achieving a large

MCE under a small applied magnetic field remains one of the most challenging tasks. With respect to this, magnetocaloric materials with a first-order magnetostructural transition could be good candidates. However, inducing a first-order structural transition is not easy. Nowadays, only a few systems were reported to have first-order magnetostructural transitions.[11–16] And all of these magnetocaloric materials possess obvious magnetic and heat hysteresis, which decreases the efficiency of a magnetic refrigeration cycle. In addition, other issues low down adoption of magnetic refrigeration, e. g. high cost, elaborate synthetic methods, poor stability of the materials, and requirements for high magnetic fields.

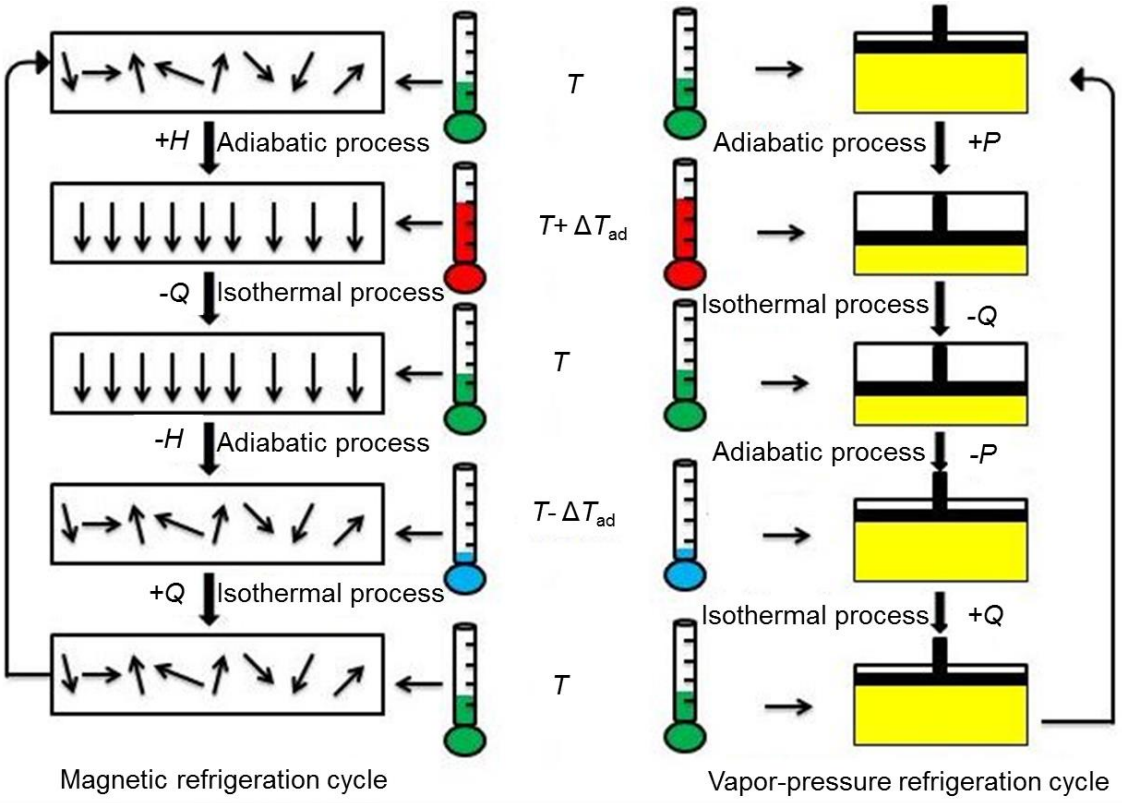

Figure 1.9. Magnetic (left) and conventional vapor-pressure (right) refrigeration cycles.

1.3 Magnetocaloric Materials

Before new magnetocaloric materials are explored, known magnetocaloric phases will be reviewed. In the following sections, the design strategies and characterizations of various magnetocaloric materials with conventional or giant MCE are summarized.

1.3.1 Gd_5T_4-based Phases (*T* = main group elements)

Given that the magnetic entropy change is determined by the total quantum number *J*, large MCE is usually observed in ferromagnetic materials that contain 3*d*- and 4*f*-elements. In addition, 4*f*-elements offer large thermal conductivity and density, which could improve the heat exchange during the refrigeration process and create a high cooling power in a small volume. Based on the discussion above, the 4*f*-elements are the most promising candidates for the high-performance magnetocaloric materials.

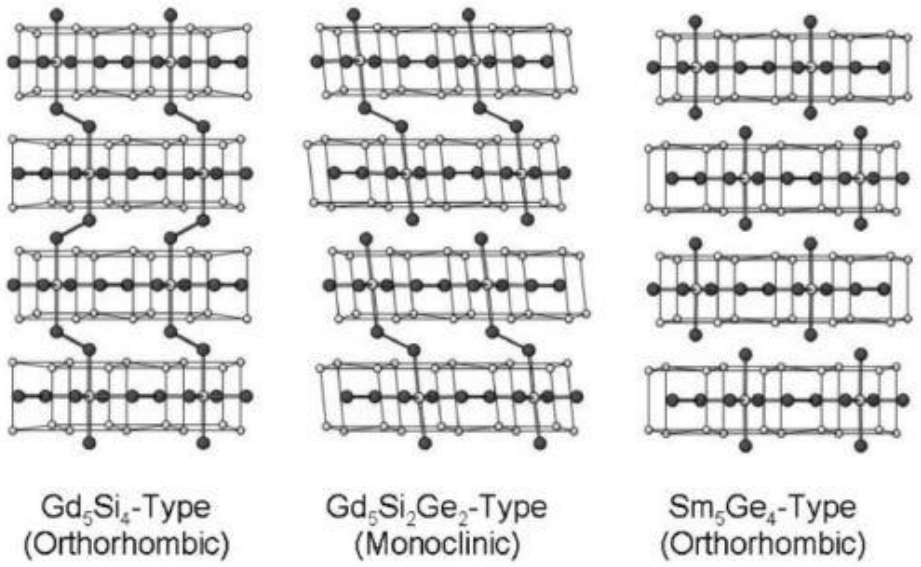

Figure 1.10. Crystal structures of Gd_5Si_4, $Gd_5Si_2Ge_2$, and Sm_5Ge_4-type phase.[10]

Extensive studies have been done on the *RE*-based magnetocaloric materials, but the true breakthrough was the discovery of a giant magnetocaloric effect (GMCE) in the monoclinic $Gd_5Si_2Ge_2$ phase in 1997.[12] The material undergoes a magneto-structural transition and the total entropy change includes not only a magnetic entropy contribution, but also a structural one. Since the discovery of the giant magnetocaloric effect in the $Gd_5Si_2Ge_2$, the Gd_5T_4 and related phases has attracted significant attention.

The GMCE of the Gd_5T_4 and related phases can be attributed to two types of first-order magnetostructural transitions: from the monoclinic paramagnetic $Gd_5Si_2Ge_2$-type structure to the orthorhombic ferromagnetic Gd_5Si_4-type structure, and from the orthorhombic antiferromagnetic Sm_5Ge_4-type structure to the ferromagnetic orthorhombic Gd_5Si_4-type structure **(Figure.1.10)**. The three structures can be distinguished by the interslab *T*-*T* dimers: i) all interslab *T*-*T* dimers are intact in the orthorhombic Gd_5Si_4-type structure; ii) half of the interslab *T*-*T* dimers are broken in the monoclinic $Gd_5Si_2Ge_2$-type structure; and (iii) all interslab *T*-*T* dimers are broken in the orthorhombic Sm_5Ge_4-type structure. In most cases, valence electron count (VEC) or (and) geometric parameters play a main role in defining RE_5T_4 structures: *T*-*T* dimers cleave at higher VEC and reform at lower VEC values. For example, a decrease in the VEC of Gd_5Ge_4 through the Ga substitution leads to the formation of the interslab dimers in $Gd_5Ge_{4-x}Ga_x$.[17] On the other hand, an increase in the VEC in $Gd_5Si_{4-x}P_x$ breaks the interslab *T*-*T* dimers.[18] In addition, the interslab *T*-*T* bonds can also be manipulated by modifying the *T*-atom size. The dimer stretching or cleavage were discovered in $Gd_5Si_{4-x}Ge_x$ and $Gd_5Si_{4-x}Sn_x$ through the substitution of Si with electron-equivalent but larger Ge and Sn. [19,20]

The study on the factors of governing the crystal structures and phase transformations is of great importance to the discovery of new Gd_5T_4-based phases and structures. Based on the previous research results, some new RE_5T_4-based phases have been designed. Our group used the combined VEC and atomic size effects in the $Gd_5Si_{4-x}Bi_x$ system (x = 1.58 - 2.42) to completely cleave the interslab T-T bonds. Equivalence of the interslab $T\cdots T$ contacts, achieved through combination of the electronic and geometric parameters, removed directionality of nearest-slab interactions and allowed for a novel slab stacking.[21,22]

1.3.2 $LaFe_{13-x}Si_x$ Alloys

Pseudo-binary $LaFe_{13-x}Si_x$ alloys adopting the $NaZn_{13}$-type structure attended attraction after the discovery of GMCE in $LaFe_{11.4}Si_{1.6}$.[23] A following study on the $LaFe_{11.4}Si_{1.6}$ alloy indicated a first-order phase transition associated with the GMCE.[24] In general, both a structural transformation and discontinuous volume change can induce a first-order phase transition.[13,16,25] In the case of $LaFe_{13-x}Si_x$ alloys, the first-order phase transition is attributed to the large negative lattice expansion associated with the itinerant electron metamagnetic transition, which induces a very sharp magnetization at T_C.[24,26]

The $NaZn_{13}$-type $LaFe_{13-x}Si_x$ phases could only be obtained with a low Si content. **Figure 1.11** and Table 1.3.1 summarize the physical properties of some reported $NaZn_{13}$-type $LaFe_{13-x}Si_x$.[26,27] Since the atomic size of Si is smaller than that of Fe, the unit cell parameters decrease with an increasing Si content. In addition, the Fe magnetic moment decreases significantly with the increasing Si, which may be attributed to the band

hybridization between the Fe-3*d* and Si-2*p*. [28] T_C values of the same $LaFe_{13-x}Si_x$ alloys differ between different research group. However, the overall trend is identical: T_C increases monotonically with the increasing Si for $LaFe_{13-x}Si_x$ alloys with $1.2 \leq x \leq 2.6$. An exception is $LaFe_{10.2}Si_{2.8}$, which has a relative low T_C and breaks the linear increase of T_C with Si.[29] Due to the absence of substantial studies on the $NaZn_{13}$-type $LaFe_{13-x}Si_x$ phases with x >2 .6, the reasons for the low T_C of $LaFe_{10.2}Si_{2.8}$ are still uncertain.

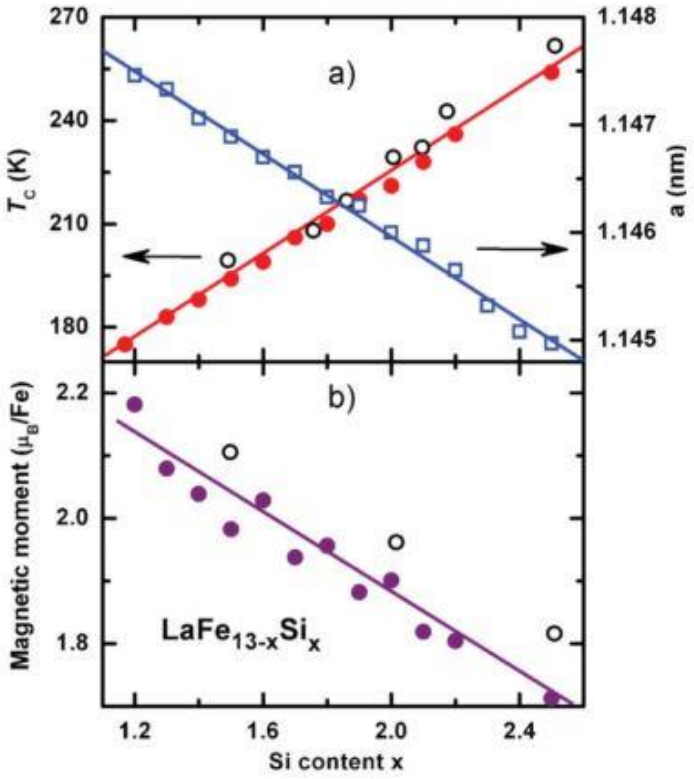

Figure 1.11. a) Curie temperature T_C, lattice constant *a* and **b)** magnetic moment/Fe vs. Si content *x* for $LaFe_{13-x}Si_x$ alloys.[27]

The itinerant electrons originate from the 3*d* electrons of Fe, therefore, the first-order phase transition may evolve into the second-order phase transition by varying the

ratio between Fe and Si. The GMCE associated with the first-order phase transition were only observed in the $LaFe_{13-x}Si_x$ alloys with low Si content and the largest GMCE was obtained in the $LaFe_{11.8}Si_{1.2}$. The boundary between the first- and second-order phases transition is located near $LaFe_{11.7}Si_{1.7}$. The maximum isothermal entropy change ($-\Delta S^{max}$) drops fast when x is more than 1.7, suggesting a conventional MCE and second-order phase transition.

One challenging issue with respect to the study of $LaFe_{13-x}Si_x$ alloys is to eliminate the α-Fe impurity and obtain a pure $NaZn_{13}$-type phase. To date, all of the reported $LaFe_{13-x}Si_x$ alloys are composed of two phases: main $NaZn_{13}$-type phase and ~5% α-Fe, and the α-Fe could not be eliminated even by extended annealing time of 1 month. Based on the La-Fe phase diagram, the immiscible liquids are formed at the Fe-rich side above 1460°C,[30] which may contribute to the presence of ~5% α-Fe in the whole $LaFe_{13-x}Si_x$ family.

Table 1.1. Physical properties of the $NaZn_{13}$-type $LaFe_{13-x}Si_x$.

Sample composition	T_C (K)	$-\Delta S^{max}$ (J/kg K)	Type of phase transition	Reference
$LaFe_{11.8}Si_{1.2}$	–	29.2 (0-5 T)	First-order	[27]
$LaFe_{11.7}Si_{1.3}$	188	29 (0-5 T)	First-order	[31]
$LaFe_{11.7}Si_{1.3}$	183	26 (0-5 T)	First-order	[27]
$LaFe_{11.6}Si_{1.4}$	188	24.7 (0-5 T)	First-order	[27]
$LaFe_{11.5}Si_{1.5}$	194	24.8 (0-5 T)	First-order	[27]
$LaFe_{11.5}Si_{1.5}$	194	23.7 (0-5 T)	First-order	[32]

$LaFe_{11.5}Si_{1.5}$	195	24.6 (0-5 T)	First-order	[33]
$LaFe_{11.5}Si_{1.5}$	198	–	First-order	[34]
$LaFe_{11.8}Si_{1.6}$	199	18.7 (0-5 T)	First-order	[27]
$LaFe_{11.8}Si_{1.6}$	209	19.3 (0-5 T)	First-order	[23]
$LaFe_{11.8}Si_{1.6}$	208	19.4 (0-5 T)	First-order	[24]
$LaFe_{11.3}Si_{1.7}$	206	17.6 (0-5 T)	–	[27]
$LaFe_{11.2}Si_{1.8}$	210	13.0 (0-5 T)	Second-order	[27]
$LaFe_{11.0}Si_{2.0}$	221	7.9 (0-5 T)	Second-order	[27]
$LaFe_{10.9}Si_{2.1}$	234	–	Second-order	[34]
$LaFe_{10.8}Si_{2.2}$	245	–	Second-order	[34]
$LaFe_{10.6}Si_{2.4}$	–	2.8 (0-2 T)	Second-order	[35]
$LaFe_{10.6}Si_{2.4}$	247	5.85 (0-5 T)	Second-order	[29]
$LaFe_{10.5}Si_{2.5}$	262	–	Second-order	[34]
$LaFe_{10.5}Si_{2.5}$	254	–	Second-order	[27]
$LaFe_{10.4}Si_{2.6}$	243	2.3 (0-2 T)	Second-order	[24]
$LaFe_{10.4}Si_{2.6}$	248	5.9 (0-5 T)	Second-order	[29]
$LaFe_{10.2}Si_{2.8}$	195	3.7 (0-5 T)	Second-order	[29]

1.3.3 Ni_2MnGa-based Heusler Alloys

Heusler alloys are a group of compounds with a generic formula of X_2YZ (X and Y = 3d transition elements, Z = IIIA-VA group elements), where the localized magnetic moments of X and/or Y atoms influence each other via the indirect exchange

interaction.[7] Ni_2MnGa-based Heusler alloys are well known for the excellent shape memory effect (SME) and magnetocaloric effect, which could be attributed to a first-order martensitic transformation. At higher temperatures, the Ni_2MnGa-based Heusler alloys adopt a cubic structure. They transform to a low temperature tetragonal or orthorhombic modulated structures upon cooling and/or application of an external magnetic field.[36] Herein, the high temperature and low temperature phases are referred to as the austenitic and martensitic phases, respectively. In addition, the martensitic transformation is completely reversible, therefore, the martensitic phase could go back to the original austenitic phase upon heating. Between the high-temperature austenitic and low-temperature martensitic phases, some orthorhombic super cells are usually observed, which are referred to as the pre-martensitic or precursor phases. (**Figure 1.12**)

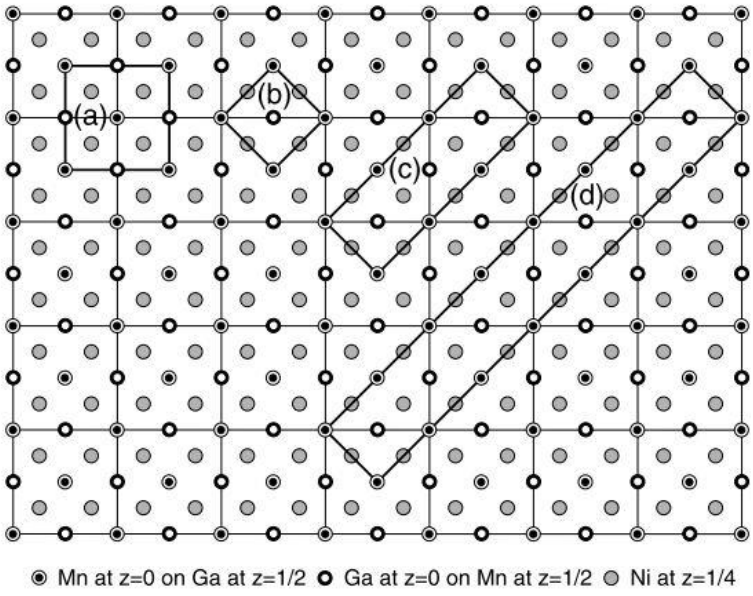

Figure 1.12. Unit cell projection of a) the cubic austenitic phase, b) tetragonal martensitic phase, c) 3-fold orthorhombic modulated structure, d) 7-fold orthorhombic modulated structure.[36]

The martensitic and austenitic phases are both ferromagnetic and the saturation magnetization of the former is larger than that of the latter. However, the magnetization of the martensite is much more difficult to saturate due to the large magnetocrystalline anisotropy. Therefore, the crossing point could be observed in the *M-H* curves of martensite and austenite, which is the boundary between the positive and negative entropy change.

In 2000, the MCE of Ni_2MnGa-based Heusler alloys were first reported in polycrystalline samples.[37] A large positive magnetic entropy change was observed at the austenitic transition temperature T_A under a magnetic field of 0.9 T, which could be attributed to a first–order phase transition from the martensitic phase to the austenitic phase during heating. Except T_A, the martensitic transition temperature T_M and the Curie temperature T_C are also significantly associated with the MCE of Ni_2MnGa-based Heusler alloys ($T_M < T_C$). Further studies suggest that GMCE with a large negative magnetic entropy change could be obtained due to the first-order coupled magneto-structural transition by adjusting the martensitic transition temperature close to the magnetic transition temperature T_C.[38]

The GMCE reported in the Ni_2MnGa-based Heusler alloys have relatively large magnetic entropy change in a large temperature range, which can be controlled by adjusting the ratio of Ni/Mn/Ga. In addition, the Ni_2MnGa-based Heusler alloys have a low cost due to the absence of *RE*, therefore, the Ni_2MnGa-based Heusler alloys may be interesting as the magnetic regenerator materials. However, full width at half maximum

(FWHM) is very small, which limits the application of corresponding Ni_2MnGa-based Heusler alloys.[39]

1.3.4 Magnetocaloric Materials Containing As

1.3.4.1 $MnAs_{1-x}Sb_x$ Alloys

MnAs experiences a first-order magnetostructural transition from a paramagnetic orthorhombic MnP-type structure to a ferromagnetic hexagonal NiAs-type structure during cooling. A 2001 discovery of a large magnetocaloric effect in MnAs[40] initiated studies on the $MnAs_{1-x}Sb_x$ (x = 0.05, and 0.1) alloy. A first-order magnetostructural transition is maintained by the substitution of Sb for As, while the Curie temperature decreases by 35K for x = 0.1. Subsequently, an extremely large MCE for $MnAs_{1-x}Sb_x$ ($0 \leq x \leq 0.4$)[41] and for $MnAs_{1-x}Sb_x$ ($0 \leq x \leq 0.3$)[42] were reported, additionally T_C could be tuned between 220 and 318K for $0 \leq x \leq 0.4$. However, the structural transformation only exists for $x \leq 0.1$, and a second-order magnetic transition is observed for $x > 0.1$. Surprisingly the maximum magnetic entropy change is barely affected for $0 \leq x \leq 0.3$. The GMCE of $MnAs_{1-x}Sb_x$ in $x \leq 0.1$ could be attributed to a first-order magnetic transition, while the large MCE for $x > 0.1$ originates from a metamagnetic trnasition above T_C. Although there is still a metamagnetic transition for x = 0.4, the magnetic entropy change decrease significantly, indicating a conventional MCE.

The $MnAs_{1-x}Sb_x$ ($0 \leq x \leq 0.3$) alloys display extremely large MCE over a broad adjustable T_C from 230 to 315K, and the hysteresis disappears for $x \geq 0.05$. Therefore, the less costly $MnAs_{1-x}Sb_x$ is one of the most promising magnetocaloric materials for

magnetic refrigeration. However, the toxicity and high vapor pressure of As make the preparation difficult and increase the production cost of $MnAs_{1-x}Sb_x$ ($0 \leq x \leq 0.3$).

1.3.4.2 (Mn,Fe)$P_{1-x}As_x$ Alloys

A GMCE was reported in the Fe_2P-type $MnFeP_{0.45}As_{0.55}$ phase with a T_C of 300K in 2002.[11] By varying the P to As ratio,[43] the T_C could be tuned from 168 to 332K. While T_C increases with the As amount, the magnetic entropy change peaks at $MnFeP_{0.65}As_{0.35.}$ The magnetocaloric $MnFeP_{1-x}As_x$ compounds with $0.25 \leq x \leq 0.65$ adopt the Fe_2P-type structure, and their first-order phase transition can be characterized as magnetostriction without a change in the symmetry or relative atomic arrangement but with discontinuity in the lattice parameters.[44] A first-order magneto-structural transition in $MnFeP_{1-x}As_x$ with $0.25 \leq x \leq 0.65$ displays considerable thermal hysteresis which is undesirable for practical applications

Since the magnetic properties of $Mn_{1+y}Fe_{1-y}P_{1-x}As_x$ alloys are determined by the 3*d* electrons, therefore, changing the Mn/Fe ratio impacted the magnetic properties, including MCE. 10% Mn substitution for Fe in $MnFeP_{0.5}As_{0.5}$ has little influence on T_C, while the maximum entropy change increased substantially.[45] Further studies on $Mn_{2-x}Fe_xP_{0.5}As_{0.5}$ ($0 \leq x \leq 0.5$)[46] and ($0.5 \leq x \leq 1$)[47] suggest that T_C increases with the Fe amount. However, a large magnetic entropy change is observed only for $x \geq 0.8$, which is due to the first-order para-to-ferromagnetic transition. For $x \leq 0.5$, the phases order antiferromagnetic, and for $0.5 < x < 0.7$, antiferromagnetism and ferromagnetism coexist.[48]

Similar to the $MnAs_{1-x}Sb_x$ alloys, the application of the MnFe(P,As) compounds is restricted by presence of As. As-free compounds with the Fe_2P-type structure were explored. i.e. $MnFeP_{1-x}Si_x$, $MnFeP_{1-x}Ge_x$ and MnFe(P,Si,Ge).[49–51] However, the high pressure of P is still a challenging issue for the synthesis of these Fe_2P-type compounds. In addition, the thermal hysteresis increases significantly for the As-free Fe_2P-type alloys in most cases.[52] Lastly, it is very difficult to obtain pure Fe_2P-type magnetocaloric compounds.[7]

1.4 Materials in Focus

The above-discussed principles define our research: synthesis of novel intermetallic phases, containing magnetically active 3*d* and 4*f* metals. We also incorporate *p* elements to create a structurally flexible framework, which may undergo a phase transition and deliver a large entropy change. In this dissertation, the interesting intermetallic alloys for the magnetocaloric study are *RE*Co_2- and RE_5Ga_3-based phases. To increase the structural variety, Ga/Co substitution was explored for both families. More than one structure is founded in both systems, suggesting possibility of a GMCE if a structural transformation can be coupled with a magnetic one.

1.4.1 *RE*Co_2-based Phases

Laves phases have a generic formula AB_2. Depending on stacking of the four-layered structural units, Laves phases could adopt a cubic $MgCu_2$-, hexagonal $MgZn_2$-, or hexagonal $MgNi_2$-type structure.[53] In 2002, The GMCE associated with a first-order itinerant electron metamagnetic transition was found in $DyCo_2$, $HoCo_2$, and $ErCo_2$.[54]

Further studies suggest that all other *RE*Co_2 exhibit a conventional MCE due to a second-order magnetic transition.[55] Based on the model relating the magnetovolume effect and spin fluctuation,[56] a first-order magnetic transition could only occur when lattice parameters are between 7.05 and 7.22 Å, and magnetic moments in the Co sublattice are produced by the molecular field of the *RE* sublattice upon application of an external magnetic field. For the two exceptions, $TbCo_2$ and $TmCo_2$, the appearance of a second-order magnetic transition could be attributed to spin fluctuations and a weak molecular field, respectively. The hysteresis originating from the first-order GMCE in *RE*Co_2 is much smaller compared to that in other alloys discussed in section **1.3**.[30]

The discovery of a GMCE with a small hysteresis in the *RE*Co_2 system attracted our attention. In our research we focused on the element substitution for both *RE* and Co. While most of these *RE*Co_2-based alloys possess a conventional MCE due to a second-order magnetic transition, some of the $DyCo_2$-, $HoCo_2$-, $ErCo_2$-based alloys display a first-order magnetic transition and GMCE, i.e., $Dy_{1-x}Y_xCo_2$ for x = 0.9 and 0.7, $Er_{1-x}Dy_xCo_2$ for $0 \leq x \leq 1$,[57] $Ho(Co_{1-x}Si_x)_2$ and $Er(Co_{1-x}Si_x)_2$ for $x \leq 0.075$,[54] $Er(Co_{1-x}Ni_x)_2$ for $x < 0.1$,[58] $Dy(Co_{1-x}Si_x)_2$ for $x \leq 0.05$,[59] $Dy(Co_{1-x}Al_x)_2$ for $x < 0.025$, $Ho(Co_{1-x}Al_x)_2$ and $Er(Co_{1-x}Al_x)_2$ for $x < 0.075$.[60] Substitution above the stated critical values leads to a second-order phase transition.

Majority of the *RE*Co_2-based alloys studied for the MCE adopt the cubic $MgCu_2$-type structure and investigation of the alloys with other crystal structures is less systematic. To explore the latter materials, $GdCo_2$ is chosen as the starting phase due to

some interesting literature results. Firstly, two structures were obtained via substitution of Ga for Co in $GdCo_2$: GdCoGa-[61] and $CeCu_2$-type structures[62], which are different from the $MgCu_2$- and AlB_2-type structures of $GdCo_2$ and $GdGa_2$, respectively. Secondly, exploration of the $Gd(Co_{1-x}Ga_{x)2}$ (x = 0-0.3) materials[63] yielded impurity phases above x = 0.2, suggesting presence of a $MgZn_2$-type phase. Since no subsequent studies on the possible $MgZn_2$-type $Gd(Co_{1-x}Ga_{x)2}$ alloys were performed, we focused on these alloys in the dissertation.

1.4.2 RE_5(Ga,*TM*)$_3$ Alloys

The RE_5Ga_3 materials may not be the most attractive magnetocaloric materials because of their weak magnetic behavior and absence of GMCE, but an interesting structural behavior stimulated our interest in these phases. Three structures were reported for RE_5Ga_3 phases: hexagonal Mn_5Si_3-, tetragonal Cr_5B_3- and W_5Si_3-type ones.[64] By analyzing the atomic radii of RE_5Ga_3, we found that the RE_5Ga_3 structures are related to the rare earth size; the structures change from the Mn_5Si_3- to Cr_5B_3- and then to W_5Si_3-type as the *RE* atoms become larger.

To confirm that the structure-atomic size relationship is more general, we substituted Co for Ga. Since the atomic radius of Ga is slightly larger, the alloys are expected to undergo structural transformations. More important, the magnetic properties determined by the structural type should also change. A paramagnetic or antiferromagenic ground state may become ferromagnetic, which is desirable for magnetic refrigeration.

Additionally, a possible coupling between the structural and magnetic transitions in the $RE_5(Ga, Co)_3$ may induce a GMCE.

While our ultimate goal is to obtain high-performance magnetocaloric materials, we realize that achieving such goal may be quite difficult. However, the knowledge obtained can be used to understand the structure-property relationship in studied and novel materials and ultimately be used for a targeted design of new structures with a large MCE.

Chapter 2. Methodology and Experimentation

2.1 Synthetic Approach

In this dissertation, the starting materials were rare-earth metals, Ta, Si, and 3*d* elements with high melting point. Therefore, a high-temperature synthesis, such as arc-melting or sintering, was used to fuse the raw elements. Since the raw materials are not chemically inert at high temperature, argon-filled atmosphere or vacuum had to be used during synthesis to prevent oxidation. After the elements were fused together, high-temperature annealing was employed to improve homogeneity and crystallinity of the target materials.

The arc-melting furnace is composed of a power source and chamber. The power source controls the output voltage and current, yielding a range of temperatures. **Figure 2.1** is a picture for the chamber of the arc-melting furnace. The Cu hearth is placed at the bottom of the chamber and connected to cooling water, which prevents Cu hearth from melting and cools down the samples rapidly. The silica glass shield isolates the system from the outside atmosphere. Stoichiometric amounts of elements are placed on the Cu hearth, the entire chamber is evacuated to 10^{-2} torr via a rough pump and then back filled with the argon atmosphere. The sample is arc-melted by generating an electric arc between the tungsten electrode and the surface of the sample. Temperature close to 3000°C can be reached, which is sufficient to melt majority of the elements.

After the first arc-melting, the samples are turned over and remelted 2-3 times to achieve homogeneity. To minimize the mass loss during arc-melting, the elements with higher vapour pressure are placed at the bottom. Each alloy is weighed after the arc-melting and the resulting mass is compared with the loading one. If there is an obvious mass loss due to the evaporation, extra raw materials are added to compensate for the losses.

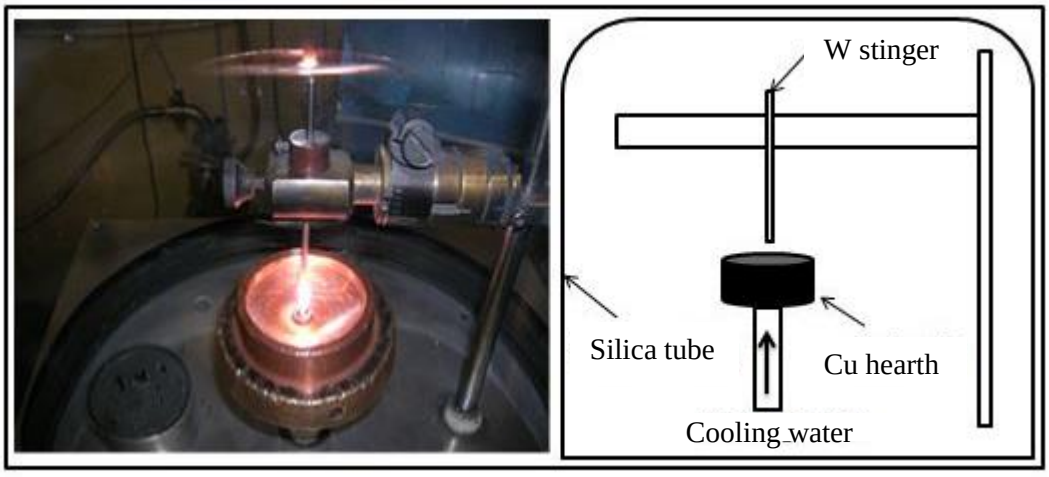

Figure 2.1. A picture (left) and schematic diagram (right) of the arc-melting furnace used for the high temperature synthesis.

Since the melting point of Ta is much higher than the boiling point of Ge (Ta_m = 3017°C, Ge_b = 2833°C), arc melting cannot be applied to prepare Ta_5Ge_3; instead high-temperature sintering was used. Stoichiometric amounts of Ta and Ge were measured, mixed, and pressed into pellets by a hydraulic press. Next, the pellets were sealed in silica ampoules with a length of about 10 cm under a vacuum of 10^{-4} torr. To fuse Ta and Ge,

the sintering temperature 1000°C was chosen. A more detailed description of the Ta_5Ge_3 synthesis is provided in Appendix.

2.2 X-ray Diffraction

Determination of crystal structures of materials is key to understanding their chemical and physical properties and it is typically done by employing X-ray diffraction.

2.2.1 Introduction of X-rays

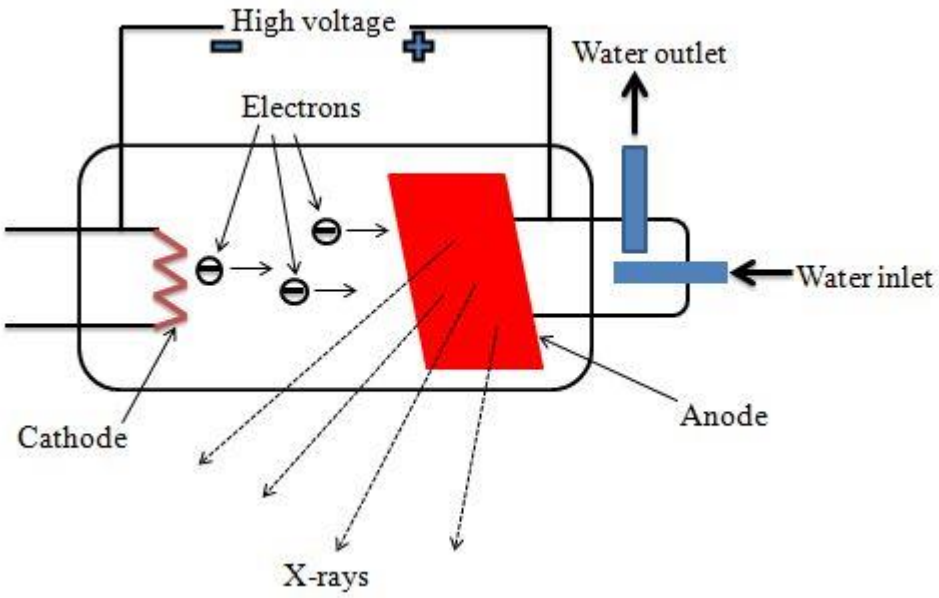

Figure 2.2. The illustration for the generator of X-ray beams.

X-rays are electromagnetic waves with the wavelengths ranging 0.1-100 Å. The generator of X-ray beams is shown in **Figure 2.2**. The anode and cathode are sealed in an evacuated tube. The cathode is heated up to emit electrons, which are accelerated towards the anode. Due to a high voltage between the cathode and anode, the electrons acquire

high kinetic energy before they hit the anode. When electrons are decelerated on the anode, continuous and characteristic X-rays are generated.

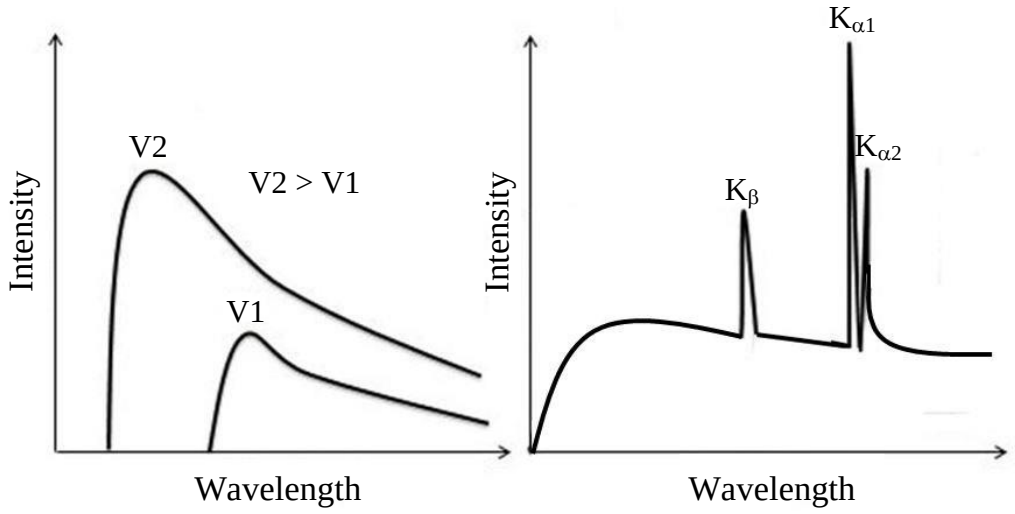

Figure 2.3. Typical spectra of continuum (left) and characteristics (right) X-rays. V1 and V2 are the voltages between cathode and anode.

Continuum X-rays have a broad range of wavelengths and the minimum wavelength is inversely proportional to the electric potential between the anode and cathode. In addition, the anode materials have no influence on the wavelengths of the continuous X-rays. On the other hand, the wavelength of characteristic X-ray is determined by a material of the anode. When the accelerated electrons excite the atoms of the anode, the electrons in the inner shell are knocked out and holes are left. Electrons in the outer shell will fill these holes and the characteristic X-ray will be generated due to the potential energy difference between the inner and outer shells. (**Figure 2.3**)

Compared with the continuous X-rays, characteristic X-rays are more intense and are nearly monochromatic. As a result, characteristic X-rays can be used for structural

determination. Single crystal monochromators are employed to separate the specific characteristic wavelength from the continuous X-rays and from other characteristic lines. Depending on experimental and material requirements, the anode can be Cu, Co, Mo and others. In this dissertation, we use $CuK_{\alpha 1}$ radiation to collect the powder X-ray diffraction data. Since Fe and Gd produce severe fluorescence with CuK_{α} radiation, a Co source is used instead for the samples containing Fe and/or Gd. MoK_{α} radiation was used for single crystal X-ray diffraction.

2.2.2 Bragg's Law

The smallest repeated unit of a crystalline solid is called the unit cell. In the 3D coordinate systems, the unit cells can be characterized by six parameters: *a*, *b*, *c*, *α*, *β*, and *γ*. The first three are the independent basic vectors of the unit cell, while the later three are the interaxial angles. The crystallographic planes of the crystalline solids can be labeled as (*h*,*k*,*l*), known as Miller indices. *h*, *k*, and *l* refer to the integer number of times the planes divide the unit cell in the ***a***, ***b***, and ***c*** directions, respectively. A specific (*h*,*k*,*l*) represents a set of equally spaced crystallographic planes parallel to each other.

Since the wavelength of X-ray has the comparable size with the periodicities of crystalline solids, X-ray diffraction could occur via the elastic scattering by the electrons of the crystalline solids. When Bragg's law is satisfied, the intensity of scattered X-ray beams is enhanced due to the constructive interference,

$$n\lambda = 2d_{hkl}sin\theta \qquad (2.1)$$

where λ is the wavelength of incident X-ray, d_{hkl} is the interplanar spacing for the set of crystallographic planes (*h*,*k*,*l*), and θ is the Bragg angle. (**Figure 2.4**) On the other hand, the signals of scattered X-ray beams could disappear or become weak because of the destructive interference.

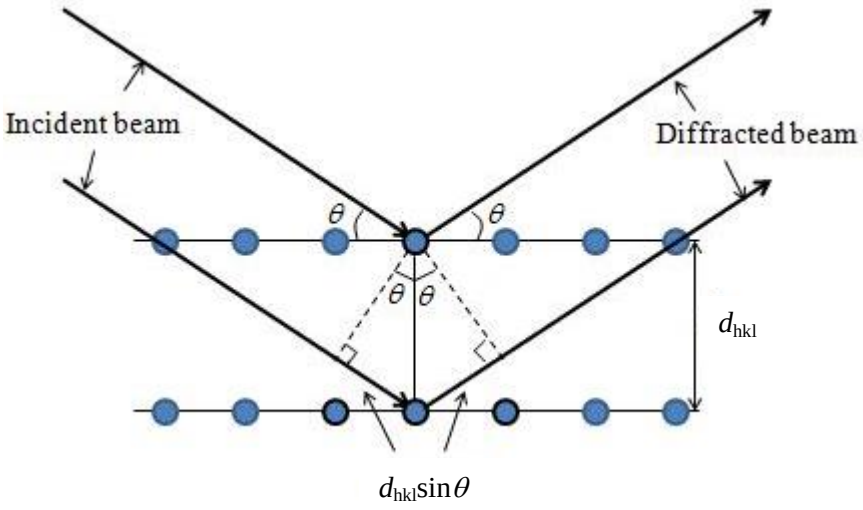

Figure 2.4. X-rays Diffraction by Bragg's law in a two-dimensional lattice of a crystalline solid.

In the 1880's, J. W. Gibbs invented the concept of a reciprocal lattice. To better describe the phenomenon of diffraction in crystalline solids, P. P. Ewald introduced the concept of a reciprocal lattice. There are also three lattice vectors, ***a****, ***b****, and ***c**** in the reciprocal space, which can be related mathematically to the real space of crystalline solids,

$$\boldsymbol{a}^* = \frac{\boldsymbol{b}\times\boldsymbol{c}}{V}, \boldsymbol{b}^* = \frac{\boldsymbol{a}\times\boldsymbol{c}}{V}, \boldsymbol{c}^* = \frac{\boldsymbol{b}\times\boldsymbol{a}}{V} \quad (2.2)$$

where V is the volume of the unit cell. The points of the reciprocal lattice are derived from the crystallographic planes of the real space. Therefore, (h,k,l) could also be used to describe the points of the reciprocal lattice. The reciprocal lattice vector, $\boldsymbol{d_{hkl}}*$, could be constructed by connecting the origin and (h,k,l) in the reciprocal lattice,

$$\boldsymbol{d_{hkl}}* = h\boldsymbol{a}^* + k\boldsymbol{b}^* + l\boldsymbol{c}^* \tag{2.3}$$

$\boldsymbol{d_{hkl}}*$ is normal to the crystallographic planes (h,k,l) of the real lattice and has a length of $1/d_{hkl}$.

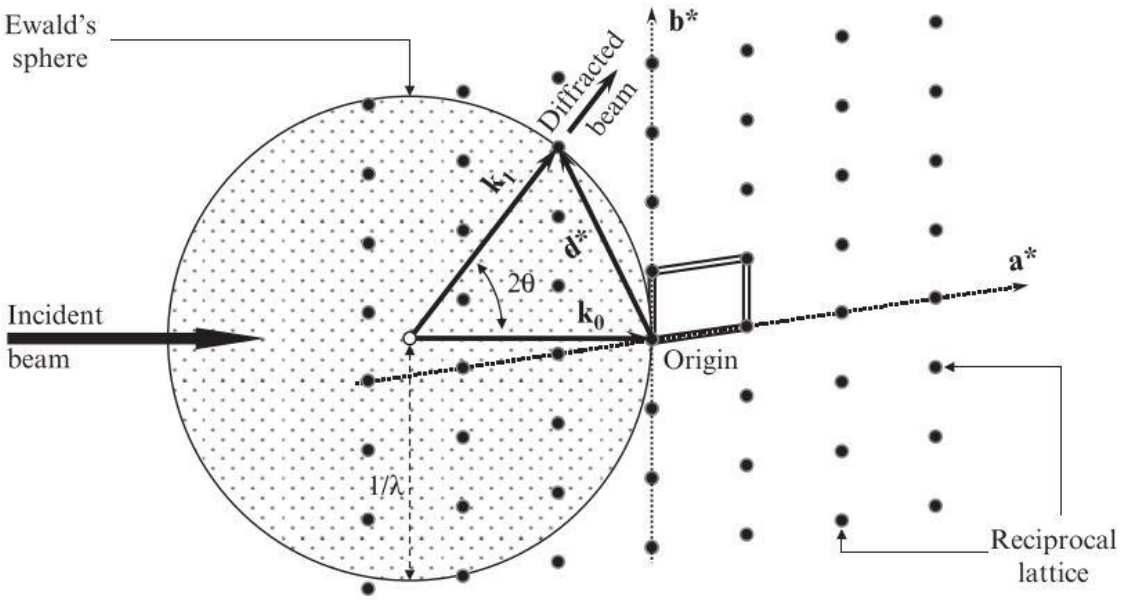

Figure 2.5. Schematic diagram of diffraction using the two-dimensional Ewald's sphere and reciprocal space.[65]

The diffraction condition expressed by Bragg's law can be more visually represented via the Ewald sphere in the reciprocal space (**Fig. 2.5**), with a radius of 1/λ.

The propagation vectors of the incident and scattered X-ray are represented by $\boldsymbol{k_0}$ and $\boldsymbol{k_1}$, respectively. Since $\boldsymbol{k_0}$ ends at the origin of reciprocal lattice and the corresponding length is 1/λ, $\boldsymbol{k_1}$ should have the same wavelength, 1/λ, when the scattering is elastic. In addition, the intersection point of $\boldsymbol{k_0}$ and $\boldsymbol{k_1}$ sits at the center of Ewald's sphere. Hence, the angles between $\boldsymbol{k_0}$ and $\boldsymbol{k_1}$ should be 2θ. By the definition of the reciprocal lattice, all the reciprocal lattice points on the surface of the Ewald's sphere meet the Bragg's law, therefore, the diffraction could occur for the corresponding crystallographic planes of the real lattice at the given 2θ.

2.2.3 Structure Factor and Fourier Transformation

The observed intensity of a given diffraction is determined by the square of the structure factor, $|F_{hkl}|^2$. Therefore, the structure factor, F_{hkl}, is very important for the study of X-ray diffraction. The scattering ability of an atom is an atomic scattering factor *f*, and if the unit cell of a crystalline solid consists of *n* atoms, F_{hkl} could be calculated by adding up all the products between f_j and the corresponding exponential function,

$$F_{hkl} = \sum_{\mathrm{j}=1}^{n} f_j \, g_j t_j e^{2\pi \mathbf{i}(hx_j + ky_j + lz_\mathrm{j})} \tag{2.4}$$

where g_j and t_j are the occupancy and atomic displacement parameters, respectively. By employing the Euler's rule, the structure factor can be rewritten as the sum of real and imaginary part,

$$F_{hkl} = \sum_{j=1}^{n} f_j g_j t_j \cos 2\pi\left(hx_j + ky_j + lz_j\right) + \mathbf{i} \sum_{j=1}^{n} f_j g_j t_j \sin 2\pi\left(hx_j + ky_j + lz_j\right) \tag{2.5}$$

Therefore, $\boldsymbol{F}_{hkl}$could be referred to as a vector with a phase angle of $2\pi(hx_j+ky_j+lz_j)$.

The experimental intensity of X-ray diffraction contains only the $|F_{hkl}|^2$ values, all the information about the phase angle is lost, which makes determination of the atomic coordinates complex. The loss of information about phase angles is referred to as the phase problem. The direct and Patterson method are commonly employed to solve the phase problem.

In the direct method, a phase angle is first assigned to one reflection. Since the phase angles are statistically related to each other, the other phase angles can be derived properly from the initial one. Herein, a triplet of reflections is employed to expand the phase angles in the crystal lattice. The reasonable initial phase angle and acceptable solution can be found by repeating the process.

On the other hand, the Patterson method takes advantage of the Patterson function of the F^2–Fourier series to generate the interatomic vectors of the density distribution of the unit cell, i.e., the Patterson map. Due to the characteristics of Fourier transformation, the Patterson map contains information related to the atomic coordinates of the unit cell. Therefore, the phase angle problem could be possibly resolved. However, the Patterson method is often applied to solve the phase angle problem of the heavy atoms, i.e., heavy-atom method.[65]

With either method, a possible structural solution can be obtained, therefore, a Fourier map of the unit cell in the real space could be set up, i.e. the initial structure solution can be obtained. By comparing calculated intensities of the initial structure with

the observed intensities, an agreement factor could be found based on the least-square method. By refining the agreement factor, the initial structural model could be improved, i.e. refined. Structural refinement is repeated until the agreement factor reaches the minimum value.

2.2.4 X-ray Single Crystal Diffraction

In this dissertation, single crystals were mounted on glass capillaries via the epoxy glue. All the single crystal X-ray data were collected in the whole reciprocal sphere on a STOE IPDS II diffractometer equipped with an image plate detector and MoK_α radiation. Firstly, the collected frames are combined to construct the diffraction peaks of the reciprocal lattices. Therefore, a possible crystal system and the unit cell parameters could be produced via a semiautomatic indexing procedure. Subsequently, the numerical absorption correction based on the crystal shape and generated from the optical face indexing is optimized against the equivalent reflections via the STOE X-Shape software.[66] Since the systematic absences correspond to a specific symmetry element, a space group could be determined based on the systematic absences. By implementing the SHELX-97 programs, the crystal structures could be solved.[67]

The least-squares method was employed for the structural refinements of the SHELX-97 programs. The following agreement factors were used:

$$R_1 = \frac{\sum_{i=1,n} \left\| F_{obs,i} \right| - \left| F_{cal,i} \right\|}{\sum_{i=1,n} \left| F_{obs,i} \right|} \qquad (2.6)$$

$$wR_2 = \left[\frac{\sum_{i=1,n} w_i \left| F^2_{obs,i} - F^2_{cal,i} \right|^2}{\sum_{i=1,n} w_i \left(F^2_{obs,i} \right)^2} \right] \quad (2.7)$$

$$S = \left[\frac{\sum_{i=1,n} w_i \left| F^2_{obs,i} - F^2_{cal,i} \right|^2}{n - p} \right] \quad (2.8)$$

where R_1 and wR_2 are called the R and weighted R factors, and S is the goodness of fit . n-the total number of reflections, F-the structure factor, p-the number of refined parameters, $w_i = 1/Y^2_{\text{obs, i}}$ where Y denotes the intensity of observed reflection.

The refined parameters in the SHELXL program are element type, atomic coordinates, occupancies (and mixing), isotropic/anisotropic temperature factors, extinction coefficient (correction of back-reflection and re-reflection), and weighting scheme (correction of the contribution from reflections with different intensities). In addition to the agreement factors, the validity of refined model can also be verified by the atomic thermal vibration, interatomic distances and angles, etc.

2.2.5 X-ray Powder Diffraction

Powder X-ray diffraction could be utilized to analyze polycrystalline samples. Since the polycrystalline samples consist of a large amount of tiny single crystals with random orientations, the diffraction beams construct a group of coaxial cones around the direction of incident X-ray in the Ewald's sphere of the reciprocal lattice. (**Figure 2.6**) The base of the cones forms rings with different radius, which is called Debye rings. Each ring is characterized by the 2θ angle, intensity and (h, k, l) indices. A 1-D linear detector

can be employed to integrate the X-ray diffraction beams along the circumference of an equatorial plane in the Ewald's sphere.

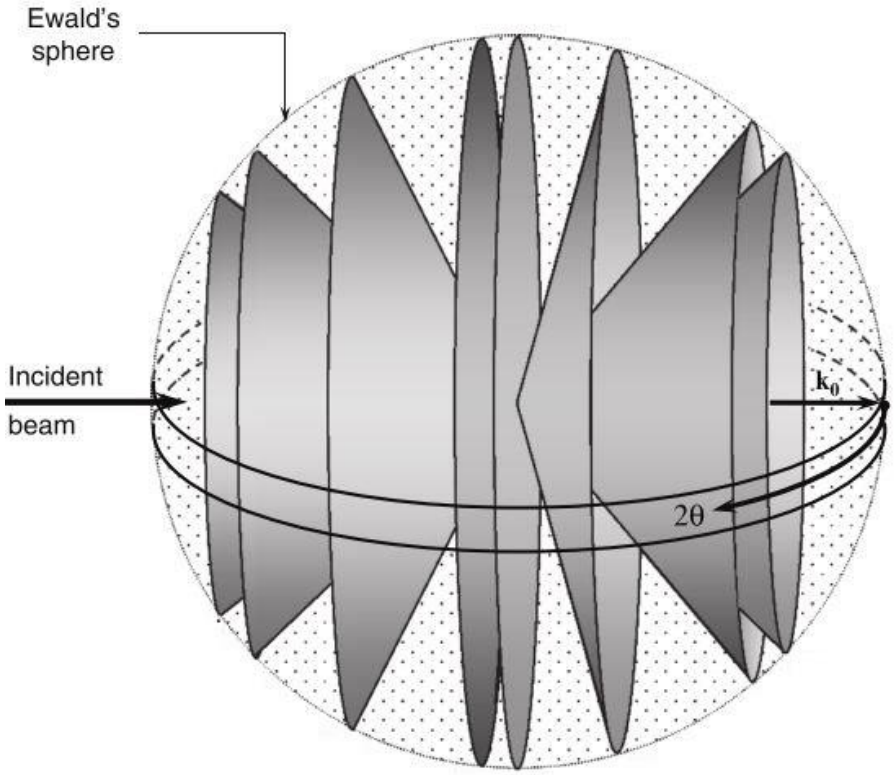

Figure 2.6. The illustration of coaxial cones around the direction of incident X-ray on the Eward's sphere for the Powder diffraction.[65]

Powder diffraction could be used for phase analysis, structural refinement, as well as structural solution. However, the structural solution from powder diffraction is less often undertaken due to the loss of vectors' directions in the reciprocal space. In this dissertation, we only use the X-ray powder diffraction for the phase analysis and structural refinement of polycrystalline samples with known structures.

Powder diffraction data were collected on a PANalytical X'Pert Pro diffractometer equipped with an X'Celerator linear detector composing of 128 independent detection channels. First, the polycrystalline samples of about 30 mg are ground finely in a mortar, deposited on a zero-background quartz wafer coated with vaseline, and placed on the spinning sample stage. Spinning of the sample increases the number of diffracting crystallites and minimizes the effect of the preferred orientation. The incident beam is Cu$K_{\alpha 1}$ and is produced by a Ge monochromator. When a sample contains Gd and/or Fe, CoK_{α} radiation ($K_{\alpha 2}/K_{\alpha 1}$ = 0.5) is employed to eliminate the fluorescence associated with Cu$K_{\alpha 1}$. For the Co source, a Fe filter is inserted to eliminate the CoK_{β} and white radiation.

The full-profile Rietveld technique (Rietica program)[68] is employed to refine the structures. The parameters refined are the background profiles, peak shape, lattice parameters, atomic coordinates, occupancies and displacement parameters. The quality of the refinement is judged by the following agreement factors:

$$R_{\mathrm{p}} = 100 \frac{\sum_{\mathrm{i}=1,\mathrm{n}} \left| \mathrm{y}_{\mathrm{obs,i}} - \mathrm{y}_{\mathrm{cal,i}} \right|}{\sum_{\mathrm{i}=1,\mathrm{n}} \mathrm{y}_{\mathrm{obs,i}}} \tag{2.9}$$

$$R_{\mathrm{wp}} = 100 \left[\frac{\sum_{\mathrm{i}=1,\mathrm{n}} \mathrm{w}_{\mathrm{i}} \left| \mathrm{y}_{\mathrm{obs,i}} - \mathrm{y}_{\mathrm{cal,i}} \right|^2}{\sum_{\mathrm{i}=1,\mathrm{n}} \mathrm{w}_{\mathrm{i}} \mathrm{y}_{\mathrm{obs,i}}^{\ 2}} \right]^{1/2} \tag{2.10}$$

$$\chi^2 = 100 \left[\frac{R_{\mathrm{wp}}}{R_{\mathrm{exp}}} \right]^{1/2} \tag{2.11}$$

R_p, R_{wp}, and χ^2 are the profile, weighted profile, and goodness of fit, respectively. Herein, y_i is the profile intensity at point i, n is the number of data points, $w_i = 1/Y^2_{obs,i}$, where Y is the intensity of the observed reflection.

2.3 Energy Dispersive Spectroscopy (EDS)

The structural solution and composition derived from the X-ray diffraction are based on the scattering power of atoms (i.e. number of electrons in atoms). Therefore, it is difficult to identify elements with similar atomic numbers. In such cases, energy-dispersive X-ray spectroscopy can be employed to complete the compositional analysis. In addition, energy-dispersive X-ray spectroscopy is an effective and direct technique in detecting both amorphous and crystalline impurities.

EDS relies on detecting X-rays emitted by the atoms in samples. An electron beam hits an atom, ejecting a core electron into vacuum and creating an electron hole. The energy of the atom decreases when an electron from a higher energy state drops into the hole. During this relaxation, characteristic X-rays are produced. The energy of the emitted X-ray depends on the energy difference between two electron shells and varies between neighbouring elements. By analyzing the intensity and energy of emitted X-ray, semi-quantitative compositions of samples can be obtained.

The EDS experiments were performed on a JEOL 7000F scanning electron microscope (SEM). Nickel or copper metals with a purity of 99.999 wt. % were used to standardize the signals. The samples were mounted on carbon tapes attached to the sample holder. The samples were laced inside the SEM chamber and evacuated. In

addition to chemical analysis, topography and morphology of the sample with chemical contrast could be obtained.

When a quantitative elemental analysis was required, the samples were analyzed using an INCA-Energy-350 X-ray EDS spectrometer (Oxford Instruments) on a Jeol JSM-6480LV scanning electron microscope (20 kV accelerating voltage, beam current 0.7 nA and beam diameter 50 μm). Signals averaged over three points of the selected regions were used to calculate the elemental compositions. L-series lines were chosen for rare-earth elements, while K-series lines were used for the 3*d* transition elements and *p* elements.[69]

2.4 Superconducting Quantum Interference Device (SQUID)

To study the magnetic properties of the samples, magnetic measurements were performed using superconducting quantum interference device (SQUID) on the magnetic property measurement system (MPMS). The samples measured by SQUID can be either a solid chunk or powder. The former were mounted on a glassy rod with Apiezon grease and wrapped with the Teflon tape, while the latter were mounted inside the gelatin capsule and put into the plastic straw. Direct current (DC) and reciprocating sample option (RSO) are the two highly sensitive modes used on the SQUID instrument. The magnetization vs. temperature measurements were done with the RSO mode due to its fast measurement speed, which oscillated around the center of the inductive coils. The saturation magnetization was collected under the DC mode, where the average

magnetization over a number of pre-set times was measured by transporting samples along the inductive coils in the discrete steps.

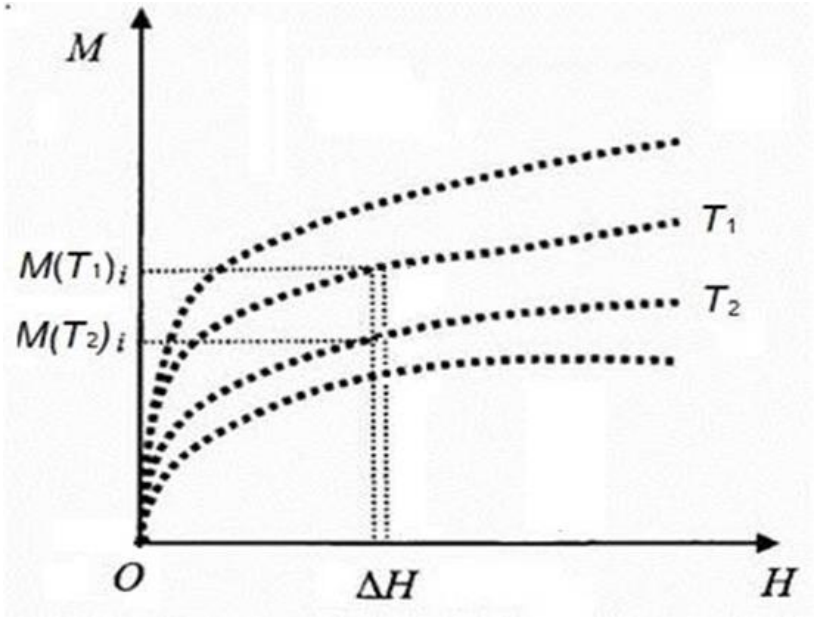

Figure 2.7. Magnetization (*M*) vs. applied magnetic field (*H*) plots.

The magnetocaloric effect in terms of the isothermal magnetic entropy change, ΔS_{mag}, can be derived from the Maxwell relations:

$$\left(\Delta S_{mag}\right)_T = \int_{H_i}^{H_f} \left(\frac{\partial M}{\partial T}\right)_{\mathrm{H}} \mathrm{d}H \qquad (2.12)$$

where H_{i} and H_f are the initial and final magnetic fields, respectively. In practice, a numerical integration is performed using the following formula

$$(\Delta S_{mag})_{\frac{T_1+T_2}{2}} = \sum_i \frac{M(T_2)_i - M(T_1)_i}{T_2 - T_1} \Delta H \qquad (2.13)$$

where ΔH is a magnetic field step and $M(T_2)_i$ and $M(T_1)_i$ are the values of magnetization at temperatures T_2 and T_1, respectively. (**Figure 2.7**)

2.5 Electronic Structure Calculations

To better understand the relationship between the structure and physical properties of the studied materials, electronic structure calculations were performed. The density of states and character of the bonds were typically calculated. The calculations were done with the Stuttgart program using the tight-binding, linear-muffin tin orbital method with the atomic sphere approximation (TB-LMTO-ASA).[70] Experimentally determined structural parameters were input into the program. The 4*f*-electrons were treated as the core electrons. The local density approximation (LDA)[71] and local spin-density approximation (LSDA)[72] were employed to deal with the exchange and correlation. A scalar relativistic approximation[73] was used to account for all the relativistic effects except the spin-orbital coupling. To make the overlapping potential be the optimal approximation to the full potential, the overlapping Wigner-Seitz (WS) cells with required radii were used to fill the space in the ASA method. In addition, the empty spheres built by using the automatic sphere generation[74] were added in the unit cell to better meet the requirement of overlapping criteria in the TB-LMTO-ASA model.

Chapter 3. Targeted Structural Changes and Magnetic Properties Study in $(Ho/Er)_5Ga_{3-x}(Co/Fe)_x$

This chapter contains the material covered in the manuscript "Targeted Structural Changes and Magnetic Properties Study in $(Ho/Er)_5Ga_{3-x}(Co/Fe)_x$", which was published in Journal of Alloys and Compounds (*J. Alloys Compd.* **2015,** 620, 376–382). The candidate finished all of the experimental procedures, data interpretations, structure determinations, and prepared the manuscript. Dr. Alex V. Morozkin assisted with the microprobe analysis of the selected samples.

Phase transformations in the $Ho_5Ga_{3-x}Co_x$ (x = 0, 0.1, 0.2, 0.3, 0.4, 0.5, 1), $Er_5Ga_{3-x}Fe_x$ (x = 0, 0.4), and $Er_5Ga_{3-x}Co_x$ (x = 0, 0.4) system reveal an intimate coupling between the crystal structure and atomic size. A decrease in the effective atomic size of the Ga site through the transition metal substitution results in a transition from the Mn_5Si_3-type structure to Cr_5B_3-type one. According to the single crystal X-ray diffraction, Co and Fe substitution occurs only on the Ga 8*h* site. The relationship between the composition, crystal structures and magnetic properties is analyzed. Magnetization studies for pure Ho_5Ga_3, $Ho_5Ga_{2.9}Co_{0.1}$, $Ho_5Ga_{2.7}Co_{0.3}$, $Ho_5Ga_{2.6}Co_{0.4}$ phase reveal an antiferromagnetic ordering for Ho_5Ga_3, but ferromagnetic transition for the other phases. In addition, the ferromagnetic transition temperature increases with the Co amount. The maximum magnetic entropy change of -12.7 J/(kgK) is obtained in $Ho_5Ga_{2.6}Co_{0.4}$ at 32.5K.

3.1 Introduction

Increasing environmental pressure and limited natural resources urge development of novel, more efficient cooling techniques that can replace conventional vapor-cycle refrigeration. One of the most promising approaches is magnetic refrigeration based on magnetocaloric effect (MCE). However, some important problems have to be addressed prior to the implementation of this technique. One of the most challenging tasks is to achieve large MCE values in relatively small magnetic fields. A breakthrough was the discovery of a giant magnetocaloric effect (GMCE) in $Gd_5Si_2Ge_2$ in 1997.[12] This material undergoes a first-order coupled magneto-structural transition and the total entropy change includes not only a magnetic entropy contribution, but also a structural one.

The discovery of a GMCE in $Gd_5Si_2Ge_2$ initiated extensive research on the related RE_5T_4 phases (*RE* = rare earth, *T* is a *p*-element). One of the important outcomes is the possibility to tune the structural and magnetic properties of RE_5T_4 through valence electron concentration (VEC).[17,22,75–77] It was also shown that the VEC stabilization can be applied to other phases, e.g. the non-existing Gd_4Ge_3 binary can be stabilized through a VEC increase.[78]

Compared with the RE_5T_4 series, the magnetic and structural properties of RE_5X_3 (*X* is Si, Ge, Sn, Sb, Bi) are less systematically explored, and in general the factors governing their stability and phase transformations are not as well understood. The literature data suggest that both the RE_5X_3 tetrelides and pnictides adopt the Mn_5Si_3-type structure, suggesting that neither the VEC nor atomic size alone dictates their stability.[79–82] On the other hand, the RE_5Ga_3 phases present an interesting case as their structures are governed by the size of the rare earths. The three structures identified for RE_5Ga_3 are hexagonal Mn_5Si_3-type, tetragonal Cr_5B_3-type and W_5Si_3-type ones (**Figure 3.1**), and their stability can be summarized as follows (except for La and Y): (1) a hexagonal Mn_5Si_3-type structure ($P6_3/mcm$) forms for Ho (1.74 Å) and smaller rare-earth atoms; (2) a tetragonal Cr_5B_3-type structure ($I4/mcm$) is stable between Dy (1.75 Å) and Nd (1.81 Å); (3) a tetragonal W_5Si_3-type structure ($I4/mcm$) is observed for Pr (1.82 Å) and Ce (1.83 Å); (4) RE_5Ga_3 phases are unknown for Yb (1.94 Å) and Eu (2.00 Å).[64,83–87] This structure-atomic size relationship provides a possibility to stabilize a specific structure of RE_5Ga_3 through elemental substitution either on the *RE* or Ga sites. Since Ho_5Ga_3 and

Er_5Ga_3 sit close to the Cr_5B_3-Mn_5Si_3 boundary, a transition between the two structures should be achieved by tuning the average atomic size of the *RE* or Ga sites.

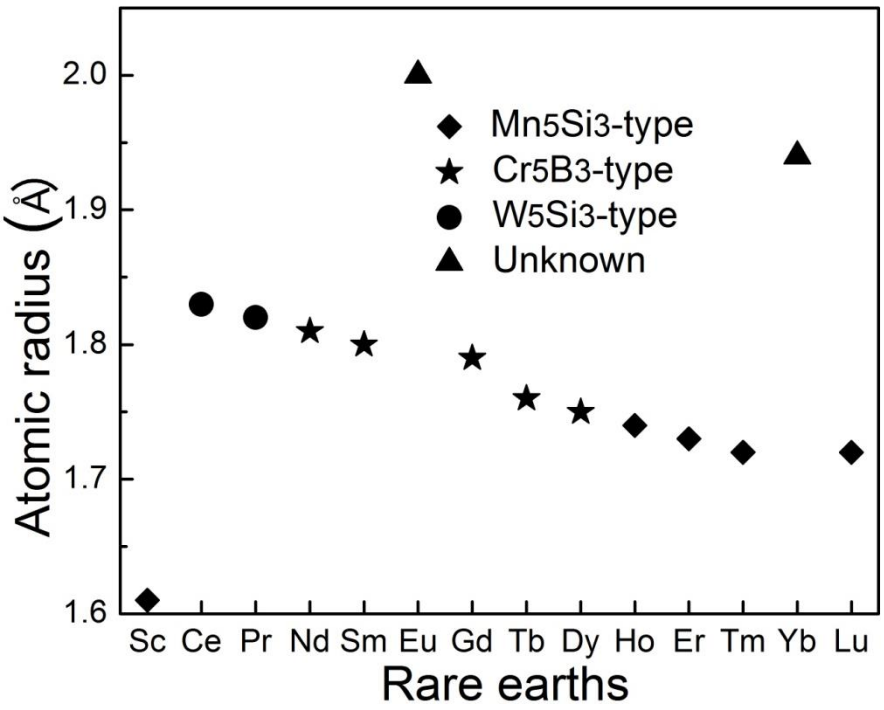

Figure 3.1. Structural map for RE_5Ga_3 phases.

In our research, we focused on the $Ho_5Ga_{3-x}Co_x$, $Er_5Ga_{3-x}Fe_x$, and $Er_5Ga_{3-x}Co_x$ systems as the size difference between Co (Fe) and Ga (r_{Fe} = 1.24 Å, r_{Co} = 1.25 Å and r_{Ga} = 1.26 Å) is comparable to that between the rare-earth elements (r_{Er} = 1.73 Å, r_{Ho} = 1.74 Å and r_{Dy} = 1.75 Å) and, in principle, should allow structural tuning. Additionally, the RE_5Ga_3 phases order antiferromagnetically or remain paramagnetic,[64,85,88] which makes them unsuitable for magnetic refrigeration. Through the Co or Fe substitution, we aimed to change the ground magnetic state into a ferromagnetic one. In this work, we reported on the successful stabilization of the Cr_5B_3-type structure in Ho_5Ga_3 and Er_5Ga_3 via Co

and Fe substitution. We also presented magnetic properties of newly discovered $Ho_5Ga_{3-x}Co_x$ series and MCE of $Ho_5Ga_{2.7}Co_{0.3}$ and $Ho_5Ga_{2.6}Co_{0.4}$ phases with the Cr_5B_3-type structure.

3.2 Experimental Section

3.2.1 Synthesis

The starting materials were pieces of holmium and erbium (99.9+ wt. %, distilled grade, Metall Rare Earth Limited, China), cobalt (99.9 wt. %, Alfa Aesar), iron (99.9 wt. %, Alfa Aesar) and gallium (99.9999 wt. %, Alfa Aesar). The surfaces of Ho and Er metal lumps were cleaned with a file before they were cut into pieces. The $Ho_5Ga_{3-x}Co_x$ (x = 0, 0.1, 0.2, 0.3, 0.4, 0.5, 1), $Er_5Ga_{3-x}Fe_x$ (x = 0, 0.4), and $Er_5Ga_{3-x}Co_x$ (x = 0, 0.4) samples were arc-melted at least three times to improve the homogeneity. The cast samples were wrapped in individual Ta foils, sealed in evacuated silica tubes and annealed at 900^{o}C for 1 week to improve crystallinity and homogeneity. The tubes were then quenched in cold water.

3.2.2 X-ray Powder Diffraction

Powder X-ray diffraction (XRD) data for the $Ho_5Ga_{3-x}Co_x$ (x = 0, 0.1, 0.2, 0.3, 0.4, 0.5, 1), $Er_5Ga_{3-x}Fe_x$, and $Er_5Ga_{3-x}Co_x$ (x = 0, 0.4) samples were collected on a PANalytical X'Pert Pro diffractometer equipped with a linear X'Celerator detector and using the Cu $K_{\alpha 1}$ radiation. The phase analysis were carried out through the Rietveld refinement using the *Rietic*a program.[89] The cast Ho_5Ga_3 and $Ho_5Ga_{2.9}Co_{0.1}$ samples contained Mn_5Si_3-type

phases, however annealing at 900°C yielded the Ba_5Si_3-type phase and unknown impurity/ies. All the other cast Ho-containing samples were found to be mixture of both Mn_5Si_3-type (main phase) and Cr_5B_3-type phases; annealing yielded high-purity Cr_5B_3-type phases only for the $Ho_5Ga_{2.7}Co_{0.3}$ and $Ho_5Ga_{2.6}Co_{0.4}$ samples. The cast Er_5Ga_3 was a mixture of the Mn_5Si_3-type phases and unknown impurity/ies. The cast $Er_5Ga_{2.6}Co_{0.4}$ and $Er_5Ga_{2.6}Fe_{0.4}$ had both Mn_5Si_3-type (main phase) and Cr_5B_3-type phases. After annealing at 900°C for 1 week, a pure Cr_5B_3-type phase was obtained in $Er_5Ga_{2.6}Fe_{0.4}$, while large amounts of Er_3Ga_2-type impurities were observed in $Er_5Ga_{2.6}Co_{0.4}$ (**Table 3.1**).

Table 3.1. Structure types of the major phase in $Ho_5Ga_{3-x}Co_x$, $Er_5Ga_{3-x}Fe_x$, and $Er_5Ga_{3-x}Co_x$.

Composition	treatment	str. type of major phase
Ho_5Ga_3	cast	Mn_5Si_3
	annealed	Ba_5Si_3
$Ho_5Ga_{2.9}Co_{0.1}$	cast	Mn_5Si_3
	annealed	Ba_5Si_3
$Ho_5Ga_{2.8}Co_{0.2}$	cast	Mn_5Si_3 + Cr_5B_3
	annealed	Cr_5B_3+impurity/ies
$Ho_5Ga_{2.7}Co_{0.3}$	cast	Mn_5Si_3 + Cr_5B_3
	annealed	Cr_5B_3
$Ho_5Ga_{2.6}Co_{0.4}$	cast	Mn_5Si_3 + Cr_5B_3
	annealed	Cr_5B_3
$Ho_5Ga_{2.5}Co_{0.5}$	cast	Mn_5Si_3 + Cr_5B_3
	annealed	Cr_5B_3+impurity/ies
Ho_5Ga_2Co	cast	Mn_5Si_3 + Cr_5B_3
	annealed	Cr_5B_3+impurity/ies
Er_5Ga_3	cast	Mn_5Si_3+impurity/ies
	annealed	Ba_5Si_3

$Er_5Ga_{2.6}Fe_{0.4}$	cast	Mn_5Si_3 + Cr_5B_3
	annealed	Cr_5B_3
$Er_5Ga_{2.6}Co_{0.4}$	cast	Mn_5Si_3
	annealed	Cr_5B_3+impurity/ies

Based on the phase analysis, five single phase samples were obtained: cast Ho_5Ga_3 and $Ho_5Ga_{2.9}Co_{0.1}$, annealed $Ho_5Ga_{2.7}Co_{0.3,}$ $Ho_5Ga_{2.6}Co_{0.4}$ and $Er_5Ga_{2.6}Fe_{0.4}$. The unit cell dimensions derived from the Rietveld refinement (*Rietic*a program[89]) for these samples are summarized in **Table 3.2**. The lattice parameters decrease upon the transition metal substitution due to the atomic size difference between Ga and Co/Fe.

Table 3.2. Crystallographic data for the $Ho_5Ga_{3-x}Co_x$ and $Er_5Ga_{2.6}Fe_{0.4}$ samples determined from the powder X-ray diffraction.

Composition	treatment	str. type	*a*, Å	*c*, Å	*V*, Å^3
Ho_5Ga_3	cast	Mn_5Si_3	8.5403(1)	6.4151(2)	405.21(1)
$Ho_5Ga_{2.9}Co_{0.1}$	cast	Mn_5Si_3	8.5339(1)	6.4086(1)	404.200(3)
$Ho_5Ga_{2.7}Co_{0.3}$	annealed	Cr_5B_3	7.5753(1)	13.8844(3)	796.76(2)
$Ho_5Ga_{2.6}Co_{0.4}$	annealed	Cr_5B_3	7.5674(1)	13.8514(6)	793.21(4)
$Er_5Ga_{2.6}Fe_{0.4}$	annealed	Cr_5B_3	7.5360(1)	13.8731(5)	787.88(4)

3.2.3 X-ray Single-crystal Diffraction

Single crystal X-ray diffraction studies were performed on the crystals extracted from the cast $Ho_5Ga_{3,}$ annealed $Ho_5Ga_{2.6}Co_{0.4}$, $Er_5Ga_{2.6}Co_{0.4}$ and $Er_5Ga_{2.6}Fe_{0.4}$ samples.

Room-temperature data were collected on a STOE IPDSII diffractometer with MoK_α radiation and in the full reciprocal sphere. Numerical absorption correction was based on the crystal shapes that was originally derived from optical face indexing, but later optimized against equivalent reflections using the STOE *X-shape* software.[66] Structure refinements were performed using the *SHELXL* program.[67] Crystallographic data and refinement results are summarized in **Table 3.3 and 3.4.** The structure types obtained from single crystal solution agree well with the results of powder X-ray diffraction.

Table 3.3. Crystallographic data and refinement results for the Ho_5Ga_3, $Ho_5Ga_{2.6}Co_{0.4}$, $Er_5Ga_{2.6}Co_{0.4}$ and $Er_5Ga_{2.6}Fe_{0.4}$ samples (MoK_α radiation, 293K).

Sample	Ho_5Ga_3	$Ho_5Ga_{2.6}Co_{0.4}$	$Er_5Ga_{2.6}Co_{0.4}$	$Er_5Ga_{2.6}Fe_{0.4}$
Refined composition	Ho_5Ga_3	$Ho_5Ga_{2.6(1)}Co_{0.4(1)}$	$Er_5Ga_{2.6(1)}Co_{0.4(1)}$	$Er_5Ga_{2.5(1)}Fe_{0.5(1)}$
Space group	*P*6$_3$/*mcm*	*I*4/*mcm*	*I*4/*mcm*	*I*4/*mcm*
Scan mode	Omega			
Crystal size (mm)	0.0698 × 0.0582 × 0.0388	0.0720 × 0.0376 × 0.0362	0.0890 × 0.814 × 0.1229	0.0358 × 0.0381 × 0.0313
***a* (Å)**	8.521(1)	7.5971(1)	7.534(1)	7.530(1)
***c* (Å)**	6.411(1)	13.882(3)	13.770(3)	13.834(3)
Volume (Å^3)	403.1(1)	801.3(2)	781.5(2) Å3)	784.41(2)
ρ_{calc} (g/cm^3)	8.516	9.058	8.794	6.80
Z	2	4	4	4
Index ranges	$-11 \le h \le 10$ $-11 \le k \le 11$ $-8 \le l \le 8$	$-10 \le h \le 8$ $-9 \le k \le 10$ $-18 \le l \le 18$	$-14 \le h \le 14$ $-15 \le k \le 12$ $-5 \le l \le 6$	$-5 \le h \le 11$ $-10 \le k \le 11$ $-21 \le l \le 21$
2θ range (°)	5.86 to 58.32	5.86 to 58.32	5.86 to 58.40	5.84 to 68.82
Meas. Refl.	4280	4113	4371	2899
Ind. Refl.	221 (R_{int} = 0.0667)	311 (R_{int} = 0.0667)	311 (R_{int} = 0.0509)	466 (R_{int} = 0.0633)
Extinction coefficient	0.0037(8)	0.00104(8)	0.00120(8)	0.0006(1)
# of param.	17	17	17	18

Largest peak / hole (e/Å^3)	3.124/-2.771	6.653 /-1.918	4.063/-2.419	3.384/-3.057
Goodness-of-fit on |F^2|	1.259	1.213	1.266	1.156
R indices [I > 2σ(I)]	R_1 = 0.0576 wR_2 = 0.1135	R_1 = 0.0250 wR_2 = 0.0542	R_1 = 0.0255 wR_2 = 0.0440	R_1 = 0.0417 wR_2 = 0.0495

Table 3.4. Atomic coordinates and isotropic temperature parameters (U_{eq}) for Ho_5Ga_3, $Ho_5Ga_{2.5(1)}Co_{0.5(1)}$, $Er_5Ga_{2.5(1)}Co_{0.5(1)}$ and $Er_5Ga_{2.5(1)}Fe_{0.5(1)}$.

Atom	Site	Occupancy	x/a	y/b	z/c	U_{eq} (Å^2)
			Ho_5Ga_3			
Ho1	6*g*	1	0.2392(2)	0	1/4	0.025(1)
Ho2	4*d*	1	1/3	2/3	0	0.045(1)
Ga1	6*g*	1	0.5949(5)	0	1/4	0.059(2)
			$Ho_5Ga_{2.6(1)}Co_{0.4(1)}$			
Ho1	16*l*	1	0.1645(1)	0.6660(1)	0.1478(1)	0.012(1)
Ho2	4*c*	1	0	0	0	0.017(2)
Ga1	4*a*	1	0)	0	1/4	0.011(1)
Ga2/Co22	8*h*	0.82/0.18(6)	0.6237(2)	0.1237(2)	0	0.008(1)
			$Er_5Ga_{2.6(1)}Co_{0.4(1)}$			
Er1	16*l*	1	0.1666(1)	0.6661(1)	0.1467(1)	0.014(1)
Er2	4*c*	1	0	0	0	0.018(1)
Ga1	4*a*	1	0	0	1/4	0.011(2)
Ga2/Co22	8*h*	0.79/0.21(6)	0.6234(6)	0.1235(1)	0	0.010(1)
			$Er_5Ga_{2.5(1)}Fe_{0.5(1)}$			0.011(1)
Er1	16*l*	1	0.1676(1)	0.6676(1)	0.1470(1)	0.015(1)
Er2	4*c*	1	0	0	0	0.011(1)
Ga1	4a	1	0)	0	1/4	0.009(1)
Ga2/Fe22	8*h*	0.76/0.24(7)	0.6230(3)	0.1230(2)	0	0.009(1)

3.2.4 Electron Probe Microanalysis

Then quantitative elemental analysis of $Ho_5Ga_{2.6}Co_{0.4}$ was performed with an INCA-Energy-350 X-ray EDS spectrometer (Oxford Instruments) on the JEOL JSM-6480LV scanning electron microscope (20kV accelerating voltage, beam current 0.7 nA and beam diameter 50 μm). Signals averaged over three points per phase had estimated standard deviations of 1 at.% for Ho (measured by *L*-series lines), Co and Ga (measured by *K*-series lines).

3.2.5 Magnetometry

Magnetic measurements were performed using a Superconducting Quantum Interference Device (SQUID) on the Magnetic Property Measurement System (MPMS) magnetometer. Magnetization in a field-cooled (FC) mode for the polycrystalline Ho_5Ga_3 (cast), $Ho_5Ga_{2.9}Co_{0.1}$ (cast), $Ho_5Ga_{2.7}Co_{0.3}$ (annealed) and $Ho_5Ga_{2.6}Co_{0.4}$ (annealed) samples was measured in the 100 Oe field from 300 to 5K. Magnetization of other samples was not measured because of the significant amounts of secondary phases. Maxima in the derivatives of the magnetization with respect to temperature were taken as Curie (T_C) temperatures. The cusp temperature on the thermal magnetization curve was taken as the Neel (T_N) temperature of Ho_5Ga_3 (cast). Weiss temperature (θ_p) and effective magnetic moment per formula unit (μ_{eff}) were obtained by fitting the paramagnetic data to the Curie-Weiss law. The magnetocaloric effect for $Ho_5Ga_{2.7}Co_{0.3}$ and $Ho_5Ga_{2.6}Co_{0.4}$ was evaluated from the magnetization vs. field (*M* vs. *H*) curves measured around the ordering temperature with 5K steps. The magnetic field changed from 0 to 50 kOe in 2 kOe steps.

3.3 Results and Discussion

3.3.1 Composition, Structure and Stability of $Ho_5Ga_{3-x}Co_x$, $Er_5Ga_{3-x}Fe_x$, and $Er_5Ga_{3-x}Co_x$

Although the single crystal refinements yielded compositions nearly identical to the loaded ones within one standard deviation, relatively similar X-ray scattering factors and atomic sizes of Ga and Fe/Co made it difficult to reliably establish the compositions. To avoid any possible compositional bias resulting from refining mixed sites and also check for possible Ta contamination, electron probe microanalysis (EPMA) was performed on the bulk $Ho_5Ga_{2.6}Co_{0.4}$ sample. The resulting composition is $Ho_{5.00(4)}Ga_{2.60(2)}Co_{0.39(2)}$ (**Table 3.5)**, along with the single crystal X-ray data for comparison. No Ta signal was detected, suggesting no contamination from the Ta foil during annealing. Based on both the EPMA and X-ray results, we conclude that all the samples maintain the compositions used for their synthesis.

Table 3. 5. Composition of the $Ho_5Ga_{2.6}Co_{0.4}$ sample from the EPMA and single crystal X-ray refinement.

Loaded composition	EPMA	single crystal X-ray data
$Ho_5Ga_{2.6}Co_{0.4}$	$Ho_{5.00(4)}Ga_{2.60(2)}Co_{0.39(2)}$	$Ho_5Ga_{2.6(1)}Co_{0.4(1)}$

The cast Ho_5Ga_3, $Ho_5Ga_{2.9}Co_{0.1}$ and Er_5Ga_3 adopt the Mn_5Si_3-type structure, but large amounts of impurity can be found in cast Er_5Ga_3. It is worth mentioning that while both the cast Ho_5Ga_3 and $Ho_5Ga_{2.9}Co_{0.1}$ phases adopt the Mn_5Si_3-type structure, Ho_5Ga_3 is

air sensitive and $Ho_5Ga_{2.9}Co_{0.1}$ is not. The cast $Ho_5Ga_{2.7}Co_{0.3}$ and $Ho_5Ga_{2.6}Co_{0.4}$ samples were found to be mixture of Mn_5Si_3-type and Cr_5B_3-type phases, but annealing at 900°C for 1 week yielded pure Cr_5B_3-type phases, suggesting that a heat treatment is essential for transformation of the high-temperature Mn_5Si_3-type polymorph into the lower-temperature Cr_5B_3-type one. The cast $Ho_5Ga_{2.8}Co_{0.2}$ and $Ho_5Ga_{2.5}Co_{0.5}$ consisted of Mn_5Si_3-type and Cr_5B_3-type phases, and the annealed samples were found to be mixtures of the Cr_5B_3-type and Ho_3Ga_2 phases. The phase analysis sets the homogeneity limits of the Cr_5B_3-type phase to $0.3 \leq x \leq 0.4$ for $Ho_5Ga_{3-x}Co_x$. .Based on the homogeneity limits of $Ho_5Ga_{3-x}Co_x$, the $Er_5Ga_{2.6}Fe_{0.4}$ and $Er_5Ga_{2.6}Co_{0.4}$ samples were prepared by arc melting. They contained Mn_5Si_3-type (dominant) and Cr_5B_3-type phases similar to the cast $Ho_5Ga_{2.6}Co_{0.4}$ sample. Annealing at 900°C for 1 week yielded a pure Cr_5B_3-type phase only in $Er_5Ga_{2.6}Fe_{0.4}$, while a Ho_3Ga_2-type phase was observed in $Er_5Ga_{2.6}Co_{0.4}$ and it could not be eliminated by increasing the annealing time and/or temperature.

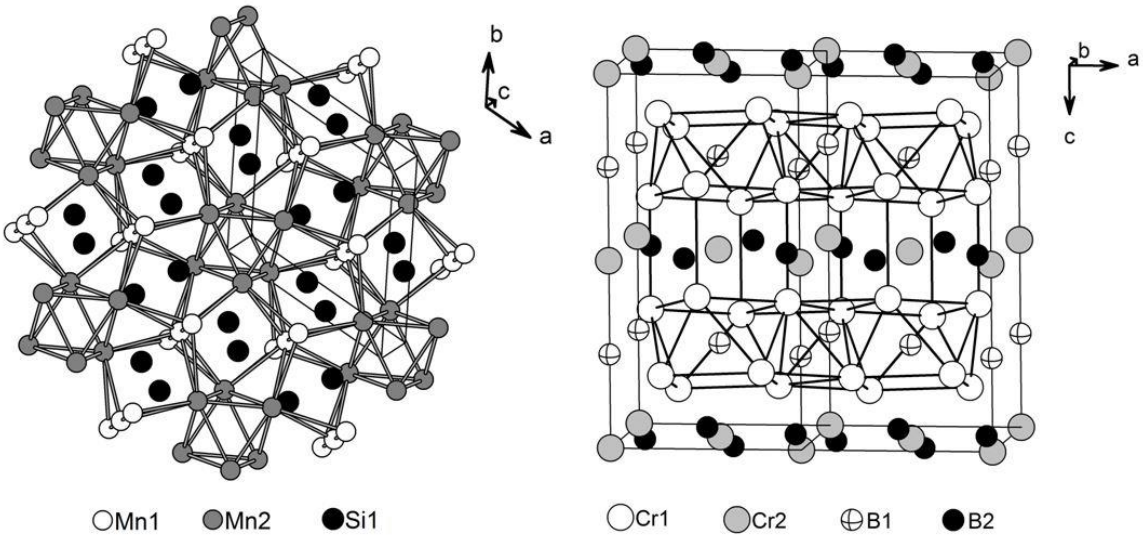

Figure 3.2. Crystal structures of the Mn_5Si_3 (left) and Cr_5B_3 (right) phases.

The Mn_5Si_3 and Cr_5B_3 structures have been described before[90,91] and only a brief summary is provided. The Mn_5Si_3 structure ($P6_3/mcm$) has two Mn sites (6*g* and 4*d*) and one Si site (6*g*): the Mn1 atoms on the 4*d* site make linear chains along the *c* axis and are neighbored with six Si atoms, which in turn form twisted trigonal prisms. Mn2 atoms on the 6*g* site form trigonal antiprisms, which share faces along the *c* axis. The face-shared trigonal antiprisms are closely bonded with the Mn1 linear chains. The Cr_5B_3-type structure ($I4/mcm$) has two independent Cr and B sites. The Cr1 atoms form two 3^2434 layers that are rotated by 45^o with respect to each other and they alternate along the *c* direction. Stacking of these layers produces trigonal (occupied by B2) and tetragonal (occupied by Cr2) prisms, tetragonal antiprisms (filled with B1) and empty tetrahedra. (**Figure 3.2**).

In the tetragonal Cr_5B_3-type $Ho_5Ga_{3-x}Co_x$, $Er_5Ga_{3-x}Fe_x$ and $Er_5Ga_{3-x}Co_x$ phases, Ga atoms are located on the B 8*h* and 4*a* sites, while larger *RE* atoms are located on the Cr 4*a* and 16*l* sites. As the atomic sizes of Fe and Co are comparable to that of Ga, Fe and Co are likely to occupy the two Ga sites. However, the Fe and Co atoms are only found on the Ga 8*h* site in $Ho_5Ga_{2.6}Co_{0.4}$, $Er_5Ga_{2.6}Fe_{0.4}$ and $Er_5Ga_{2.6}Co_{0.4}$. The preference of transition elements for the Ga 8*h* site is not fully understood, but it is in line with the site preference in other fully ordered phases, such as $RE_5Ni_2(Sb/Bi)$,[91] Gd_5Pd_2Bi,[91] $RE_5Pt_2(Sb/Bi)$,[92] $Gd_5Co_{1.73}Bi$,[93] Gd_5Au_2Bi,[94] and other $RE_5(Sb/Bi)_3$ compounds, in which some of Bi or Sb is partially substituted by a transition elements.[95–97]

The stabilization of the Cr_5B_3-type structure in the $Ho_5Ga_{3-x}Co_x$, $Er_5Ga_{3-x}Fe_x$ and $Er_5Ga_{3-x}Co_x$ samples stems from the decrease of the average atomic size of the Ga 8*h* site.

This can be also treated as an increase in the Ho or Er relative atomic size, which according to the diagram in **Figure 3.1**, should stabilize the Cr_5B_3-type structure. The atomic size difference between Er and Fe, Ho and Co is identical to that between Dy and Ga, which may explain why pure Cr_5B_3-type phases are formed in both samples. However, the atomic size difference between Er and Co is slightly larger than that between Er and Fe, and this may be a reason for the formation of the Ho_3Ga_2-type impurity in $Er_5Ga_{2.6}Co_{0.4}$ in addition to the Cr_5B_3-type one.

3.3.2 Magnetic Properties of the $Ho_5Ga_{3-x}Co_x$ Phases

The temperature-dependent magnetization data for the cast Ho_5Ga_3, $Ho_5Ga_{2.9}Co_{0.1}$ (Mn_5Si_3-type), annealed $Ho_5Ga_{2.7}Co_{0.3}$ and $Ho_5Ga_{2.6}Co_{0.4}$ (Cr_5B_3-type) phases are shown in **Figure 3.3.** The nature of the magnetic transition in Ho_5Ga_3 cannot be reliably established due to the lack of enough data points at lower temperatures. But $Ho_5Ga_{2.9}Co_{0.1,}$ $Ho_5Ga_{2.7}Co_{0.3}$ and $Ho_5Ga_{2.6}Co_{0.4}$ clearly undergo a ferromagnetic ordering. The transition temperature (T_t) of the Cr_5B_3-type phases are higher than those of the Mn_5Si_3-type one, additionally, the increasing Co amount has no effect on the transition temperature of two Mn_5Si_3-type phases, but raises the Curie temperature of Cr_5B_3-type phases (**Table 3.6).** In addition to the original ferromagnetic transitions, the annealed $Ho_5Ga_{2.9}Co_{0.1}$ and $Ho_5Ga_{2.7}Co_{0.3}$ exhibit an additional transition slightly below their Curie temperatures. While the nature of this transition could not be reliably established from our data, most likely it is a spin reorientation.

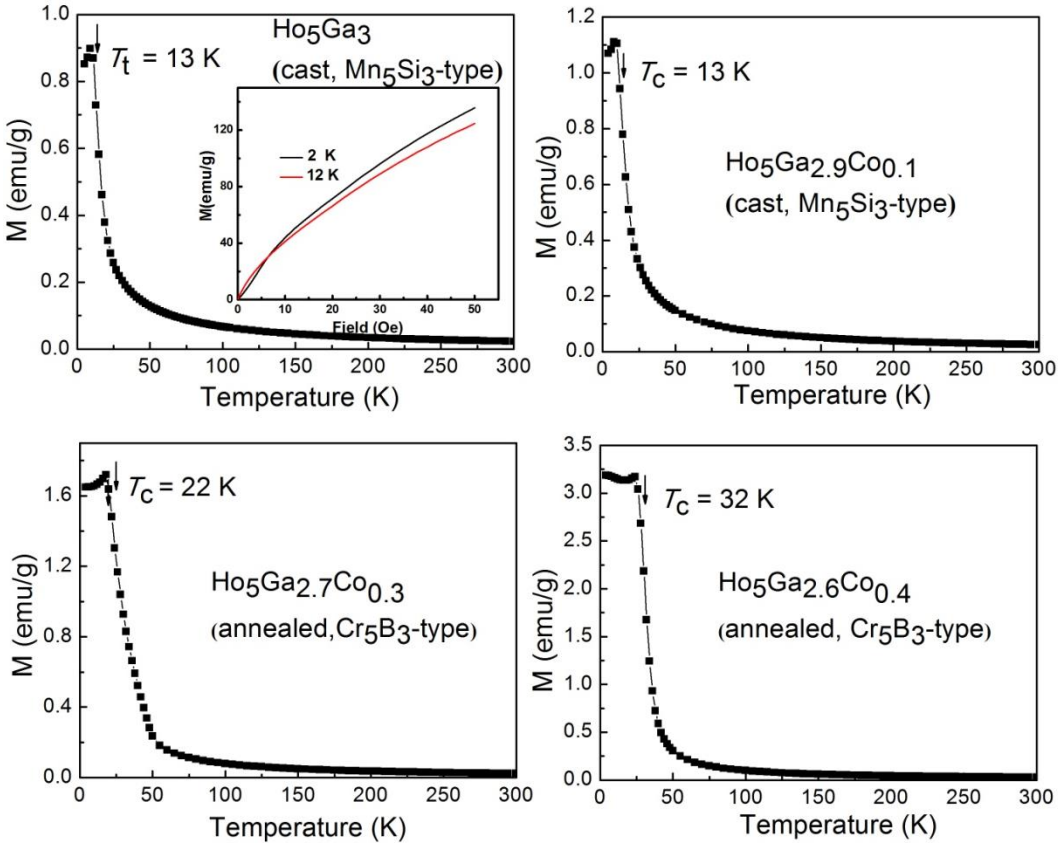

Figure 3.3. Magnetization vs. temperature for Ho_5Ga_3, $Ho_5Ga_{2.9}Co_{0.1}$, $Ho_5Ga_{2.7}Co_{0.3}$ and $Ho_5Ga_{2.6}Co_{0.4}$ .The inset is the magnetization vs. field for Ho_5Ga_3 at 2 and 12K.

Table 3.6. Magnetic transition temperature (T_t), calculated Weiss temperatures (θ_p) and effective magnetic moments per formula unit (μ_{eff}) for $Ho_5Ga_{3-x}Co_x$ (x = 0, 0.1, 0.3 and 0.4).

Composition	Treatment	T_t (K)	θ_p (K)	μ_{eff} (μ_B/f.u.)
Ho_5Ga_3	cast	13	-2.68	23.92
$Ho_5Ga_{2.9}Co_{0.1}$	cast	13	0.77	24.80
$Ho_5Ga_{2.7}Co_{0.3}$	annealed	22	17.86	23.90
$Ho_5Ga_{2.6}Co_{0.4}$	annealed	32	20.83	25.82

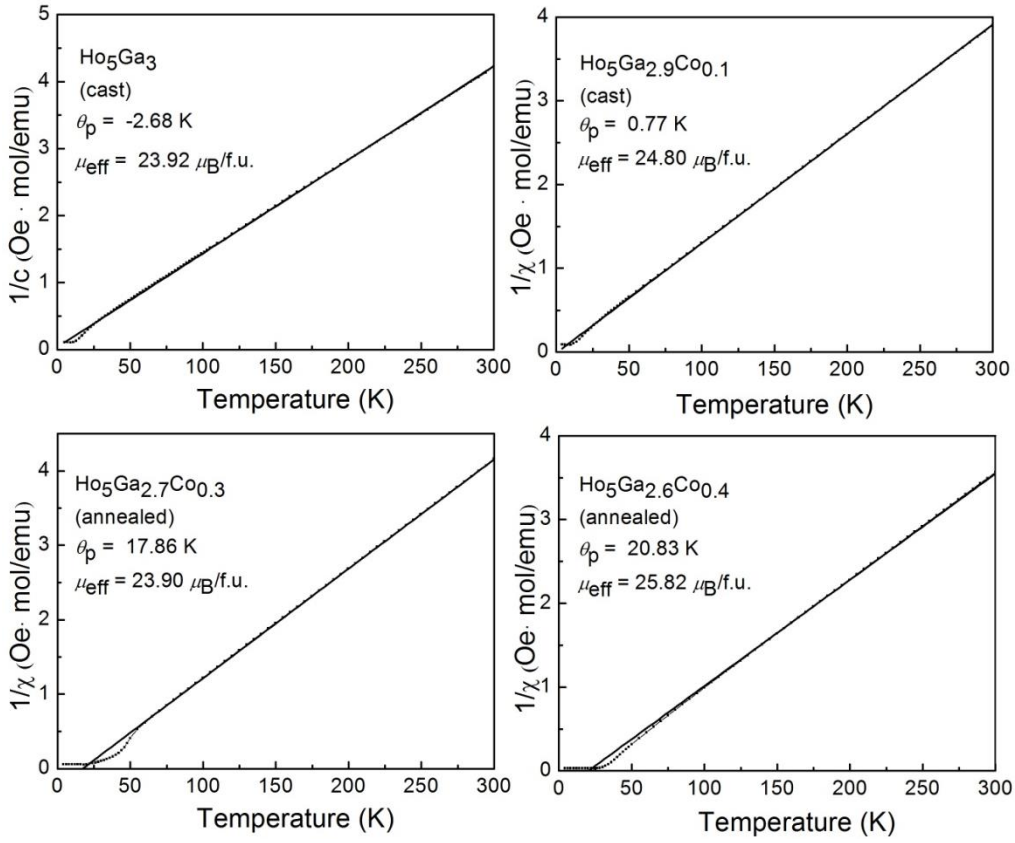

Figure 3.4. Inverse susceptibility vs. temperature for the $Ho_5Ga_{3-x}Co_x$ (x = 0, 0.1, 0.3 and 0.4) samples. Black lines indicate the linear fits to the Curie-Weiss formula.

Above the transition temperature, the magnetization follows the Curie-Weiss law (**Figure 3.4**). The Weiss temperatures (θ_p) and effective magnetic moments per formula unit (μ_{eff}) were extracted from the paramagnetic region data and are summarized in **Table 3.6.** The fit of Ho_5Ga_3 to the Curie-Weiss formula yielded a negative paramagnetic Weiss temperature θ_p = -2.68K, which suggested that the dominant interactions in Ho_5Ga_3 are antiferromagnetic in nature. To clarify the magnetic ground state of Ho_5Ga_3, we performed the M-H measurements at 2K and 12K **(the inset of Figure 3.3)**. Magnetization at 2K is lower than that at 12K below 7 kOe, but becomes larger at higher

fields. Both curves are not straight lines as expected for simple antiferromagnets. Additionally, below 7 kOe the magnetisation at 2K has a step-like feature characteristic of a metamagnetic transition. This can be associated with a partial spin reorientation and suggests a ground state with competing magnetic interactions, i.e. presence of some ferromagnetic ones in addition to the dominant antiferromagnetic ones. This spin reorientation can also explain a larger magnetization at 2K above 7 kOe.

In contrast to Ho_5Ga_3, $Ho_5Ga_{2.9}Co_{0.1}$ has a positive Weiss temperature, which suggests that the dominant interactions are ferromagnetic in nature. We did not investigate the ground state of $Ho_5Ga_{2.9}Co_{0.1}$ in details, but based on the similarity of their *M* vs *T* curves and structures, we can speculate that the magnetic interactions in $Ho_5Ga_{2.9}Co_{0.1}$ are likely to be similar to those in Ho_5Ga_3, with ferromagnetic ones being dominant. Both $Ho_5Ga_{2.7}Co_{0.3}$ and $Ho_5Ga_{2.6}Co_{0.4}$ order ferromagnetically. The calculated effective magnetic moments per formula unit are given **in Figure 3.4** and **Table 3.6**. If only Ho atoms were to carry magnetic moments of 10.61 μ_B (theoretical value for Ho^{3+}), the expected magnetic moment would 23.72 μ_B/f.u. Ho_5Ga_3 and $Ho_5Ga_{2.7}Co_{0.3}$ have magnetic moments close to that value, while $Ho_5Ga_{2.9}Co_{0.1}$ and $Ho_5Ga_{2.6}Co_{0.4}$ have slightly higher values, which may suggest some Co contribution contribution or more likely polarization of conduction *d*-electrons by localized Ho *f*-electrons. .

The magnetocaloric effect (MCE) of $Ho_5Ga_{2.7}Co_{0.3}$ and $Ho_5Ga_{2.6}Co_{0.4}$ was evaluated from the isothermal magnetization vs. field (*M* vs. *H*) measurements (**Fig 3.5a and c**). But before analyzing the MCE, we would like to discuss their saturation

magnetization curves below the Curie temperatures. For both samples, the magnetization does not saturate at 5K and 50 kOe, which is suggestive of some antiferromagnetic contributions. Additionally, at low temperatures and fields, there are metamagnetic transitions both in $Ho_5Ga_{2.7}Co_{0.3}$ and $Ho_5Ga_{2.6}Co_{0.4}$ similar to the one observed in Ho_5Ga_3, which proves that the ground state is not a purely ferromagnetic one but contains some antiferromagnetic interactions.

The magnetocaloric effect in terms of the isothermal magnetic entropy change, ΔS_{mag}, is derived using the numerical integration of the Maxwell equation:

$$\Delta S(\frac{T_1+T_2}{2})_{mag} = \sum_i \frac{M(T_2)_i - M(T_1)_i}{T_2 - T_1}\Delta H \qquad (3.1)$$

where ΔH is a magnetic field step and M_i and M_{i+1} are the values of magnetization at temperatures T_2 and T_1, respectively. The magnetic entropy change, ΔS_{mag}, for ΔH = 0-50 kOe is plotted in **Fig 3.5b and d**. As expected, ΔS_{mag} peaks around the Curie temperatures and has the maximum value of -12.7 J/(kgK) for $Ho_5Ga_{2.6}Co_{0.4.}$ The maximum value of ΔS_{mag} for $Ho_5Ga_{2.7}Co_{0.3}$ is smaller (-10.2 J/(kgK)), which indicates that the substitution of Co for Ga has a positive effect on the magnetocaloric effect. In addition, the value of -12.7 J/(kgK) for the magnetic entropy change indicates the presence of a conventional magnetocaloric effect (MCE) and implies absence of a first-order coupled magneto-structural transition.

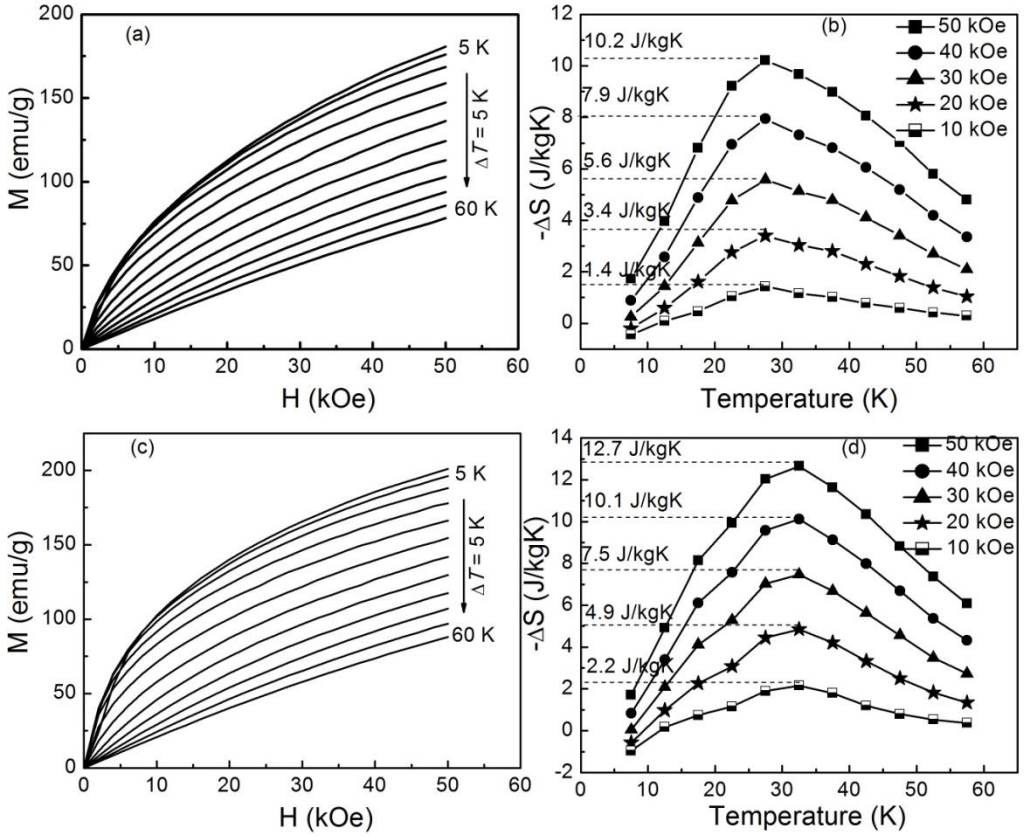

Figure 3.5. (a) Magnetization vs. magnetic field plots, **(b)** magnetic entropy changes as a function of temperature for $Ho_5Ga_{2.7}Co_{0.3}$; **(c)** Magnetization vs. magnetic field plots, **(d)** magnetic entropy changes as a function of temperature for $Ho_5Ga_{2.6}Co_{0.4}$.

3.4 Conclusion

The study of phase transitions in the $Ho_5Ga_{3-x}Co_x$, $Er_5Ga_{2.6}Fe_{0.4}$ and $Er_5Ga_{2.6}Co_{0.4}$ samples clearly show that the structures of RE_5Ga_3 are dictated by the relative size of the rare earth and Ga sites. Although a Cr_5B_3-type structure is non-existing for Ho_5Ga_3 and Er_5Ga_3, it can be easily stabilized through substitution of transition metals onto the Ga 8*h* site even at relatively small levels of x = 0.3 or 0.4. $Ho_5Ga_{2.9}Co_{0.1}$, $Ho_5Ga_{2.7}Co_{0.3}$ and $Ho_5Ga_{2.6}Co_{0.4}$ samples order ferromagnetically, while Ho_5Ga_3 orders likely

antiferromagnetically. The Co substitution strengthens the ferromagnetic interactions in the $Ho_5Ga_{3-x}Co_x$ system as evidenced from the increased Curie temperatures. The MCE in terms of the magnetic entropy changes, ΔS_{mag}, reaches the maximum of -12.7 J/(kgK) for the Cr_5B_3-type $Ho_5Ga_{2.6}Co_{0.4}$ phase around its Curie temperature. The moderate value of the magnetic entropy change implies the presence of a conventional MCE without a coupled structural transition.

Chapter 4. Structural and Magnetic Studies on the New Laves Phases *RE*($Co_{0.667}Ga_{0.333}$)$_2$ (*RE* = Gd, Tb, Dy, Ho, and Er). Magnetocaloric Effect of Gd($Co_{0.667}Ga_{0.333}$)$_2$

This chapter contains the material covered in the manuscript "Structural and Magnetic Studies on the New Laves Phases *RE*($Co_{0.667}Ga_{0.333}$)$_2$ (*RE* = Gd, Tb, Dy, Ho, and Er). Magnetocaloric Effect of Gd($Co_{0.667}Ga_{0.333}$)$_2$", which is currently being revised for publication in Acta Materialia. The experimental procedures, structure determinations, data interpretations, and manuscript were completed by the candidate. Dr. John E. Greedan participated in analysis of magnetic properties.

Several new $MgZn_2$-type Laves phases with the *RE*$(Co_{0.667}Ga_{0.333})_2$ compositions (*RE* = Gd, Tb, Dy, Ho, and Er) were obtained by arc-melting and subsequent annealing. Single crystals with the $MgZn_2$-type structure were extracted from the annealed *RE*$(Co_{0.667}Ga_{0.333})_2$ (*RE* = Gd, Tb, Dy, and Ho) alloys and Ga flux-grown $Er(Co_{0.667}Ga_{0.333})_2$ sample. Powder and single-crystal X-ray diffraction methods were used for the phase analysis and structural characterization. A decrease in the cell volume due to the lanthanide contraction is observed from $Gd(Co_{0.667}Ga_{0.333})_2$ to $Er(Co_{0.667}Ga_{0.333})_2$. *RE* atoms occupy the 4*f* site, while Co and Ga are in the 2*a* and 6*h* sites. Magnetic behavior of the hexagonal $MgZn_2$-type *RE*$(Co_{0.667}Ga_{0.333})_2$ phases strongly depends on the *RE*. Apparent ferromagnetic transition is observed for *RE* = Gd, Tb, and Dy, while the other two phases (*RE* = Ho and Er) seem to be ferrimagnetic. Magnetocaloric properties of the $Gd(Co_{0.667}Ga_{0.333})_2$ phase were measured; the small isothermal magnetic entropy change (ΔS_{iso}) value of -4.94 J/(kgK) suggests a conventional magnetocaloric effect.

4.1 Introduction

Nowadays, conventional vapor-based refrigeration is the main cooling technique around the world. However, some distinct drawbacks such as its low efficiency and environmental impact promote search for alternative techniques.[98] One of the promising alternatives is magnetic refrigeration, whose origin can be traced to 1881, when Warburg discovered the magnetocaloric effect (MCE) in pure iron.[8] Recently, refrigerator prototypes with magnetocaloric materials as active cooling media were developed.[9,99]

When compared to vapor-based refrigeration, the magnetic refrigeration offers a higher efficiency of 40-60%, smaller volume and lower noise.[52]

Widespread adoption of magnetic refrigeration will depend on the performance of magnetocaloric materials, namely on their MCE values. Discovery of the giant magnetocaloric effect (GMCE) in $Gd_5Si_2Ge_2$ was a significant breakthrough as the MCE was significantly enhanced.[12] $Gd_5Si_2Ge_2$ undergoes a first-order magneto-structural phase transition, and the total entropy change includes not only a magnetic entropy contribution, but also a structural one. Similar studies on the *RE*Co_2-based (*RE* = 4*f* rare-earth elements) compounds revealed presence of the GMCE in the $DyCo_2$, $HoCo_2$, and $ErCo_2$ phases[54]. But in contrast to $Gd_5Si_2Ge_2$, a first-order phase transition (FOPT) associated with the GMCE in $DyCo_2$, $HoCo_2$, and $ErCo_2$ stems from the itinerant electron metamagnetism (IEM), which is also observed in the $La(Fe,Si)_{13}$ magnetocaloric phases.[100] Although all of the *RE*Co_2 phases belong to the Laves family and adopt the cubic $MgCu_2$-type structure, only $DyCo_2$, $HoCo_2$, and $ErCo_2$ display a GMCE, while the other *RE*Co_2 ones exhibit a conventional MCE because of FOPT absence.[7]

The magnetocaloric research on the *RE*Co_2-based phases focused primarily on the substitution of *RE* or Co, i.e. on $(RE_{1-x}RE'_x)Co_2$ and $RE(Co_{1-x}M_x)_2$, where *RE* and *RE*′ are the original and substituting rare-earth elements, respectively, while *M* is a nonmagnetic or magnetic element with atomic radius similar to that of Co.[54,57–60] To date, the majority of the *RE*Co_2-based compounds studied had the structure of the pristine *RE*Co_2, as Co substitution levels were kept low in order to preserve the $MgCu_2$-type structure. The

question may be asked: when the *M* content in $RE(Co_{1-x}M_x)_2$ is increased further, can new magnetocaloric phases with different structures be obtained?

Herein, we explore this question on the $RE(Co_{1-x}Ga_x)_2$ systems. Literature data suggest the possibility of obtaining a hexagonal $MgZn_2$-type Laves phase in $RE(Co_{1-x}Ga_x)_2$.[63,101] However the compositional diagram is not well established; secondary phases appear above $x = 0.2$ in $RE(Co_{1-x}Ga_x)_2$ (x = 0-0.3), and one of them is reported to adopt the hexagonal $MgZn_2$-type structure, but its composition is not given.[63] A hexagonal $MgZn_2$-type structure is also obtained in the $Gd(Co_{1-x}Al_x)_2$ system for $0.49\pm0.01 \leq x \leq 0.73\pm0.03$, otherwise, the cubic $MgCu_2$-type Laves phases forms.[101] Since Ga and Al are in the same group and have similar atomic radii, we propose that hexagonal $MgZn_2$-type Laves phases can be found both in the Al- and Ga-substituted $RECo_2$ phases. Additionally, the new materials may possess interesting magnetocaloric properties.

It is worth mentioning that magnetic properties are quite different in $RECo_2$ for the light and heavy *RE*.[7] Since the GMCE was discovered in the latter compounds, we focus on $RE(Co_{1-x}Ga_x)_2$ with *RE* = Gd, Tb, Dy, Ho, and Er in our study. Based on the previous work, the hexagonal $MgZn_2$-type Laves phases should exist for $x > 0.2$.[63] In addition, $RECo_2$ and $RE(Co_{0.5}Ga_{0.5})_2$ phases were reported to adopt cubic and orthorhombic structure, respectively, indicating that the symmetry decreases as x increases from 0 to 0.5 in $RE(Co_{1-x}Ga_x)_2$.[61,102] Based on these observation, hexagonal $MgZn_2$-type Laves phases in the $RE(Co_{1-x}Ga_x)_2$ systems are likely to exist in a limited x range, tentatively for $0.2 < x < 0.5$. Our current work indicates that the hexagonal $MgZn_2$-type Laves phase can be successfully obtained at $x = 0.333$, i.e. $RE(Co_{0.667}Ga_{0.333})_2$ for *RE* = Gd, Tb, Dy, Ho, and

Er. In this paper, we describe synthesis, structure and magnetic properties of the new *RE*$(Co_{0.667}Ga_{0.333})_2$ compounds.

4.2 Experimental

4.2.1 Synthesis

4.2.1.1 Arc-melting and Heat Teatment

The starting materials for the *RE*$(Co_{0.667}Ga_{0.333})_2$ (*RE* = Gd, Tb, Dy, Ho, and Er) phases were *RE* (99.9 wt.%, distilled grade, Metall Rare Earth Limited, China), Co (99.98 wt.%, Alfa Aesar), and Ga (99.999 wt.%, Alfa Aesar) pieces. The *RE*$(Co_{0.667}Ga_{0.333})_2$ alloys with a total mass of ~3 g were arc-melted 3 times to ensure homogeneity. During re-melting process, the samples were turned over as fast as possible to prevent sample cracking during cooling. The cast alloy buttons were wrapped in Ta foil, sealed in evacuated silica tubes, heated at 100^{o}C/hour to a target temperature and annealed for 72 hours. The annealing temperatures were 850^{o}C, 950^{o}C, 1000^{o}C, 1000^{o}C, and 1000^{o}C at 100^{o}C/hour for with *RE* = Gd, Tb, Dy, Ho, and Er, respectively. Subsequently, all the annealed samples were quenched in cold water.

4.2.1.2 Single Crystal Growth from Ga Flux

Small single crystals could be found in all samples except for the annealed Er$(Co_{0.667}Ga_{0.333})_2$. To obtain single crystals suitable for X-ray diffraction, Er, Co, and Ga pieces in the 3:2:2 ratio were placed into a set of alumina crucibles with a frit in-between

and sealed in a carbon-coated evacuated silica tube. The sample was heated according to the following temperature profile and subsequently centrifuged:

$$25°C \xrightarrow{100°C/h} 1050°C\ (dwell\ 72\ hours) \xrightarrow{3°C/h} 850°C\ (\ dwell\ 1\ week)$$
$$\rightarrow centrifugation$$

Small single crystals with the hexagonal $MgZn_2$-type structure could be picked up for the X-ray diffraction.

4.2.2 X-ray Analysis

Room-temperature phase analysis of the cast and annealed *RE*$(Co_{0.667}Ga_{0.333})_2$ (*RE* = Tb, Dy, Ho, and Er) samples were performed on a PANalytical X'Pert Pro diffractometer equipped with a linear X'Celerator detector and Cu$K\alpha_1$ radiation. The data for the Gd-containing alloys were collected using the Co$K\alpha$ radiation in order to eliminate the Gd fluorescence present for the Cu$K\alpha$ radiation. The refinement of lattice parameters was performed with the *Rietica* program.[89]

All the cast *RE*$(Co_{0.667}Ga_{0.333})_2$ alloys contained more than one phases. The cast Er$(Co_{0.667}Ga_{0.333})_2$ sample was composed of the hexagonal ($P6_3/mmc$) and cubic ($Fd\bar{3}m$) Laves phases, while other *RE*-based compounds contained large amounts of unidentified secondary phases. In addition, the amount of impurities increased from the Ho- to Gd-based phases. After annealing, the *RE*$(Co_{0.667}Ga_{0.333})_2$ samples contained only a hexagonal $MgZn_2$-type phase, except for Tb$(Co_{0.667}Ga_{0.333})_2$, where a secondary $CeNi_3$-type phase, with a weight percentage of 4%, was detected. A single crystal with the hexagonal $CeNi_3$-

type ($P6_3/mmc$) structure and lattice parameters of a = 5.1094(7) Å and c = 16.298(3) Å was extracted from the $Tb(Co_{0.667}Ga_{0.333})_2$ boule. The Inorganic Crystal Structure Database contains $TbCo_{2.4}Ga_{0.6}$ with the $CeNi_3$-type structure and practically the same unit cell constants.[103] Therefore, we propose that the composition of the secondary phase in the $Tb(Co_{0.667}Ga_{0.333})_2$ is close to $TbCo_{2.4}Ga_{0.6.}$ The unit cell dimensions derived from the Rietveld refinement (*Rietic*a program) [89] for the $MgZn_2$-type phases are summarized in **Table 4.1**. A decrease in the cell volume from $Gd(Co_{0.667}Ga_{0.333})_2$ to $Er(Co_{0.667}Ga_{0.333})_2$ reflects the lanthanoid contraction.

Table 4.1. Lattice parameters from the Reitveld powder refinement for the annealed $RE(Co_{0.667}Ga_{0.333})_2$ (*RE* = Gd, Tb, Dy, Ho, and Er; space group $P6_3/mmc$).

annealed sample	a, Å	c, Å	V, Å^3
$Gd(Co_{0.667}Ga_{0.333})_2$	5.2668(2)	8.5009(3)	204.22(1)
$Tb(Co_{0.667}Ga_{0.333})_2$	5.2346(2)	8.4658(4)	200.89(2)
$Dy(Co_{0.667}Ga_{0.333})_2$	5.2179(4)	8.4458(7)	199.14(3)
$Ho(Co_{0.667}Ga_{0.333})_2$	5.2064(1)	8.4228(1)	197.72(1)
$Er(Co_{0.667}Ga_{0.333})_2$	5.1851(1)	8.4115(1)	195.85(1)

Single crystals with the $MgZn_2$-type structure were extracted from the annealed $RE(Co_{0.667}Ga_{0.333})_2$ (*RE* = Gd, Tb, Dy, and Ho) alloys and flux-grown $Er(Co_{0.667}Ga_{0.333})_2$ sample. Single-crystal diffraction data were collected on a STOE IPDS II diffractometer with the Mo $K\alpha$ radiation at room temperature. Numerical absorption corrections were based on the crystal shapes that were originally derived from optical face indexing but

later optimized against equivalent reflections using the STOE X-shape software. Crystal structures were refined using the SHELXL program.[67]

Crystallographic and refinement data for the *RE*($Co_{0.667}Ga_{0.333}$)$_2$ crystals are summarized in **Table 4.2 and 4.3**, confirming the structural parameters obtained from the powder X-ray diffraction**.** The hexagonal $MgZn_2$-type structure (*P*6_3/mmc) has three crystallographic sites: 2*a*, 4*f* and 6*h*. *RE* atoms take the 4*f* site, Co and Ga are in 2*a* and 6*h* sites but their occupancies could not be reliably established from the X-ray diffraction due to their similar atomic scattering factors. The published data for the analogous *RE*Co_2-*RE*Al_2 phases give a random distribution of Co and Al on the 2*a* and 6*h* sites.[104] Similarly, we assume a statistical Co/Ga mixing in *RE*($Co_{0.667}Ga_{0.333}$)$_2$. In case of the crystals obtained from the Er:Co:Ga flux, the unit cell dimensions were abnormally large, suggesting a composition richer in Ga than Er($Co_{0.667}Ga_{0.333}$)$_2$. These results suggest that the targeted $MgZn_2$-type phase possesses an extended homogeneity range.

Table 4.2. Crystallographic data and refinement results for the annealed $RE(Co_{0.667}Ga_{0.333})_2$ (*RE* = Gd, Tb, Dy, Er, and Ho) (MoK_α radiation, 293K).

Sample composition	**$Gd(Co_{0.667}Ga_{0.333})_2$**	**$Tb(Co_{0.667}Ga_{0.333})_2$**	**$Dy(Co_{0.667}Ga_{0.333})_2$**	**$Ho(Co_{0.667}Ga_{0.333})_2$**	**$Er(Co_{0.667}Ga_{0.333})_2$**
Space group	$P6_3/mmc$	$P6_3/mmc$	$P6_3/mmc$	$P6_3/mmc$	$P6_3/mmc$
Scan mode			Omega		
Crystal dimensions (mm^3)	0.0462 x 0.0522 x 0.3819	0.0978 x 0.0506 x 0.0709	0.0455 x 0.1404 x 0.0241	0.0760 x 0.0780 x 0.0440	0.0594 x 0.0542 x 0.0475
***a* (Å)**	5.2593(7)	5.2273(7)	5.2084(7)	5.1892(7)	5.2555(7)
***c* (Å)**	8.490(2)	8.457(2)	8.456(2)	8.411(2)	8.438(2)
Volume ($Å^3$)	203.37(6)	200.13(6)	198.67(5)	196.15(5)	201.85(6)
ρ_{calc} (g/cm^3)	9.221	9.426	9.615	9.821	9.620
Z	4	4	4	4	4
2θ range (°)	8.94 to 58.18	9.00 to 58.36	9.04 to 58.22	9.08 to 57.96	8.96 to 58.06
Meas. Refl.	2053	2020	2267	2122	2019
Ind. Refl.	129 (R_{int} = 0.0824)	128 (R_{int} = 0.0841)	125 (R_{int} = 0.0601)	124 (R_{int} = 0.0595)	128 (R_{int} = 0.0915)
Extinction coefficient	0.015(1)	0.008(2)	0.023(2)	0.0087(9)	0.019(2)
# of param.	12	12	12	12	12
Largest peak / hole ($e/Å^3$)	1.824/-1.370	2.521/-3.443	2.021/-0.914	1.706/-1.036	2.285/-1.058
Goodness-of-fit on $\|F^2\|$	1.319	1.137	1.339	1.226	1.228
R indices [I > 2σ(I)]	R_1 = 0.0280 wR_2 = 0.0326	R_1 = 0.0303 wR_2 = 0.0690	R_1 = 0.0185 wR_2 = 0.0383	R_1 = 0.0193 wR_2 = 0.0333	R_1 = 0.0273 wR_2 = 0.0569
R indices [all data]	R_1 = 0.0430 wR_2 = 0.0343	R_1 = 0.0420 wR_2 = 0.0721	R_1 = 0.0254 wR_2 = 0.0402	R_1 = 0.0311 wR_2 = 0.0355	R_1 = 0.0335 wR_2 = 0.0587

Table 4.3. Atomic coordinates and isotropic displacement parameters (U_{eq}) for annealed $RE(Co_{0.667}Ga_{0.333})_2$ (*RE* = Gd, Tb, Dy, Er, and Ho).

Atom	Site	Occupancy	x/*a*	y/*b*	z/*c*	U_{eq} (Å^2)
			$Gd_3(Co_{0.667}Ga_{0.333})_2$			
Gd1	4*f*	1	1/3	2/3	0.0617(1)	0.009(1)
Co1/Ga11	2a	0.667/0.333*	0	0	0	0.003(1)
Co2/Ga22	6*h*	0.667/0.333*	0.8326(2)	0.6652(5)	1/4	0.009(1)
			$Tb(Co_{0.667}Ga_{0.333})_2$			
Tb1	4*f*	1	1/3	2/3	0.0620(1)	0.010(1)
Co1/Ga11	2a	0.667/0.333*	0	0	0	0.005(1)
Co2/Ga22	6*h*	0.667/0.333*	0.8323(3)	0.6645(6)	1/4	0.011(1)
			$Dy(Co_{0.667}Ga_{0.333})_2$			
Dy1	4*f*	1	1/3	2/3	0.0623(1)	0.009(1)
Co1/Ga11	2a	0.667/0.333*	0	0	0	0.004(1)
Co2/Ga22	6*h*	0.667/0.333*	0.8320(2)	0.6639(2)	1/4	0.009(1)
			$Ho(Co_{0.667}Ga_{0.333})_2$			
Ho1	4*f*	1	1/3	2/3	0.0626(1)	0.010(1)
Co1/Ga11	2a	0.667/0.333*	0	0	0	0.004(1)
Co2/Ga22	6*h*	0.667/0.333*	0.8316(2)	0.6632(4)	1/4	0.009(1)
			$Er(Co_{0.667}Ga_{0.333})_2$			
Er1	4*f*	1	1/3	2/3	0.0605(1)	0.009(1)
Co1/Ga11	2a	0.667/0.333*	0	0	0	0.008(1)
Co2/Ga22	6*h*	0.667/0.333*	0.8317(2)	0.6633(4)	1/4	0.010(1)

* Co/Ga occupancy is not refined

4.2.3 Magnetometry

Magnetic measurements were performed using a Superconducting Quantum Interference Device (SQUID) on the Magnetic Property Measurement System (MPMS). Magnetization in a field-cooled (FC) mode for the annealed polycrystalline $RE(Co_{0.667}Ga_{0.333})_2$ samples was measured under a 100 Oe field from 300 to 5K.

Magnetization of cast samples was not measured because of the significant amounts of other phases. Maxima in the derivatives of the magnetization with respect to temperature were taken as Curie (T_C) temperatures. The cusp temperature on the thermal magnetization curve was taken as the Neel (T_N) temperature. Weiss temperatures (θ_p) and effective magnetic moments per formula unit (μ_{eff}) were obtained by fitting the paramagnetic data to the Curie-Weiss law. The magnetocaloric effect of $Gd(Co_{0.667}Ga_{0.333})_2$ was evaluated from the magnetization vs. field (*M* vs. *H*) curves measured around T_C with 5K steps. The magnetic field changed from 0 to 50 kOe in 2 kOe steps. Magnetic entropy change was calculated using the Maxwell equation.

4.3 Results and Discussion

4.3.1 Structural Transformations upon Annealing in $RE(Co_{0.667}Ga_{0.333})_2$

The structural transformations of $Er(Co_{0.667}Ga_{0.333})_2$ upon annealing at 1000°C for 72 hours could be characterized as a $Fd\bar{3}m$-to-$P6_3/mmc$ transformation. The arc-melted $Er(Co_{0.667}Ga_{0.333})_2$ sample contained both the cubic ($Fd\bar{3}m$) and hexagonal ($P6_3/mmc$) phases, with the latter being the major phase (66.5 wt.%). The minor cubic phase disappeared after annealing. Both the cubic and hexagonal phases belong to the Laves pseudobinary phases. Formation of the hexagonal $MgZn_2$-type $Er(Co_{0.667}Ga_{0.333})_2$ phase resembles transformations in the $REAl_2$-RET_2 (T = 3*d* elements) systems,[101] and can be described as a peritectic reaction between the cubic $MgCu_2$-type phase and Ga-rich liquid when annealing at 1000°C.

In some respects, the phase transformation in the other *RE*($Co_{0.667}Ga_{0.333}$)$_2$ (*RE* = Gd, Tb, Dy, and Ho) is similar to that in Er($Co_{0.667}Ga_{0.333}$)$_2$. However, some unidentified phases were observed in the cast samples besides the cubic and hexagonal phases, and the complexity of powder patterns increased from Ho to Gd. Similar to the Er($Co_{0.667}Ga_{0.333}$)$_2$ alloy, pure hexagonal $MgZn_2$-type phases were obtained only after annealing. It is worth mentioning that the annealing temperature increased from 850°C for Gd($Co_{0.667}Ga_{0.333}$)$_2$ to 1000°C for Er($Co_{0.667}Ga_{0.333}$)$_2$. Such a trend was observed in other *RE*-based alloys and could be attributed to higher melting temperatures of heavier rare-earths.

Transformation between the cubic and hexagonal Laves phases with the AB_2 stoichiometry has been extensively analyzed in terms of average electron density, atomic size ratios (r_A/r_B), electronegativity difference, temperature, composition, and pressure.[53,101,105–108] However, a unified theory for predicting or explaining the structural types of all the Laves phases is not developed yet. In our current study, all *RE*Co_2 phases adopt the cubic $MgCu_2$-type structure, despite different *RE* sizes. Substitution of Ga for Co will not alter the relative geometric parameters significantly as Co and Ga have similar atomic radii (r_{Co} = 1.25 Å vs. r_{Ga} = 1.26 Å).[109] Most likely, adoption of the $MgZn_2$-type structure instead of the $MgCu_2$-type one by *RE*($Co_{0.667}Ga_{0.333}$)$_2$ is driven by changes in the valence electron count. This conclusion will be verified by detailed electronic structure analysis. It is worth mentioning that electronic factors do not always dictate the structural stability. In systems such as RE_5Ga_3 phases, where geometric effects are important, even small perturbations to the relative atomic sizes may yield different structures. In our previous work on the $RE_5Ga_{3-x}Co_x$ phases, we have proven that point by

selectively stabilizing either Mn_5Si_3- or Cr_5B_3-type structure through fine tuning of the effective atomic size of the Ga/Co site.[69]

4.3.2 Magnetic Properties of the Annealed *RE*$(Co_{0.667}Ga_{0.333})_2$ Phases

The temperature-dependent magnetization of the annealed *RE*$(Co_{0.667}Ga_{0.333})_2$ (*RE* = Gd, Tb, Dy, Ho, and Er) samples is shown in **Figure 4.1.** Gd$(Co_{0.667}Ga_{0.333})_2$, Dy$(Co_{0.667}Ga_{0.333})_2$ and Ho$(Co_{0.667}Ga_{0.333})_2$ undergo a ferromagnetic or ferrimagnetic ordering with T_C of 150, 55, and 36K, respectively. Additionally, the magnetic transition of Gd$(Co_{0.667}Ga_{0.333})_2$ phase is very sharp, which may be interesting for magnetocaloric applications. The temperature-dependent magnetization of Tb$(Co_{0.667}Ga_{0.333})_2$ contains two magnetic transitions at 95 and 195K. The experimental transition temperature (T_t) of Er$(Co_{0.667}Ga_{0.333})_2$ is 15K, but the nature of the magnetic transition could not be reliably established due to the lack of enough data points at lower temperatures.

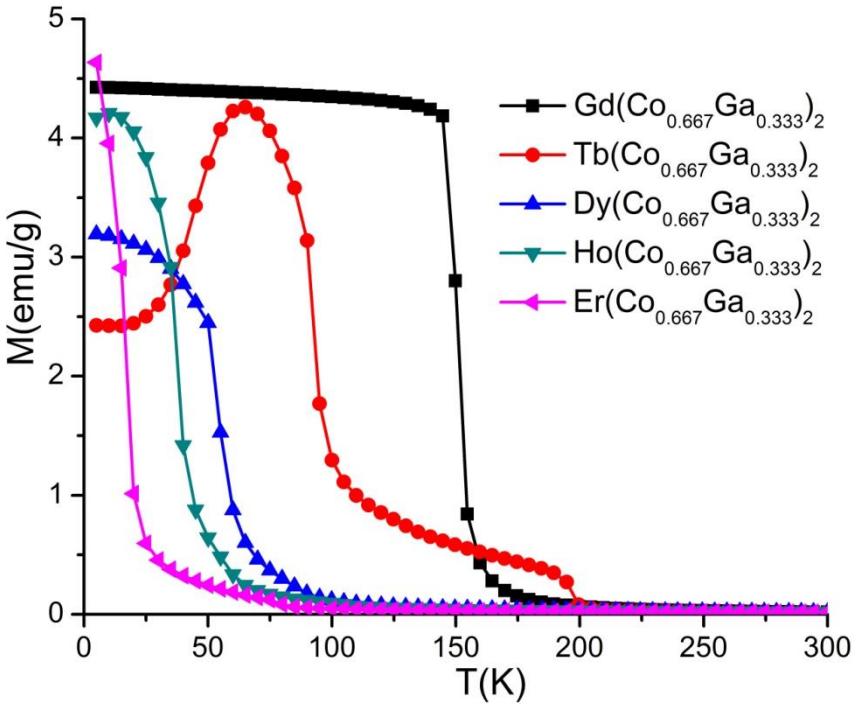

Figure 4.1. Magnetization vs. temperature for the annealed $RE(Co_{0.667}Ga_{0.333})_2$ samples (*RE* = Gd, Tb, Dy, Ho, and Er) under a magnetic field of 100 Oe.

The magnetic susceptibility of the $RE(Co_{0.667}Ga_{0.333})_2$ (*RE* = Gd, Tb, Dy, Ho, and Er) samples was fitted to the Curie-Weiss law at higher temperatures (**Figure 4.2**). The Weiss temperatures (θ_p) and effective magnetic moments per formula unit (μ_{eff}) extracted from the paramagnetic regions are summarized in **Table 4.4**. For $Er(Co_{0.667}Ga_{0.333})_2$, the fit to the Curie-Weiss formula yields a negative paramagnetic Weiss temperature of -9.82 K, which indicates that the dominant interactions are probably antiferromagnetic, suggesting that the order might be ferrimagnetic in nature. On the other hand, the other four phases have positive θ_ps, although for the Ho materials, the ratio θ_p/T_t is < 1, which is atypical for a simple ferromagnet. Magnetization of $Gd(Co_{0.667}Ga_{0.333})_2$ follows the Curie-

Weiss law to just above the Curie temperatures, which is typical for ferromagnetism, while for the other four phases the Curie-Weiss law is obeyed only at temperatures significantly higher than their transition temperatures. In addition, an upward curvature of the $1/\chi$-T curves between the T_t and the beginning of the Curie-Weiss regime could be taken as evidence of dominant ferrimagnetic interactions in $RE(Co_{0.667}Ga_{0.333})_2$ (*RE* = Ho and Er). The Tb data are clearly dominated by the impurity phase and the situation for Dy is not so clear, where an upward curvature is absent.

The magnetic interactions in $RE(Co_{0.667}Ga_{0.333})_2$ (*RE* = Gd, Tb, Dy, Ho, and Er) are likely of the Ruderman-Kittel-Kasuya-Yoshida (RKKY) type.[2,1] In the molecular field approximation the magnitude of the Weiss constant is identical with the transition temperature.[110] Since the annealed $RE(Co_{0.667}Ga_{0.333})_2$ (*RE* = Gd, Tb, Dy, Ho, and Er) samples adopt the identical structure, where *RE* have the same valence, i.e. RE^{3+}, their T_t should vary quantitatively with $(g\text{-}1)^2J(J+1)$, i.e. the de Gennes function.[4] Therefore, the calculated transition temperatures (de Gennes in **Figure 4.3**) are evaluated in terms of the de Gennes function by assuming that the calculated T_t of $Gd(Co_{0.667}Ga_{0.333})_2$ equals the experimental one, i.e. 150K. As shown in **Figure 4.3**, de Gennes decreases from $Gd(Co_{0.667}Ga_{0.333})_2$ to $Er(Co_{0.667}Ga_{0.333})_2$. Thus in the $Tb(Co_{0.667}Ga_{0.333})_2$ sample, the magnetic transition at 95K results likely from the $MgZn_2$-type phase, while the other one at 195K is from the secondary phase, i.e. $CeNi_3$-type impurity.

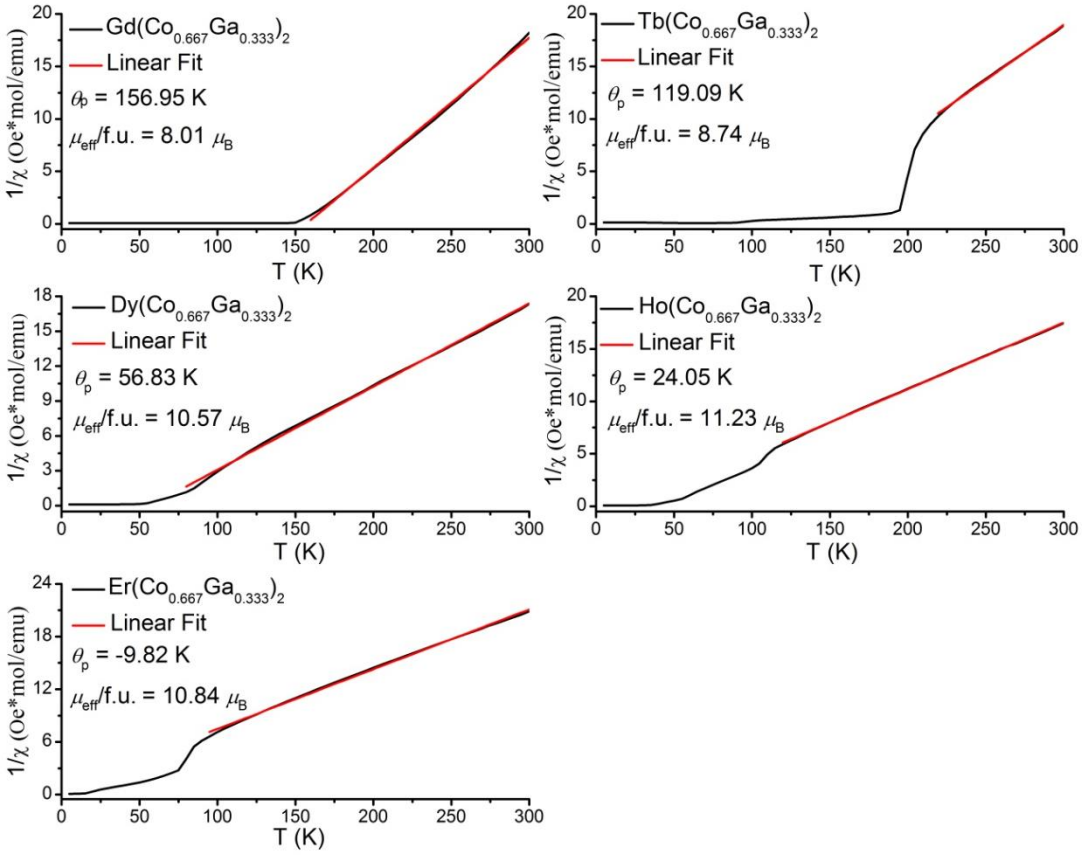

Figure 4.2. Inverse susceptibility vs. temperature for the annealed $RE(Co_{0.667}Ga_{0.333})_2$ samples (*RE* = Gd, Tb, Dy, Ho, and Er). The red lines are linear fits to the Curie-Weiss law.

Figure 4.3 also compares the experimental transition and Weiss temperature with those calculated using the de Gennes function (de Gennes) for the rare-earth metals heavier than Gd. In the de Gennes model, which is essentially the mean field theory, $T_t = \theta_p$. In general, for a true ferromagnet, the ratio θ_p/T_t is ~ 1.1 or so, which seems to hold for Gd and Dy. The Tb case is clouded by the presence of an impurity phase but the θ_p/T_t ratio is still > 1. However, for Ho and Er, both T_t and θ_p/T_t ratio deviate in a negative sense from the predictions of the de Gennes function based on the numbers for Gd. θ_p for Er is

actually negative, a property often taken as evidence for ferrimagnetic behaviour. The point is that as we move along the *RE* series, both T_t and the θ_p/T_t ratio begin to deviate, apparently systematically, from those expected for a simple ferromagnet, i.e. the Gd case.

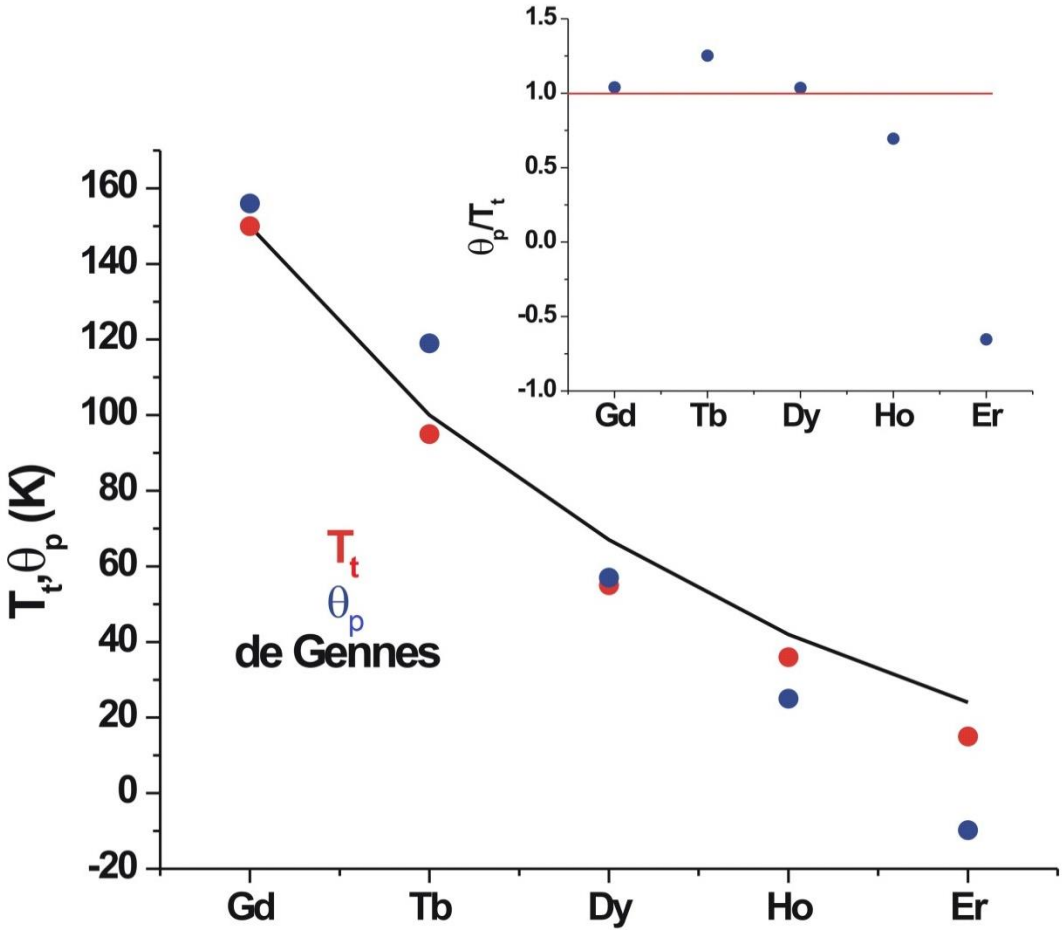

Figure 4.3. Comparison of the predicted de Gennes with observed transition temperature (T_t) and Weiss temperature (θ_p). The inset shows θ_p/T_t which deviates strongly from the mean field theory value of 1 (red line) for Ho and Er.

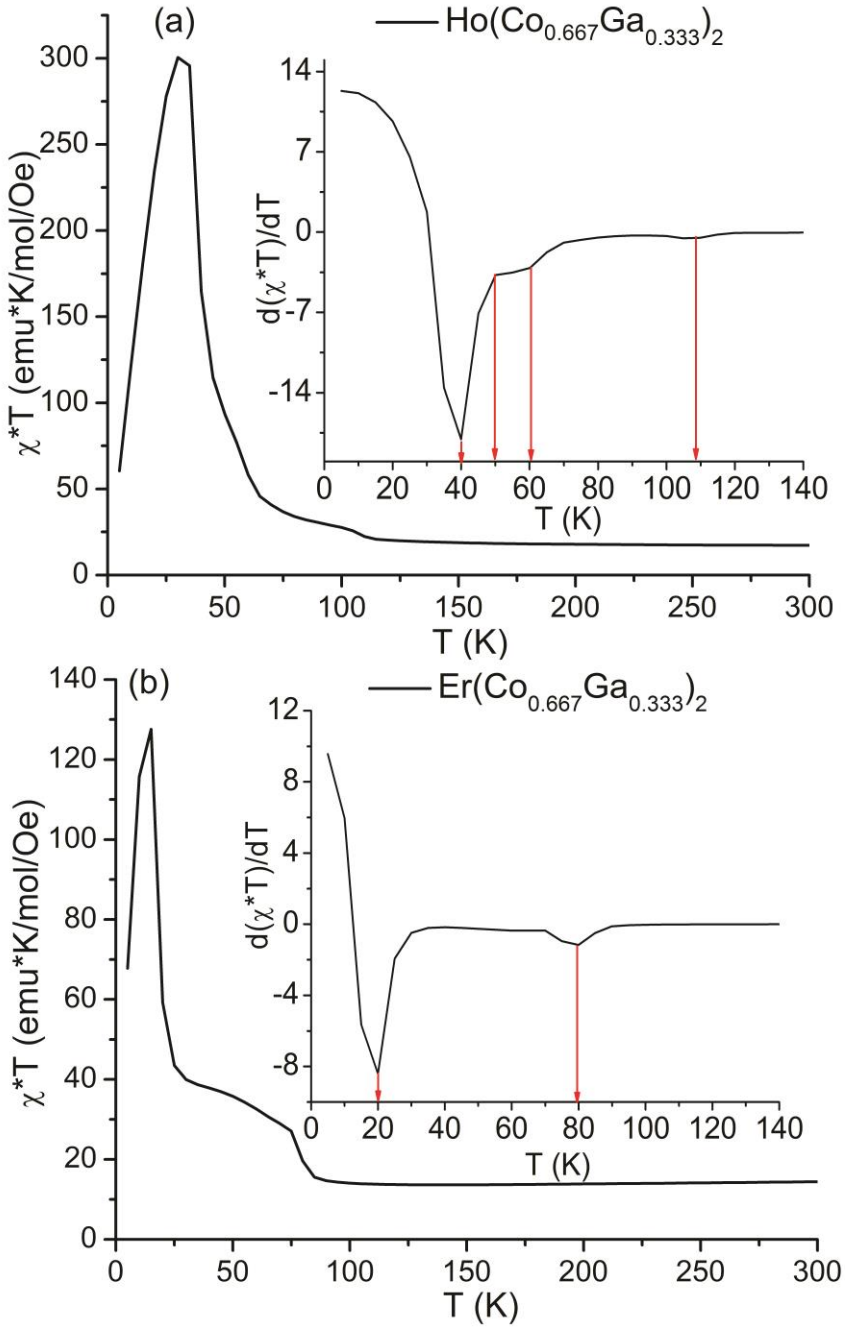

Figure 4.4. (a) A plot of χ*T vs T for $Ho(Co_{.667}Ga_{.333})_2$ and the associated first derivative (inset) showing the possibility of magnetic phase transitions due to undetected (by diffraction) magnetic phases. **(b)** A corresponding plot for $Er(Co_{.667}Ga_{.333})_2$.

Although no impurity phases were detected by X-ray powder diffraction, except for Tb, it is possible that the magnetic behavior between the T_t and beginning of Curie-Weiss regime is dominated by such magnetic impurities. Such possibility is confirmed in $RE(Co_{0.667}Ga_{0.333})_2$ (*RE* = Ho and Er): both χ^*T and its derivatives versus *T* indicate the presence of subtle magnetic transitions (**Figure 4.4 (a) and (b)**).

Table 4.4. Magnetic transition temperature (T_t), calculated Weiss temperatures (θ_p), theoretical magnetic moment of *RE* ions (M_{RE}^{3+}), effective magnetic moments per formula unit (μ_{eff}), g_JJ, and saturation magnetization per formula unit (M_s) for annealed $RE(Co_{0.667}Ga_{0.333})_2$ (*RE* = Gd, Tb, Dy, Ho, and Er).

Composition	T_t(K)	θ_p(K)	M_{RE}^{3+}(μ_B/ion)	μ_{eff}(μ_B/f.u.)	g_JJ	M_s(μ_B/f.u.)
$Gd(Co_{0.667}Ga_{0.333})_2$	150	156.95	7.94	8.01	7	6.52
$Tb(Co_{0.667}Ga_{0.333})_2$	95	119.09	9.72	8.74	9	7.53
$Dy(Co_{0.667}Ga_{0.333})_2$	55	56.83	10.63	10.57	10	6.54
$Ho(Co_{0.667}Ga_{0.333})_2$	36	24.05	10.60	11.23	10	8.10
$Er(Co_{0.667}Ga_{0.333})_2$	15	-9.82	9.59	10.84	9	6.90

Returning to **Table 4.4**, the free ion effective magnetic moments of Gd^{3+} and Dy^{3+} are 7.94 and 10.63 μ_B, respectively. Magnetic moments derived for $Gd(Co_{0.667}Ga_{0.333})_2$ and $Dy(Co_{0.667}Ga_{0.333})_2$ are close to those values, indicating no paramagnetic Co contributions above T_t. The free ion values of the Ho^{3+} and Er^{3+} magnetic moments are 10.60, and 9.59 μ_B, respectively, and the experimental moments for $Ho(Co_{0.667}Ga_{0.333})_2$ and $Er(Co_{0.667}Ga_{0.333})_2$ are significantly higher, suggesting the possibility of some Co contribution. As mentioned, the case of Tb is difficult due to obvious contamination by

the detected impurity phase. However, Tb is between Gd and Dy in the periodic table, therefore, Co atoms may not carry magnetic moments in $Tb(Co_{0.667}Ga_{0.333})_2$ above T_t.

To clarify the magnetic ground state below T_t, we measured the isothermal magnetizations at 5K. **Figure 4.5** reveals that the magnetization is saturated in $Gd(Co_{0.667}Ga_{0.333})_2$, confirming the ferromagnetic transition, although the value is slightly below the expected 7 μ_B. On the other hand, the other four are not completely saturated even at 50 kOe and 5K and it is difficult to extract a saturation moment. As the data were taken at 5K, the rare-earth moment may be significantly reduced from the free ion value due to crystal field effects. It is, thus, impossible to deduce if an ordered moment on Co exists at this temperature, nor is it possible to determine if the ground state is that of a simple ferromagnet with only a rare-earth moment or that of a ferrimagnet with an anti-parallel Co moment.

As discussed before, ferrimagnetic interactions in $RE(Co_{0.667}Ga_{0.333})_2$ (*RE* = Ho and Er) are very possible. Ordered Co moments of 1 μ_B have been reported for $HoCo_2$ and $ErCo_2$.[111,112] However, according to the magnetic behavior of RET_2-$REAl_2$,[101] there will be some transfer of additional electrons to Co in $RE(Co_{0.667}Ga_{0.333})_2$. Therefore, the magnetic moment of Co should be less than $1\mu_B$/Co in the Ga substituted materials studied here. Thus, it is possible that in the case of $RE(Co_{0.667}Ga_{0.333})_2$ (*RE* = Ho, and Er), antiferromagnetic coupling between the *RE* and Co sublattices and the crystal field effects may both be at play. Neutron diffraction studies are planned in order to better investigate this hypothesis.

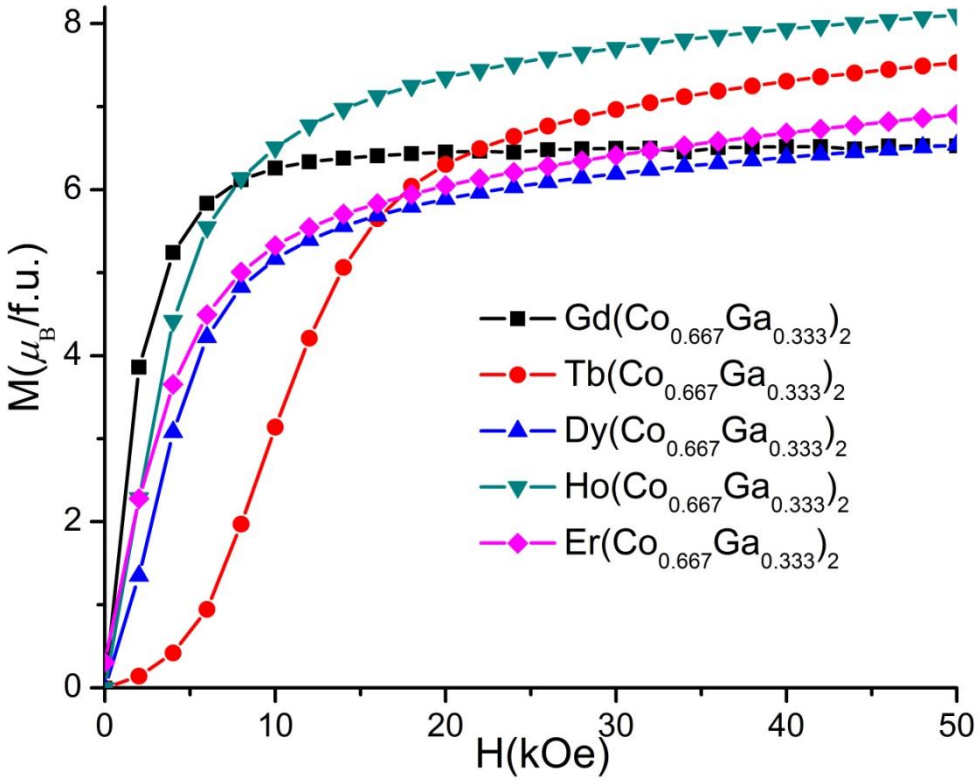

Figure 4.5. Magnetization vs. magnetic field plots of *RE*$(Co_{0.667}Ga_{0.333})_2$ (*RE* = Gd, Tb, Dy, Ho, and Er) at 50 kOe and 5K.

4.3.3 Magnetocaloric Effect of $Gd(Co_{0.667}Ga_{0.333})_2$

The magnetocaloric effect (MCE) of $Gd(Co_{0.667}Ga_{0.333})_2$ was evaluated from the isothermal magnetization vs. field (*M* vs. *H*) measurements (**Figure 4.6 (a) and (b)**). The magnetocaloric effect in terms of the isothermal magnetic entropy change, ΔS_{mag}, can be derived from the Maxwell relations:

$$\left(\Delta S_{mag}\right)_T = \int_{H_i}^{H_f} \left(\frac{\partial M}{\partial T}\right)_H \mathrm{d}H \qquad (4.1)$$

where H_i and H_f are the initial and final magnetic fields, respectively.

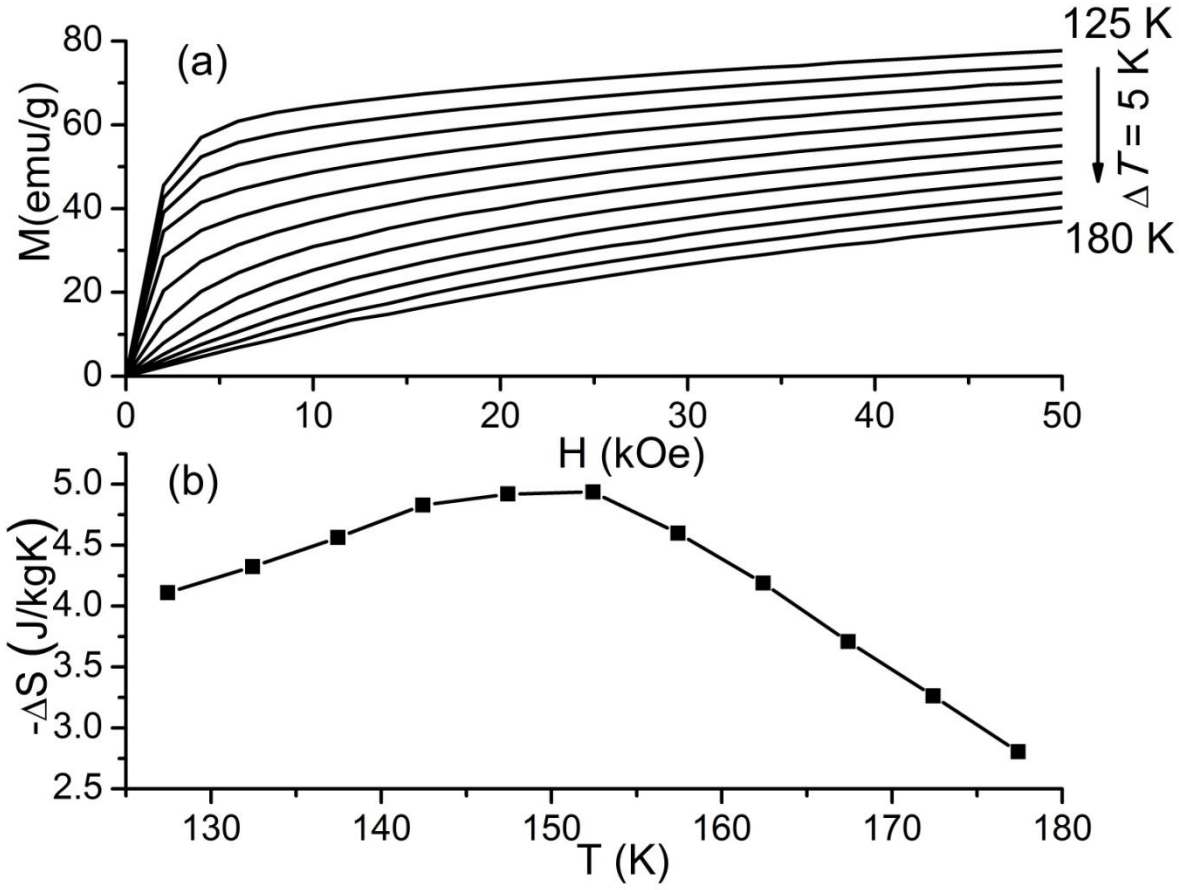

Figure 4.6. (a) Magnetization vs. magnetic field plots. **(b)** magnetic entropy changes as a function of temperature for the annealed $Gd(Co_{0.667}Ga_{0.333})_2$.

In practice, a numerical integration is performed using the following formula

$$(\Delta S_{mag})_{\frac{T_1+T_2}{2}} = \sum_i \frac{M(T_2)_i - M(T_1)_i}{T_2 - T_1}\Delta H \qquad (4.2)$$

where ΔH is a magnetic field step and $M(T_2)_i$ and $M(T_1)_i$ are the values of magnetization at temperatures T_2 and T_1, respectively. The magnetic entropy change, ΔS_{mag}, for ΔH = 0-50 kOe is plotted in **Figure 4.6 (b)**. As expected, ΔS_{mag} peaks around the Curie temperatures and has the maximum value of -4.94 J/(kgK) for $Gd(Co_{0.667}Ga_{0.333})_2$. A

relatively small ΔS_{mag} value of -4.94 J/(kgK) indicates the presence of a conventional magnetocaloric effect (MCE), i.e. without a first-order coupled magneto-structural transition.

4.4 Conclusions

A peritectic reaction between cubic Laves phase and Ga-rich liquid appears necessary to form pure $MgZn_2$-type *RE*$(Co_{0.667}Ga_{0.333})_2$ (*RE* = Gd, Tb, Dy, Ho, and Er) phases. Co and Ga atoms occupy the 2*a* and 6*h* sites, however, their Co/Ga ratio on the two sites could not be refined due to their similar atomic scattering powers. Magnetic analyses suggest that *RE*$(Co_{0.667}Ga_{0.333})_2$ (*RE* = Gd, Tb and Dy) are apparently ferromagnetic while the other two phases are likely to be ferrimagnetic. Plots of χ**T* and its derivatives versus *T* show the presence of subtle magnetic transitions, which indicates some impurities beyond detecting limit of X-ray diffraction. Plots of χ^{-1} versus *T* suggest the possibility of some Co contribution in *RE*$(Co_{0.667}Ga_{0.333})_2$ (*RE* = Ho, and Er) above the transition temperature. At low temperatures, crystal field effects on the RE^{3+} cations and/or antiparallel coupling between the *RE* and Co magnetic sublattices can contribute to the smaller than expected saturation magnetization. The MCE was studied for the ferromagnetic Gd$(Co_{0.667}Ga_{0.333})_2$, and the magnetic entropy change reaches the maximum value of -4.94 J/(kgK) around its Curie temperature. Although the magnetic entropy value implies presence of a conventional MCE, the current work highlights possibilities to obtain new $MgZn_2$-type Laves phases and magnetocaloric materials.

Neutron diffraction studies are planned in order to clarify the Co/Ga occupancy and establish the magnetic ground state of $RE(Co_{0.667}Ga_{0.333})_2$ (*RE* = Ho, and Er).

Chapter 5. Studies on Structural Transformations and Magnetic Properties of Pseudobinary $GdCo_2$-$GdGa_2$ System

This chapter contains the material covered in the manuscript "Studies on Structural Transformations and Magnetic Properties of Pseudobinary $GdCo_2$-$GdGa_2$ system", which is currently unpublished, but will be submitted to a peer reviewed scientific journal. The experimental procedures, structure determinations, data interpretations, and writing of the manuscript were completed by the candidate. Electronic structure calculations were performed in collaboration with Dr. Asa Toombs and Dr. Gordon J Miller.

Pseudobinary $Gd(Co_{1-x}Ga_x)_2$ (x = 0, 1/6, 1/3, 1/2, 2/3, 5/6, and 1) phases were synthesized by arc melting of the constituent elements and subsequent annealing. The samples were characterized by powder and single crystal X-ray diffraction, magnetic measurements, and electronic structure calculations. An interesting structural sequence was obtained: cubic $MgCu_2$-type structure for x = 0 and 1/6; $MgCu_2$-type structure for x = 1/3; orthorhombic MgSrSi-type structure x = 1/2, orthorhombic $CeCu_2$-type structure for x = 2/3; hexagonal AlB_2-type structure for x = 5/6 and 1. The two samples with the orthorhombic structures display similar behavior. Firstly, both of them contain more than one phase according to the X-ray diffraction or magnetic measurements. In addition, they both exhibit a sharp magnetic transition at 55K. The $GdGa_2$ (x = 1) phase is antiferromagnetic, while the other ones are ferrimagnetic or ferromagnetic. Curie temperature of $Gd(Co_{1-x}Ga_x)_2$ decreases with the increasing Ga content. Tight-binding linear-muffin-tin orbital (TB-LMTO) calculations were performed on $GdCo_2$, GdCoGa, and $GdGa_2$ to investigate their structural transformations, which appear to be driven by the changes in the valence electron count (VEC).

5.1 Introduction

The environmental awareness, which matured in the past few decades, increased our efforts towards development of energy-efficient and environment-friendly refrigeration techniques. Discovery of giant magnetocaloric effect (GMCE) in $Gd_5Si_2Ge_2$ showed that magnetic refrigeration can be a potential alternative to the conventional vapor-cycle refrigeration.[12] In the case of GMCE, there is a first-order magnetic

transition; the total entropy change, which is discontinuous at the transition points, contains both the structural and magnetic entropy contributions, and thus is significantly enhanced when compared to a conventional MCE. In this light, materials with a GMCE are good candidates for magnetic refrigeration. Laves phases with a general formula *RE*Co_2 (*RE* = rare earth) adopt a cubic $MgCu_2$-type structure,[113] but exhibit different magnetic properties depending on *RE* due to the inherent instability of Co sublattice magnetism. For *RE* = Dy, Ho, and Er, a nonmagnetic Co sublattice is turned into ferromagnetic by the *RE* molecular field upon cooling, i.e. a metamagnetic transition is induced by the itinerant electrons.[56] Due to the itinerant electron metamagnetic (IEM) transition, *RE*Co_2 (*RE* = Dy, Ho, and Er) show a first-order magnetic transition and GMCE.[54,55] On the other hand, a conventional MCE with a second-order magnetic transition is observed in other *RE*Co_2 compounds.

Magnetocaloric materials with transitions around room temperature are the most promising candidates in terms of wide-spread applications and economic benefits. However, most of *RE*Co_2 compounds have transitions at lower temperatures. Curie temperature (T_C) of *RE*Co_2 peaks at 400K for *RE* = Gd and drops rapidly when *RE* moves away from Gd on both sides.[56] Replacing Co with some nonmagnetic elements in $GdCo_2$ may allow adjusting the T_C to room temperature. In this work, nonmagnetic Ga was chosen to substitute for Co. Previously, a few structures have been reported in the $Gd(Co_{1-x}Ga_x)_2$ system: 1) cubic $MgCu_2$-type $GdCo_2$ ($Fd\bar{3}m$);[63] 2) orthorhombic MgSrSi-type GdCoGa (*Pnma*);[61] 3) orthorhombic $CeCu_2$-type $GdCo_{0.67}Ga_{1.33}$ (*Imma*);[62] and 4) hexagonal AlB_2-type $GdGa_2$ (*P*6/*mmm*).[114] To explore this system in greater detail,

$Gd_3Co_{6-x}Ga_x$ (x = 0, 1, 2, 3, 4, 5, and 6) alloys were prepared in this work. The composition of the starting materials is divided by 3 to resemble the general AB_2 formula, i.e. $Gd(Co_{1-x}Ga_x)_2$ (x = 0, 1/6, 1/3, 1/2, 2/3, 5/6, and 1).

Structural transitions can be driven by changes in the valence electron count (VEC) and/or geometric parameters. In the case of the $Gd(Co_{1-x}Ga_x)_2$ system, Ga has an atomic size similar to that of Co (r_{Co} = 1.25 Å, r_{Ga} = 1.26 Å),[109] which minimizes the geometric effects. Therefore, the VEC must be a key factor in controlling the $Gd(Co_{1-x}Ga_x)_2$ structures. In it worth mentioning that the structural transformation in the $GdCo_2$-$GdAl_2$ system were rationalized in terms of the VEC and Fermi surface features.[101] Since Ga and Al are isovalent and have similar atomic sizes (r_{Al} = 1.25 Å),[109] some of the general rules developed for the $GdCo_2$-$GdAl_2$ system may be applicable to the $GdCo_2$-$GdGa_2$ system.

5.2 Experimental Section

5.2.1 Synthesis

The starting materials are Gd (99.99 wt.%, distilled grade, Metall Rare-earth Limited, China), Co (99.98 wt.%, Alfa Aesar) and Ga (99.999 wt.%, Alfa Aesar) pieces. Alloys with the $Gd(Co_{1-x}Ga_x)_2$ (x = 0, 1/6, 1/3, 1/2, 2/3, 5/6, and 1) stoichiometries and a total mass of ~1 g were arc-melted 3 times to ensure homogeneity. During remelting process, the samples were turned over as fast as possible to prevent sample cracking during cooling. The cast alloy buttons were split, and then one-half of each button was

wrapped in Ta foil, sealed in evacuated silica tubes, heated to 850°C at 100°C/hour, annealed at this temperature for 7 days and subsequently quenched in cold water.

5.2.2 X-ray Analysis

Room-temperature phase analyses of the cast and annealed $Gd(Co_{1-x}Ga_{x)2}$ (x = 0, 1/6, 1/3, 1/2, 2/3, 5/6, and 1) samples were performed on a PANalytical X'Pert Pro diffractometer with a linear X'Celerator detector. The X-ray diffraction patterns were collected with Co$K\alpha$ radiation to eliminate the Gd fluorescene associated with Cu$K\alpha$ radiation. More than one crystalline phase was observed in most of the cast $Gd(Co_{1-x}Ga_{x)2}$ (x = 0, 1/6, 1/3, 1/2, 2/3, 5/6, and 1) alloys. However, pure samples could be obtained by annealing at 850°C for 7 days except for GdCoGa (x = 1/2). The annealed alloys with x = 0 and 1/6 yielded a cubic $Fd\bar{3}m$ phase. X-ray powder diffraction of the sample with x = 1/3 suggested a hexagonal $P6_3/mmc$ phase. The GdCoGa alloy contained an orthorhombic *Pnma* phase as the main phase and some unidentified peaks. The annealed alloy with x = 2/3 adopted an orthorhombic *Imma* structure. A hexagonal phase ($P6/mmm$) was formed in the annealed alloys with x = 5/6 and 1. The unit cell dimensions derived from the Rietveld refinement (Rietica program)[68] for the annealed samples are summarized in **Table 5.1**.

Table 5.1. Phase analyses from the Reitveld refinement of X-ray powder diffraction for annealed $Gd(Co_{1-x}Ga_x)_2$ (x = 0, 1/6, 1/3, 1/2, 2/3, 5/6, and 1).

$Gd(Co_{1-x}Ga_x)_2$	structure	space group	a, Å	b, Å	c, Å	V, Å^3
x = 0	$MgCu_2$-type	$Fd\bar{3}m$	7.25618(2)	7.25618(2)	7.25618(2)	382.054(2)
x = 1/6	$MgCu_2$-type	$Fd\bar{3}m$	7.33059(3)	7.33059(3)	7.33059(3)	393.928(3)
x = 1/3	$MgZn_2$-type	$P6_3/mmc$	5.26670(3)	5.26670(3)	8.50070(8)	204.203(3)
x = 1/2	MgSrSi-type + impurities	$Pnma$	7.0001(7)	4.4330(4)	7.1509(7)	221.90(4)
x = 2/3	$CeCu_2$-type	$Imma$	4.3684(1)	7.0967(2)	7.4914(2)	232.24(1)
x = 5/6	AlB_2-type	$P6/mmm$	4.37694(7)	4.37694(7)	3.65559(9)	60.650(2)
x = 1	AlB_2-type	$P6/mmm$	4.22011(6)	4.22011(6)	4.13423(9)	63.764(2)

Suitable single crystals were extracted from the annealed $Gd(Co_{1-x}Ga_{x)2}$ (x = 0, 1/3, 1/2, 2/3, 5/6, and 1) alloys. However, no suitable single crystals were picked up for x = 1/6. Single crystal X-ray diffraction data were collected on a STOE IPDS II diffractometer with Mo$K\alpha$ radiation at room temperature. Numerical absorption corrections were based on the crystal shapes that were originally derived from optical face indexing but later optimized against equivalent reflections using the STOE X-shape software. Crystal structures were refined using the SHELXL program.[67] Crystallographic data and refinement results are summarized in **Table 5.2 and 5.3.** The structures obtained from single crystal solutions agree well with the powder X-ray diffraction results.

Table 5.2. Crystallographic data and refinement results for the annealed $Gd(Co_{1-x}Ga_{x)2}$ phases. (MoK_α radiation, 293K)

$Gd(Co_{1-x}Ga_{x)2}$	x = 0	x = 1/3	x = 1/2	x = 2/3	x = 5/6	x = 1
Structure type	$MgCu_2$-type	$MgZn_2$-type	MgSrSi-type	$CeCu_2$-type	AlB_2-type	AlB_2-type
Space group	$Fd\bar{3}m$	$P6_3/mmc$	$Pnma$	$Imma$	$P6/mmm$	$P6/mmm$
Scan mode			Omega			
***a* (Å)**	7.2518(8)	5.2593(7)	7.111(1)	4.3649(9)	4.3719(6)	4.2143(6)
***b* (Å)**			4.3887(9)	7.090(1)		
***c* (Å)**		8.490(2)	7.340(2)	7.482(2)	3.6441(7)	4.1319(8)
Volume (Å^3)	381.36(7)	203.37(6)	229.05(8)	231.54(8)	60.32(2)	63.55(2)
ρ_{calc} (g/cm^3)	9.583	9.221	8.291	8.304	8.070	7.752
Z	8	4	4	4	1	1
Index ranges	$-9 \le h \le 9$ $-9 \le k \le 8$ $-9 \le l \le 9$	$-7 \le h \le 7$ $-7 \le k \le 7$ $-11 \le l \le 11$	$-9 \le h \le 9$ $-4 \le k \le 5$ $-10 \le l \le 10$	$-5 \le h \le 5$ $-8 \le k \le 9$ $-10 \le l \le 10$	$-5 \le h \le 5$ $-5 \le k \le 5$ $-4 \le l \le 4$	$-6 \le h \le 5$ $-6 \le k \le 6$ $-6 \le l \le 6$
2θ range (°)	9.74 to 57.38	8.94 to 58.18	8.00 to 58.50	7.92 to 58.08	10.78 to 57.52	9.88 to 57.62
Meas. Refl.	963	2053	2302	1255	629	1127
Ind. Refl.	36 (R_{int} = 0.0819	129 (R_{int} = 0.0824)	345 (R_{int} = 0.0715)	189 (R_{int} = 0.0669)	49 (R_{int} = 0.0722)	77 (R_{int} = 0.0485)
Extinction coefficient	0.0003(2)	0.016(1)	0.0015(9)	0.0050(7)	0.05(2)	0.062(2)
Largest peak / hole (e/Å^3)	0.452/-1.259	1.158/-1.071	6.159 /-6.778	1.479/-1.888	1.327 /-1.403	0.738/-0.785
Goodness-of-fit on $\|F^2\|$	1.384	1.199	1.110	1.191	1.529	0.591
R indices [I > 2σ(I)]	R_1 = 0.0238 wR_2 = 0.0237	R_1 = 0.0252 wR_2=0.0292	R_1 = 0.0574 wR_2 = 0.1079	R_1 = 0.0244 wR_2 = 0.0482	R_1 = 0.0293 wR_2 = 0.0727	R_1 = 0.0111 wR_2 = 0.0581
R indices [all data]	R_1 = 0.0238 wR_2 = 0.0237	R_1 = 0.0402 wR_2=0.0310	R_1 = 0.0857 wR_2 = 0.1254	R_1 = 0.0316 wR_2 = 0.0511	R_1 = 0.0293 wR_2 = 0.0727	R_1 = 0.0120 wR_2 = 0.0603

Table 5.3. Atomic coordinates and isotropic temperature parameters (U_{eq}) for $Gd(Co_{1-x}Ga_x)_2$ (x = 0, 1/3, 1/2, 2/3, 5/6, 1).

Atom	Site (point symmetry)	Occupancy	x/*a*	y/*b*	z/*c*	U_{eq} (Å^2)
		$GdCo_2$ (x = 0)				
Gd1	8*a*($\bar{4}$3*m*)	1	1/8	1/8	1/8	0.012(1)
Co1	16*d*($\bar{3}$*m*)	1	0	1/2	0	0.012(1)
		$GdCo_{1.33}Ga_{0.67}$ (x = 1/3)				
Gd1	4*f*(3*m*)	1	1/3	2/3	0.0617(1)	0.009(1)
Co1/Ga11	2*a*($\bar{3}$*m*)	0.67/0.33*	0	0	0	0.003(1)
Co2/Ga22	6*h*(*mm*)	0.67/0.33*	0.8326(2)	0.6652(5)	1/4	0.009(1)
		GdCoGa (x = 1/2)				
Gd1	4*c*(*m*)	1	0.0103(2)	1/4	0.7969(2)	0.016(1)
Co1	4*c*(*m*)	1	0.3219(6)	1/4	0.0783(6)	0.020(1)
Ga1	4*c*(*m*)	1	0.1981(4)	1/4	0.4086(5)	0.018(1)
		$GdCo_{0.67}Ga_{1.33}$ (x = 2/3)				
Gd1	4*e*(*mm*)	1	0	3/4	0.4541(1)	0.015(1)
Co1/Ga11	8*h*(*m*)	0.33/0.67*	0	0.4443(2)	0.1648(1)	0.019(1)
		$GdCo_{0.33}Ga_{1.67}$ (x = 5/6)				
Gd1	1*a*(6/*mmm*)	1	0	0	0	0.018(2)
Co1/Ga11	2*d*($\bar{6}$*m*2)	0.17/0.83*	1/3	2/3	1/2	0.036(2)
		$GdGa_2$ (x = 1)				
Gd1	1*a*(6/*mmm*)	1	0	0	0	0.008(1)
Ga1	2*d*($\bar{6}$*m*2)	1	1/3	2/3	1/2	0.012(1)

*Co/Ga occupancy was not refined

5.2.3 Magnetometry

Temperature-dependent magnetization was measured in a 100 Oe field from 300 (or 350K) to 5K, or 550 to 300K, in a field-cooled (FC) mode using a Superconducting Quantum Interference Device (SQUID) on the Magnetic Property Measurement System (MPMS). The maxima in the derivatives of the magnetization with respect to temperature were taken as Curie (T_C) temperatures. Temperatures of the cusps on the temperature-dependent magnetizations were treated as Neel temperatures (T_N).

5.2.4 Electronic Structure Calculations

Electronic structure calculations were performed using the Stuttgart Tight-Binding, Linear-Muffin-Tin Orbital program with Atomic Sphere approximation (TB-LMTO-ASA).[115] The atomic sphere approximation uses overlapping Wigner-Seitz (WS) spheres to fill space. The symmetry of potential is considered spherical in each WS sphere and a combined correction is used to account for the overlapped spheres. The maximum allowed overlap between the WS spheres was 20% and no empty spheres were necessary for any of the calculations. The electron exchange and correlation were treated with the von Barth-Hedin local-density approximation (LDA)[71] and the local spin-density approximation (LSDA).[72] All relativistic effects except spin-orbit coupling were taken into account using a scalar relativistic approximation.[116] The basis sets included Gd (6*s*, 6*p*, 5*d*), Co (4*s*, 4*p*, 3*d*), and Ga (4*s*, 4*p*). The Gd 4*f* wavefunctions were considered as pseudo-core orbitals with 7 electrons, and were not included into the electronic density of states and crystal orbital Hamilton population analyses.[117] Structure optimization

calculations were performed using the Vienna Ab initio Simulation Package (VASP).[118,119] The VASP uses projector augmented-wave (PAW) pseudopotentials that were adopted with the Perdew-Burke-Ernzerhof generalized gradient approximation (PBE-GGA).

5.3 Results and Discussions

5.3.1 Structural Features and Transformation

X-ray diffraction results can summarized as follows: i) five structures are present in the $Gd(Co_{1-x}Ga_x)_2$ (x = 0, 1/6, 1/3, 1/2, 2/3, 5/6, and 1) system, suggesting a relationship between the Co/Ga ratio and structure (**Figure 5.1**); ii) impurities in the cast samples decrease as the Ga content is higher (x = 2/3, 5/6, and 1); iii) all samples become phase pure after the heat treatment except for GdCoGa.

Both annealed $GdCo_2$ (x = 0) and $GdCo_{1.67}Ga_{0.33}$ (x = 1/6) adopt the cubic $MgCu_2$-type structure. Diffraction peaks on the powder XRD pattern of $GdCo_{1.667}Ga_{0.333}$ shifted to lower scattering angles compared with that of $GdCo_2$, suggesting an increase in the unit cell parameters of $GdCo_{1.67}Ga_{0.33}$. (**Table 5.1**) This is expected because the atomic size of Ga is slightly larger than that of Co. Single crystal analysis was performed for $GdCo_2$, whereas no suitable single crystals of $GdCo_{1.67}Ga_{0.33}$ were found. Indexing of the Bragg peaks for $GdCo_2$ indicated a cubic lattice, isostructural with the Laves $MgCu_2$-type one. There are two independent crystallographic sites in the unit cell: Gd atoms occupy the 8*a* site while Co atoms are on the 16*d* site. For $GdCo_{1.67}Ga_{0.33,}$ Gd atoms are still on the 8*a*

site, while Ga atoms will share the 16*d* site with Co. Each Co atom has six nearest Co neighbours, which form two tetrahedra with one common Co atom.

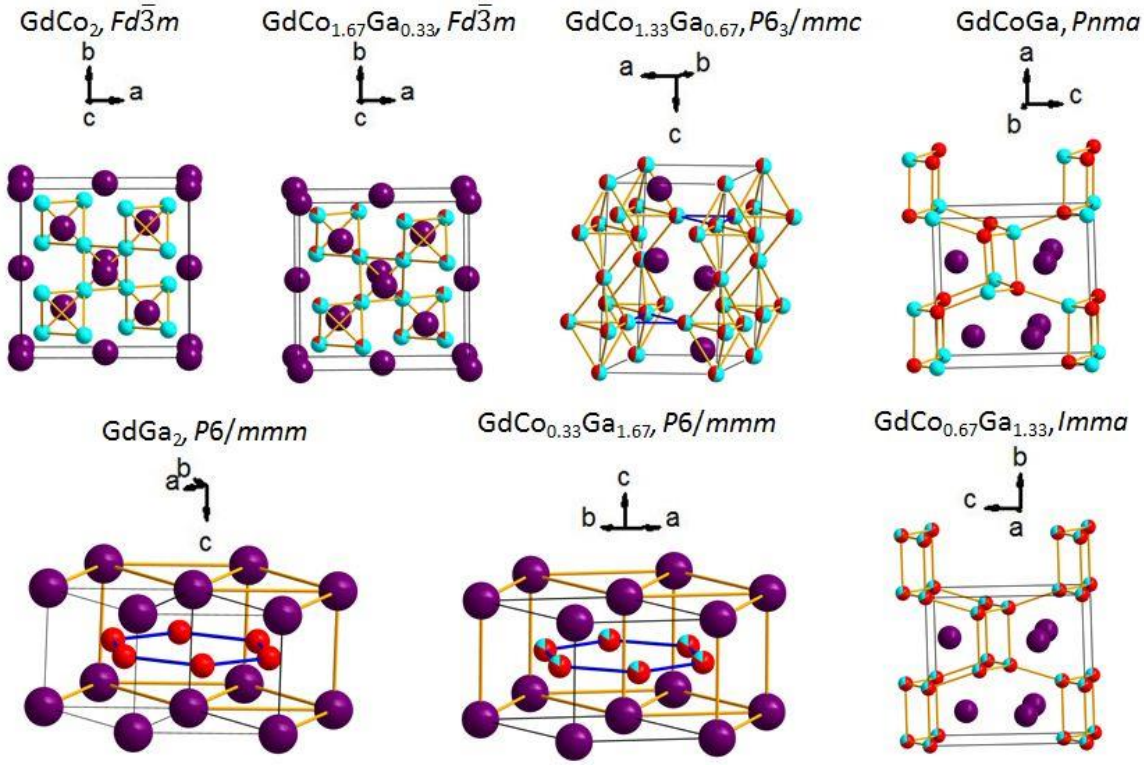

Figure 5.1. Crystal structures of Gd($Co_{1-x}Ga_{x)2}$ (x = 0, 1/6, 1/3, 1/2, 2/3, 5/6, and 1). Larger purple atoms denote Gd, teal atoms are Co, and red atoms represent Ga.

Annealed $GdCo_{1.33}Ga_{0.67}$ (x = 1/3) adopts a hexagonal $MgZn_2$-type structure, which has three crystallographic sites: 2*a*, 4*f* and 6*h*. Gd atoms fully occupy the 4*f* site, while Co and Ga are on the 2*a* and/or 6*h* site. However, the Co/Ga occupancy could not be refined due to their similar scattering factors. A statistical Co/Ga distribution with the 0.67/0.33 ratio was assumed both on the 2*a* and 6*h* sites.

GdCoGa (x = 1/2) and $GdCo_{0.67}Ga_{1.33}$ (x = 2/3) adopt orthorhombic structures with the *Pnma* and *Imma* space groups, respectively. As seen in **Figure 5.1**, the orthorhombic structures are very similar; in fact the GdCoGa structure is an ordered variant of the $GdCo_{0.67}Ga_{1.33}$ one. There are three 4*c* sites, occupied separately by Gd, Co, and Ga, in the orthorhombic GdCoGa phase. There are two crystallographic sites in the orthorhombic $GdCo_{0.67}Ga_{1.33}$ phase: Gd atoms occupy the 4*e* site, and Co and Ga atoms share the 8*h* site. It is worth mentioning that it was more difficult to obtain a pure GdCoGa phase then a pure $GdCo_{0.67}Ga_{1.33}$ phase. An impurity in GdCoGa could not be eliminated even after annealing at 850°C for 1 week.

$GdCo_{0.33}Ga_{1.67}$ (x = 5/6) and $GdGa_2$ (x = 1) adopt the hexagonal AlB_2-type structure. There are two crystallographic sites in the structure: Gd atoms fully occupy the 1*a* site whereas Co and Ga atoms are on the 2*d* site. Increased lattice parameters were observed for $GdGa_2$, which is due to the larger atomic size of Ga. In addition, the *a*/*c* ratio for $GdCo_{0.33}Ga_{1.67}$ and $GdGa_2$ is 1.20 and, 1.02, respectively. Gd atoms form two triangular prisms in one unit cell, and Co or Ga atoms are located in the center of these triangular prisms.

As the Ga content increases, the structures change from a "condensed cluster-based" → "3D Network" → "2D Network". The cubic Laves phase has the Co atoms in vertex-sharing tetrahedral clusters. In the hexagonal Laves phase, the Co tetrahedra are still present, but now they are stacked along the *c* axis via alternating vertex- and face-sharing motifs. On moving to GdCoGa and $GdCo_{0.67}Ga_{1.33}$, the tetrahedral clusters are lost, but the Co and Ga atoms sit in distorted tetrahedral coordination environments.

These structures have extended networks of 6- and 8-membered rings along with ladders of 4-membered rings. By increasing the Ga content even more, the 3D network is converted into the 2D network of the graphene-like sheets of Ga. Coordination numbers (CN) of Co/Ga also change for the different types of networks. In the cubic Laves phases, Co/Ga has a CN of 6, then changes to the CN of 4 in the 3D network, and finally to a CN of 3 in the 2D network. Electronic structure calculations were employed to gain some insights about the structural transformations of the $Gd(Co_{1-x}Ga_x)_2$ system.

5.3.2 Magnetic Properties

Temperature-dependent magnetization of $Gd(Co_{1-x}Ga_x)_2$ (x = 0, 1/6, 1/3, 1/2, 2/3, 5/6, and 1) was measured.(**Figure 5.2**) For the Co-free phase, i.e. $GdGa_2$, the magnetic transition becomes antiferromagnetic, with a Neel temperature of 20K, in accordance with the previous reported results.[120] For other samples, T_C decreases with the increasing Ga content, which indicates that Ga substitution weakens the magnetic interactions controlled via the RKKY[2,1,3] mechanism. GdCoGa and $GdCo_{0.67}Ga_{1.33}$ resemble each other with respect to magnetic trnasition: both of them has a sharp magnetic transition at ~55K, but the former has a second transition at 148K, while the latter at 204K. The apperance of two magnetic transitions indicate presence of impurities in the two samples. Magnetic transitions of $Gd(Co_{1-x}Ga_x)_2$ (x = 0, 1/6, 1/3, 1/2, and 2/3) are very sharp at T_C, suggesting that these samples may have interesting magnetocaloric properties.

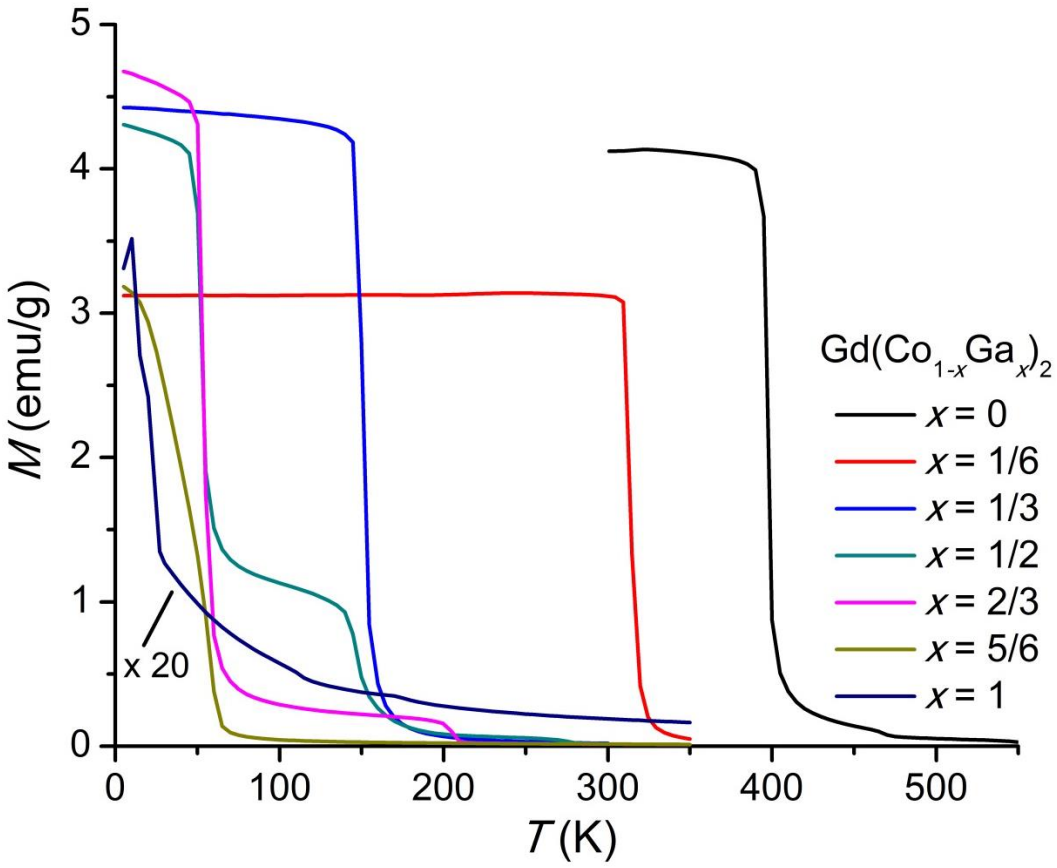

Figure 5.2. Temperature dependence of magnetization for $Gd(Co_{1-x}Ga_x)_2$ (x = 0, 1/6, 1/3, 1/2, 2/3, 5/6, and 1) under a magnetic field of 100 Oe. Magnetization for x = 1 is magnified by 20.

5.3.3 Electronic Structure

Based on the phase analysis, even small changes in x of 1/6 yield new structures. To trace the origin of the structural transformations, we performed electronic structure calculations on $GdCo_2$ and $GdGa_2$, which seem to be ripe for substitution. Additionally, we analyzed the electronic structure of ordered GdCoGa. GdCoGa is structurally similar

to $GdCo_{0.67}Ga_{1.33}$, but displays full ordering of the Co and Ga atoms. **Table 5.4** summarizes the corresponding valence electron counts (VEC).

Table 5.4. Valence electron counts (VEC) of $Gd(Co_{1-x}Ga_x)_2$ (x = 0, 1/6, 1/3, 1/2, 2/3, 5/6, 1) samples.

Samples	x value	VEC formula	VEC, e^-/f.u.
$GdCo_2$	0	(1×3)+(2×9)	21
$GdCo_{1.67}Ga_{0.33}$	1/6	(1×3)+(1.67×9)+(0.33×13)	22.32
$GdCo_{1.33}Ga_{0.67}$	1/3	(1×3)+(1.33×9)+(0.67×13)	23.68
GdCoGa	1/2	(1×3)+(1×9)+(1×13)	25
$GdCo_{0.67}Ga_{1.33}$	2/3	(1×3)+(0.67×9)+(1.33×13)	26.32
$GdCo_{0.33}Ga_{1.67}$	5/6	(1×3)-(0.33×1)+(1.67×3)	7.68 (27.68)*
$GdGa_2$	1	(1×3)+(2×3)	9 (29)*

*The VEC of 27.78 and 29 e^-/f.u. is obtained by assuming 9 electrons for Co and 13 electrons for Ga (3 valence electrons + 10 localized *d* electrons).

5.3.3.1 Electronic Structure of $MgCu_2$-type $GdCo_2$ and $GdCo_{1.67}Ga_{0.33}$

$GdCo_2$ crystallizes with the $MgCu_2$-type Laves structure. Density of states (DOS) using both the local density approximation (LDA) and the local spin density approximation (LSDA) were calculated.(**Figure 5.3**) Total energy, magnetic moment, and structural optimization calculations were performed using the VASP. Including the spin-polarization into the calculation is important; without the spin-polarization the VASP optimization produces a unit cell that is significantly smaller than the experimentally determined unit cell, while with spin-polarization the VASP optimization yields lattice parameters and bond lengths that are close to the experimental ones. (**Table 5.5)** Therefore, the COHP was calculated using the LSDA approach. Previous experimental

and theoretical studies, performed on the GdX_2 (X = Fe, Co, and Ni) compounds, showed that the Gd atoms are ferromagnetic coupled[121–123], and the same behavior was assume in our calculations. The magnetic moment on Gd in $GdCo_2$ calculated by the VASP was 6.755. It compares favorably to 6.878, obtained by B. Zegaou, et al. using all-electron full-potential linear muffin-tin orbital method (FP-LMTO) with CGA.[121]

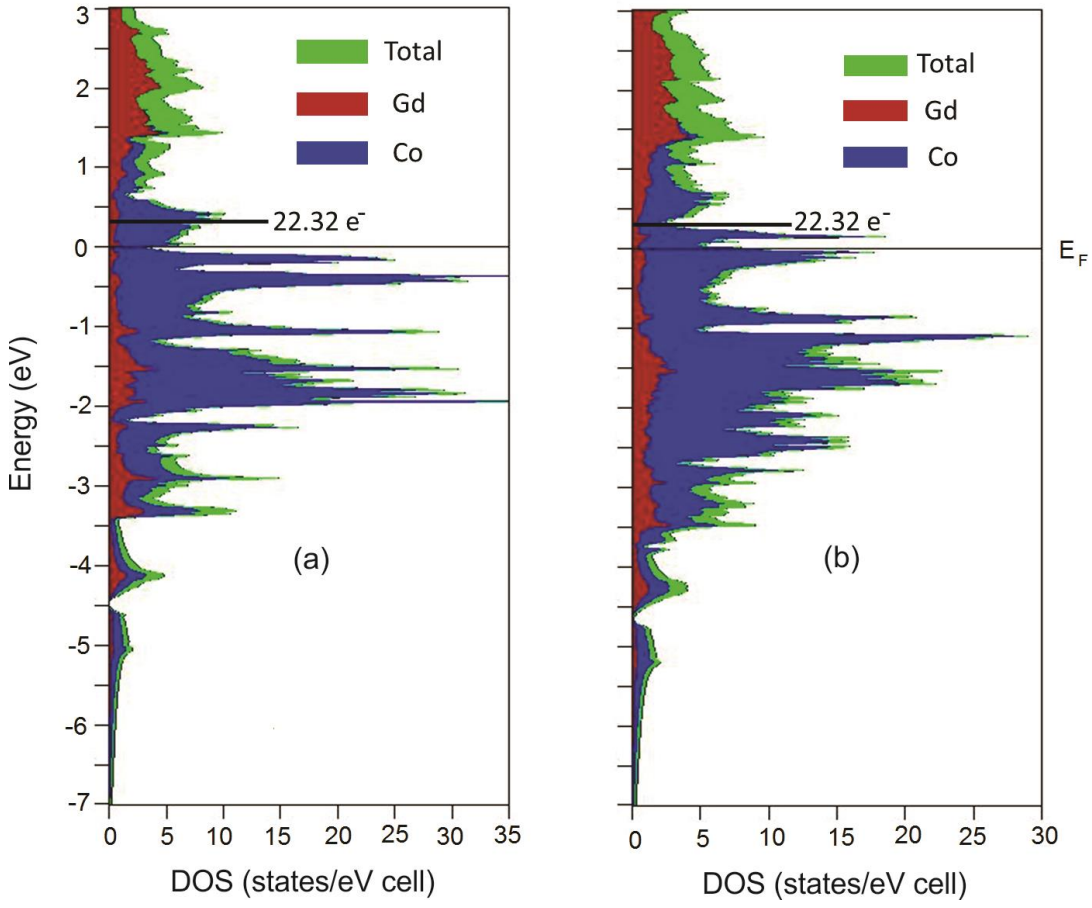

Figure 5.3. DOS calculated with LDA **(a)** and LSDA **(b)** for $GdCo_2$.

Table 5.5. Unit cell parameters and bond length for $GdCo_2$.

Sample	a (Å)	Co-Co bond length (Å)	Gd-Co bond length (Å)
$GdCo_2$ single crystal	7.2518 (8)	2.5639 (3)	3.0064 (3)
$GdCo_2$VASP LDA opt.	6.9772	2.4660	2.8926
$GdCo_2$VASP LSDA opt.	7.1752	2.5343	2.9717

Since $GdCo_{1.67}Ga_{0.33}$ and $GdCo_2$ have the same cubic structure and are only a couple electrons away from each other, the rigid band model might give some indications about the electronic properties of $GdCo_{1.67}Ga_{0.33}$ from the calculations on $GdCo_2$. For $GdCo_{1.67}Ga_{0.33}$, the VEC = 22.32 e^-/f.u. would place the Fermi level at ~0.3 eV on the DOS curves (the black line above the Fermi level of $GdCo_2$). More evidence that the spin polarization is needed to get accurate calculations could be observed by comparing the LDA and LSDA DOS curves. In the non-polarized calculations, this VEC would place the Fermi level on a large peak in the DOS curve, suggesting an electronic instability. When the spin polarization is added, the Fermi level at 0.3 eV resides in a pseudogap, which implies a greater electronic stability (**Figure 5.3**)

Figure 5.4 displays the COHP curves for all the types of bonding in $GdCo_2$. It is apparent that Co-Co interactions dominate the overall bonding in the structure. The rough percentages of the different bonding types were calculated after taking the listed bonds and the corresponding numbers per unit cell in the structure: Co-Co = 49.04%, Gd-Co = 46.04%, Gd-Gd = 4.92%. (**Table 5.6**) In looking at the middle COHP curve shown

below, the red filled in area is the entire Co-Co bonding whereas the black is only the majority spin Co-Co bonding. The bonding is optimized at the Fermi level and lies in a valley between two anti-bonding Co-Co peaks in the COHP. Another important aspect is the VEC of $GdCo_{1.67}Ga_{0.33}$ (22.32 e^- around 0.3 eV) resides in another pseudogap of the Co-Co anti-bonding states in the COHP curve, therefore, the Co-Co bonding is again close to being optimized. This is another indication that the $GdCo_{1.67}Ga_{0.33}$ compound is electronically stable.

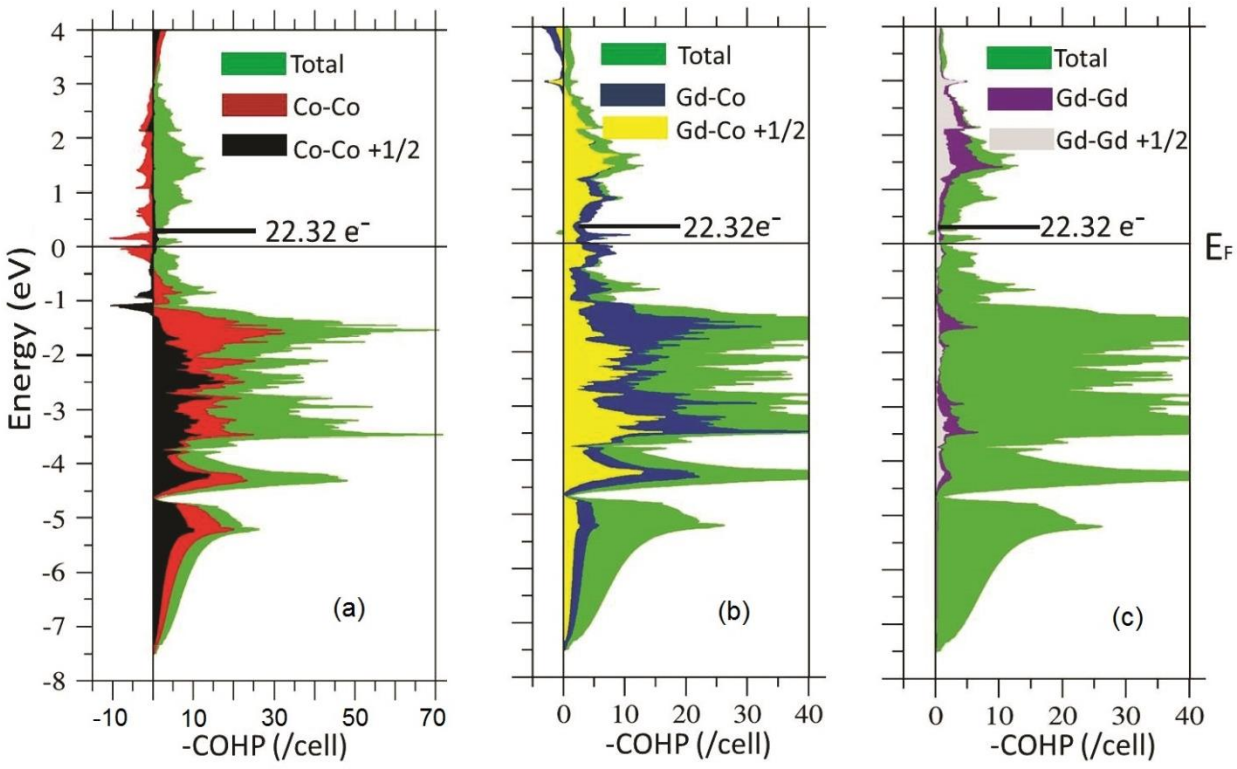

Figure 5.4. COHP curves calculated with LSDA for all the types of bonding in $GdCo_2$, +1/2 denotes the majority contribution.

Table 5.6. Bond types, their number and contribution to the total bonding in $MgCu_2$-type $GdCo_2$.

Bonds	Distance (Å)	No./unit cell	% total
Co-Co	2.565	48	49.04
Co-Gd	3.008	96	46.04
Gd-Gd	3.142	16	4.92

When looking at the DOS and COHP plots of $GdCo_2$ (**Figure 5.3 and Figure 5.4**), one notices that even though there are a lot of states around the Fermi level in the DOS, the COHP shows weak bonding for ~-0.5-0.5 eV. This suggests that the VEC can be either increased or decreased without a large effect on the structure, in other words, $MgCu_2$-type $GdCo_2$ is ripe for doping. The Co-Co interactions switch from positive to negative values (transitioning from bonding to anti-bonding) at ~-0.5 eV which corresponds to 19.1 electrons per formula unit (e^-/f.u.). The VEC of 19.1 e^-/f.u. matches the $GdFe_2$ binary, which also adopts the same structure. In addition to $GdFe_2$ and $GdCo_2$, $GdNi_2$ with VEC = 23 e^-/f.u. crystallizes with the cubic Laves structure. In the COHP curve for $GdCo_2$, the Co-Co interactions are optimized at the VEC = 19 e^-/f.u., and reside in a pseudogap at 21 e^-/f.u. and become slightly anti-bonding at 23 e^-/f.u. This suggests that the overall *T-T* bonding is sacrificed in favor of the *RE-T* bonding in the RET_2 (*T* = transition metals) Laves phase as the VEC is increased. Also, these calculations suggest that 23 e^-/f.u. is the highest VEC that the cubic Laves phase structure can sustain in this system before structural transitions occur. This argument is supported experimentally as the first transition is observed for the VEC = 23.68 e^-/f.u. ($GdCo_{1.33}Ga_{0.67}$).

5.3.3.2 Electronic Structure of Orthorhombic GdCoGa (Pnma)

GdCoGa adopts a MgSrSi-type structure. This structure is very common in the 111 compounds with a varying VEC, e.g. MgPtGa (15 e^-/f.u.), CaPtGa (15 e^-/f.u.), GdPtGa (16 e^-/f.u.), CaPtGe (16 e^-/f.u.), and GdPtGe (17 e^-/f.u.). **Figure 5.5** shows the DOS and the COHP curves, calculated for the structure refined from the X-ray single crystal data. One major difference between GdCoGa and $GdCo_2$ is that there are no Co-Co interactions. In GdCoGa the Co-Ga interactions dominate the contribution to the overall COHP curve, even though there are fewer bonds/unit cell compared with the other bond types: 42.16% vs. 27.39% and 26.54% for the Gd-Co and Gd-Ga interactions, respectively. The Gd-Gd interactions contribute 3.91% to the total COHP character. (**Table 5.7**)

Table 5.7. Bond types, their number and contribution to the total bonding in the unit cell of orthorhombic GdCoGa.

Bonds	No./unit cell	% total
Gd-Co	24	27.39
Gd-Ga	24	26.54
Gd-Gd	16	3.91
Co-Ga	16	42.16

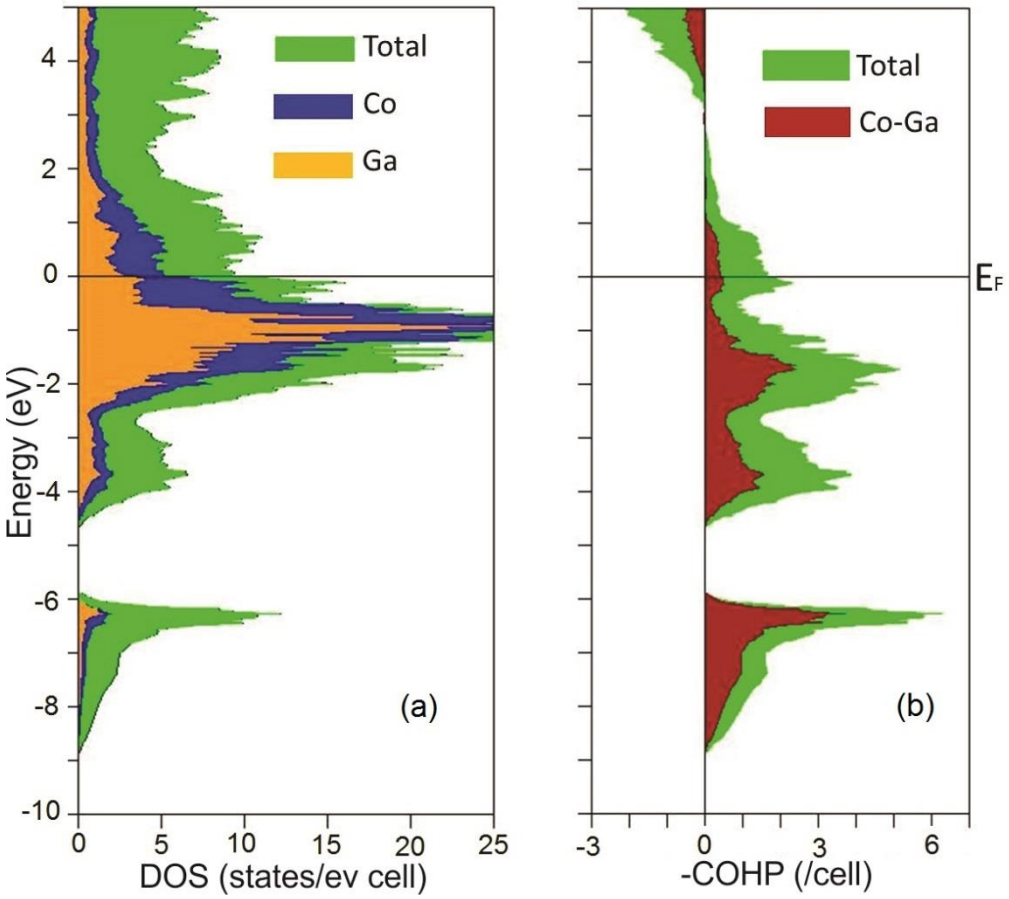

Figure 5.5. **(a)** DOS and **(b)** COHP calculated with LSDA for for experimental GdCoGa.

A structure optimization was performed using the VASP by letting all parameters relax and move. This created a unit cell different to the experimentally determined one. GdCoGa has experimental lattice parameters of a = 7.1110 Å, b = 4.3887 Å and c = 7.3400 Å (Table 2). The VASP optimization converged with a = 7.1644 Å, b = 4.4811 Å and c = 6.7719 Å. There is a slight increase in the a and b lattice parameters, but a significant decrease in the c parameter. A total energy was calculated for the experimental structure and it converged at -25.39170 eV. Total energy for the optimized structure

converged at -25.47522 eV, which shows that the optimized structure is favored by 0.08352 eV/Gd. There must be some driving force to cause such optimization results. When calculating the COHP for the optimized structure, faint Co-Co interactions are observed in the structure. The 111 phase has the zig-zag chains of "4 membered rings." In the experimental structure these "squares" have two bond angles of ~85° and two bond angles of ~95°. The VASP optimized structure has two bond angles of ~80° and two bond angles of ~100°. This "canting" of the squares has caused the Co atoms on opposite corners to come closer so that some weak Co-Co interactions developed. These interactions account only for 2.16% of the overall bonding (**Table 5.8**), which is partially due to their low occurrence in the unit cell.

Table 5.8. Bond types, their number and contribution to the total bonding in the unit cell of VASP optimized orthorhombic GdCoGa.

Bonds	No./unit cell	% total
Gd-Co	24	25.47
Gd-Ga	24	25.00
Gd-Gd	16	4.26
Co-Ga	16	43.11
Co-Co	8	2.16

The DOS calculated for the VASP optimized structure is shown in **Figure 5.6** and compared with the DOS of the experimental structure. The overall shape is similar, which is to be expected; however in the optimized structure the Fermi level resides at a lower

DOS, which can show a greater electronic stability. In the optimized structure there are also fewer Co states at and below the Fermi level.

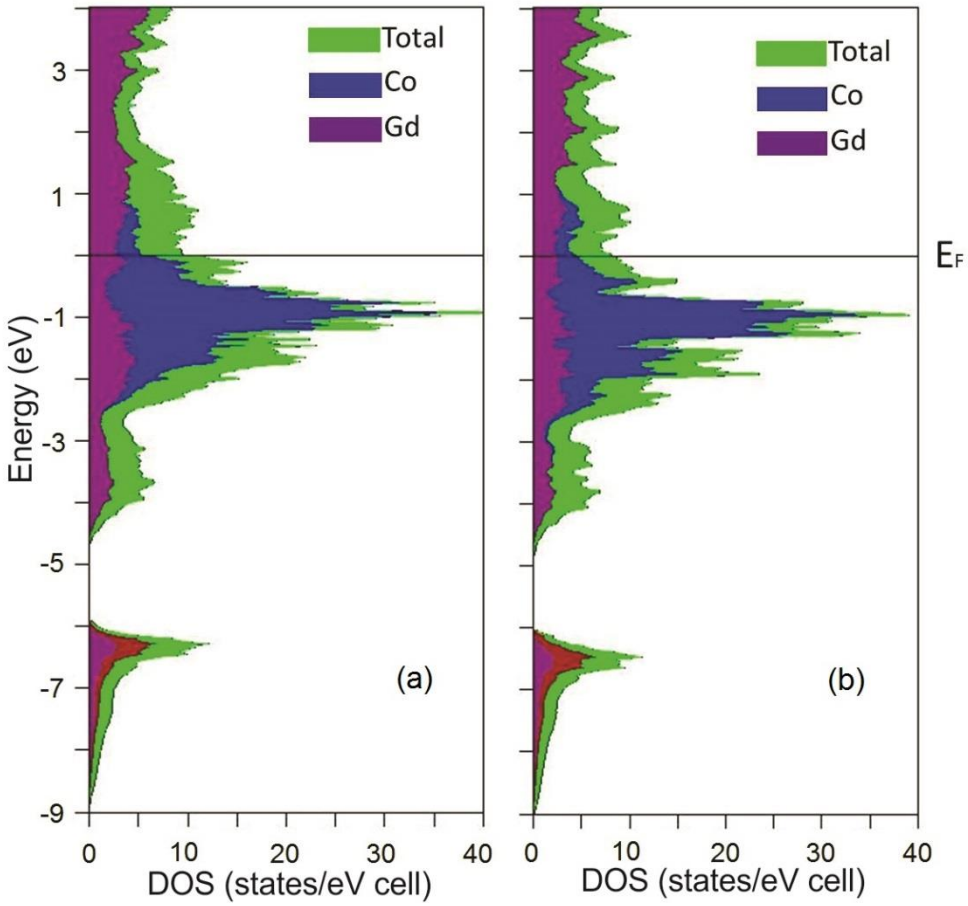

Figure 5.6. DOS calculated with LSDA for experimental **(a)** and VASP optimized **(b)** GdCoGa.

5.3.3.3 Electronic Structure of Hexagonal AlB_2-type $GdCo_{0.33}Ga_{1.67}$ and $GdGa_2$

Figure 5.7 shows DOS and COHP curves for the AlB_2-type $GdGa_2$ calculated using the LDA and LSDA methods. The main difference in the DOS plots is the width and depth of the pseudogap. The VASP LSDA optimized lattice parameters for $GdGa_2$

are slightly different from the experimental ones (**Table 5.9**), suggesting that spin polarization is necessary for the electronic calculation of $GdGa_2$. The DOS of $GdGa_2$ (VEC = 9 electrons) resides on the shoulder of a peak. The COHP data indicate that the Gd-Ga interactions (partially due to having 4x more bonds per unit cell than the Ga-Ga interactions) have the largest contribution followed by the Ga-Ga interactions, and then by the Gd-Gd interactions (**Table 5.10**). The Ga atoms form the graphene-like sheets, and each Ga has 3 bonds to other Ga in these sheets. There is a pseudogap in the DOS corresponding to 9.9 electrons, and the center of the pseudogap coincides with transitions from bonding to anti-bonding interactions in the COHP plot. Above 9.9 electrons, the Ga-Ga anti-bonding states are being filled, as a result, the graphene-like sheets should become disrupted and be no longer planar as they distort to handle a higher electron count. Even though the overall bonding contribution of these sheets is less than the contribution of the Gd-Ga bonding, the graphene-like sheets will be disrupted first at the VEC above 9.9 e^-/f.u.

Since the ternary $GdCo_{0.33}Ga_{1.67}$ compound has the same structure as $GdGa_2$, but a different VEC, the rigid band model can be used to infer its electronic structure. In $GdCo_{0.33}Ga_{1.67}$, the Co *d* states will be below the Fermi level and are expected to be fully occupied, which would translate into VEC reduction by 1 for each Co atom. Therefore, the VEC for $GdCo_{0.33}Ga_{1.67}$ is 7.68e^-/formula unit, and the Fermi level resides at ~-1eV. There is a large peak in the DOS at that energy, which suggests an electronic instability, and likely that the approach taken is not the best and other alternatives should be explored for $GdCo_{0.33}Ga_{1.67}$.

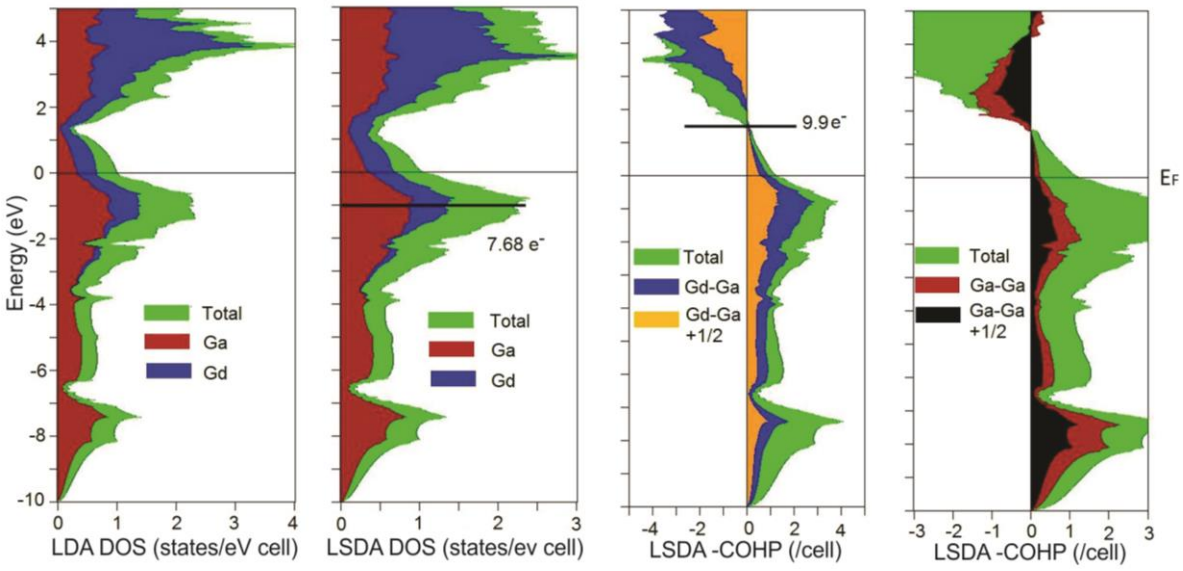

Figure 5.7. DOS and COHP calculated with LDA or LSDA for $GdGa_2$, +1/2 denotes the majority contribution.

Table 5.9. Unit cell parameters for $GdGa_2$.

Sample	*a* (Å)	*c* (Å)
$GdGa_2$ single crystal	4.2201	4.1342
$GdGa_2$VASP LSDA opt.	4.2477	4.1420

Table 5.10. Bond types, their number and contribution to the total bonds in the unit cell of $GdGa_2$.

Bonds	Distance (Å)	No./unit cell	% total
Gd-Ga	3.195	12	52.92
Ga-Ga	2.436	3	36.25
Gd-Gd	4.220	8	10.83

5.4 Conclusions

$Gd(Co_{1-x}Ga_x)_2$ (x = 0, 1/6, 1/3, 1/2, 2/3, 5/6, and 1) phases adopt five structures as a function of the x value. The structures change from a "condensed cluster-based" → "3D Network" → "2D Network" with an increasing Ga content. In terms of coordination numbers (CN), the CN of Co or Ga is 6 in the cubic $GdCo_2$, then reduces to 4 in the 3D network, and finally to 3 in the 2D network. Electronic factors appear to be the reason for the structural transformations in the $Gd(Co_{1-x}Ga_x)_2$ system. Spin polarization appears necessary for the TB-LMTO-ASA calculations in this work, therefore, DOS and COHP were calculated using the LSDA. $GdCo_2$ adopts a cubic $MgCu_2$-type structure, which could be sustained to the VEC = 23 e^-/f.u. Therefore, $GdCo_{1.67}Ga_{0.33}$ (22.32 e^-/f.u.) adopts the same $MgCu_2$-type structure, while a structural transition occurs for $GdCo_{1.33}Ga_{0.67}$ with VEC = 23.68 e^-/f.u. Although Co-Ga bonds are fewer compared with other bonds, they dominate the total bonding in the unit cell of orthorhombic GdCoGa. The VASP optimization of the GdCoGa structure generates a unit cell with a smaller c lattice parameter, which is attributed to the development of some weak Co-Co interactions in the optimized structure. The total energy calculation suggests that the optimized structure is favored by 0.08352 eV/Gd. $GdGa_2$ has a VEC of 9 e^-/f.u. and a pseudogap at 9.9 e^-/f.u. Although COHP data indicates that Gd-Ga bonds contribute the most to the overall bonding, Ga-Ga bonds, which form graphene-like sheets, are first to break above the VEC of 9.9 e^-/f.u. Ga substitution reduces the strength of the long-range magnetic interactions, which causes T_C to decrease with an increasing Ga content.

Chapter 6. Conclusions and Future Work

In this dissertation, synthesis, structural features, and physical properties of a few groups of *RE*-based alloys are presented. The driving force behind these projects is to obtain new magnetocaloric materials. Although all of the phases studied have little application potential due to low transition temperatures or poor MCEs, some of them may be attractive for the further material optimization due to their tunable physical properties and easy synthesis. In addition, the investigation of the relationship between the composition, crystal structure, and magnetic properties provides some valuable guidance for the discovery of new magnetocaloric materials in future.

6.1 $RE_5(Ga_{1-x}T_x)_3$ Phases (*RE* = Rare Earth, and *T* = 3*d* Transition Metals)

6.1.1 Structural Features and Physical Properties

Ho_5Ga_3 and Er_5Ga_3 phases both adopt a Mn_5Si_3-type structure, while Dy_5Ga_3 adopts a Cr_5B_3-type structure. An interesting Mn_5Si_3-type-to-Cr_5B_3-type transformation was obtained in the $Ho_5Ga_{3-x}Co_x$ and $Er_5Ga_{3-x}(Fe/Co)_x$ systems, which is attributed to the differences in the atomic sizes. The compositions of pure Cr_5B_3-type phases are $Ho_5Ga_{2.6}Co_{0.4}$ and $ErGa_{2.6}Fe_{0.4}$, where the atomic size difference between Ho and Co, Er and Fe is identical to that between Dy and Ga, which may explain why pure Cr_5B_3-type phases are formed in both samples (r_{Fe} = 1.24 Å, r_{Co} = 1.25 Å, r_{Ga} = 1.26 Å, r_{Er} = 1.73 Å, r_{Ho} = 1.74 Å and r_{Dy} = 1.75 Å).[109] Additionally, the cast samples were not pure, therefore,

annealing at 900°C for 1 week was required to transform the Mn_5Si_3-type polymorph into the Cr_5B_3-type one.

The Mn_5Si_3-type RE_5Ga_3 phases are not suitable for magnetic refrigeration due to the antiferromagnetism or paramagnetism[64,124]. Through substitution of Co for Ga, the ground magnetic state of $Ho_5Ga_{3-x}Co_x$ (x = 0.3 and 0.4) is transformed to a ferromagnetic one. However, the field-dependence magnetization does not saturate at 5K and 50 kOe, which indicates that the ground magnetic state is not a pure ferromagnetic one but contain some antiferromagnetic contributions. The magnetocaloric effect in terms of the isothermal magnetic entropy change, ΔS_{mag}, was studied for $Ho_5Ga_{3-x}Co_x$ (x = 0.3 and 0.4). And $-\Delta S_{mag}$ peaks around T_C, with the maximum value of 10.2 and 12.7 J/(kgK), respectively. The moderate magnetic entropy change implies absence of a first-order magneto-structural transition.

6.1.2 Further Exploration of the $RE_5(T_{1-x}Ga_x)_3$ Phases

Investigation of the structural and magnetic properties of the $Ho_5Ga_{3-x}Co_x$ system yielded interesting results: the substitution of Co for Ga not only induced a Mn_5Si_3-type-to-Cr_5B_3-type structural change, but also resulted in the antiferromagnetic-to-ferromagnetic transition. Presence of the ferromagnetic ground state makes the Co-substituted RE_5Ga_3 compounds more attractive in terms of magnetocaloric applications. Building on the success of the $Ho_5Ga_{3-x}Co_x$ project, some novel 3*d* metal-substituted phases could be explored near the RE_5Ga_3 composition and that lie close to the boundary between the two structure types (**Figure 6.1**), namely around Pr_5Ga_3, Nd_5Ga_3, Ce_5Ga_3,

Dy_5Ga_3 and Ho_5Ga_3. The choice of these phases is dictated by the idea that atomic size controls the structure type, and thus by varying the effective atomic size of the Ga site through substitution we can stabilize a specific structure.

Out of the 3*d* metals, we can focus on the magnetically active ones: Mn, Fe, Co and Ni. In addition to the possibility of affecting the ground magnetic state, these elements may carry magnetic moments, and thus may enhance magnetization and magnetocaloric effect. The size difference between Mn and Ni can allow to "push" the two neighbouring structures into the opposite structural fields. For example, Mn substitution in Dy_5Ga_3 should stabilize the Mn_5Si_3 structure for $Dy_5Ga_{3-x}Mn_x$, while Ni substitution in Ho_5Ga_3 should yield the Cr_5B_3 structure for $Ho_5Ga_{3-x}Ni_x$. Since Co and Ni have similar atomic sizes, exploration of the Co- and Ni-substituted RE_5Ga_3 phases with the same rare-earth should identify the role of the valence electron concentration on the structure stability. For example, in Chapter 3, we have shown that the Co substitution stabilizes the Cr_5B_3 structure for $Ho_5Ga_{3-x}Co_x$, and the question can be asked whether Ni substitution will promote the same structure and at the same substitution levels. In addition, electronic structure calculations could be performed to understand bonding and/or structure preference for a given phase.

Table 6.1. The atomic radii of selected 3*d* metals and Ga.

Element	Mn	Fe	Co	Ni	Ga
Radius (Å)	1.37	1.24	1.25	1.25	1.26

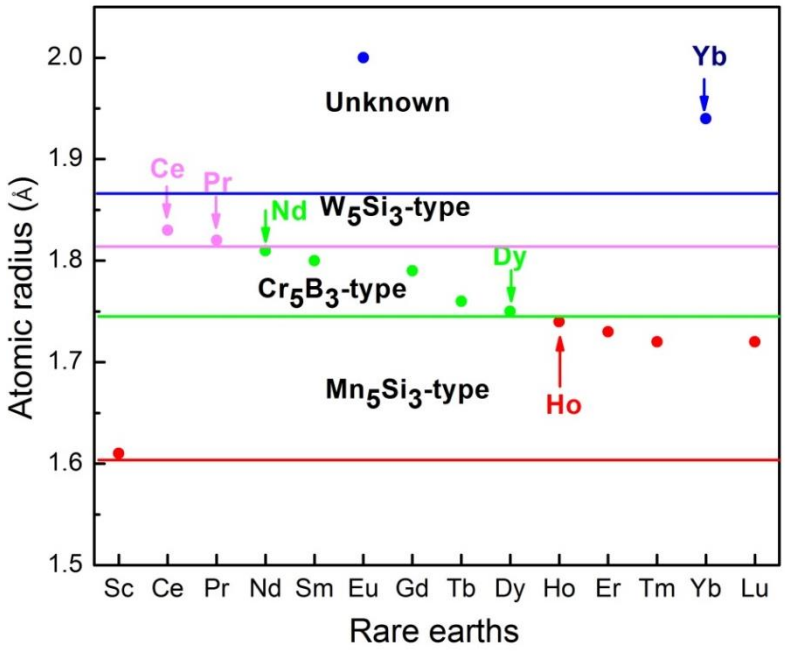

Figure 6.1. Atomic size as a function of rare earths. The horizontal lines indicate the boundaries between different structures.

6.2. The *RE*Co_2-based Phases

6.2.1 Structural Features and Physical Properties

When studying the *RE*Co_2-based phases, hexagonal $MgZn_2$-type phases with the *RE*$(Co_{0.667}Ga_{0.333})_2$ stoichiometries (*RE* = Gd, Tb, Dy, Ho, and Er) and an interesting structural sequence in the Gd$(Co_{1-x}Ga_x)_2$ system ($0 \leq x \leq 1$) were observed. The $MgZn_2$-type *RE*$(Co_{0.667}Ga_{0.333})_2$ phases appear to be formed by a peritectic reaction between the cubic Laves phase and Gd-rich liquid. Although the magnetic order of $MgZn_2$-type *RE*$(Co_{0.667}Ga_{0.333})_2$ phases (*RE* = Ho, and Er) is not confirmed, the other three phases are proved to be ferromagnetic (*RE* = Gd, Tb, and Dy). The MCE of Gd$(Co_{0.667}Ga_{0.333})_2$ was studied and it peaks around 150K. However, a relatively small value of -4.94 J/(kgK)

suggests a conventional MCE. There are three crystallographic sites: 2*a*, 4*f* and 6*h* in a hexagonal $MgZn_2$-type structure. The Co/Ga distribution on the 2*a* and 6*h* sites could not be reliably established from X-ray diffraction due to the similar atomic scattering factors of Co and Ga. Neutron diffraction were performed in order to refine the Co/Ga occupancies and establish the magnetic ground state of $RE(Co_{0.667}Ga_{0.333})_2$ (*RE* = Ho, and Er). (**Appendix 2**)

Alloys with the $Gd(Co_{1-x}Ga_x)_2$ compositions (x = 0, 1/6, 1/3, 1/2, 2/3, 5/6, 1) were prepared to systematically study the structural transformation in the pseudobinary $GdCo_2$-$GdGa_2$ system. Five structures observed in $Gd(Co_{1-x}Ga_x)_2$ features the "condensed cluster-based arrangement" →"3D Network" → "2D Network" transition with the increase of Ga content. In addition, coordination number (CN) of Co or Ga is closely related to the type of networks: 6 for cluster-based cubic Laves phase, 4 for 3D network, and 3 for 2D network. Electronic structure calculations suggest that the structural transformation in $Gd(Co_{1-x}Ga_{x)2}$ could be related to the valence electron counts (VEC).

6.2.1 Further Exploration of the *RE*Co_2-based Phases

Studies on $Gd(Co_{1-x}Ga_{x)2}$ suggest that GdCoGa (x = 1/2) adopts an orthorhombic MgSrSi-type structure, but the sample is not pure yet. To obtain a phase-pure sample, different annealings will be attempted.

Appendix 2 shows neutron powder diffraction results, which allow us to refine the Co/Ga occupancies on the 2*a* and 6*h* sites. The magnetic structures of $Ho(Co_{0.667}Ga_{0.333})_2$

and $Er(Co_{0.667}Ga_{0.333})_2$ are found to be significantly different. Therefore, it is interesting to perform neutron powder diffraction studies on other $RE(Co_{0.667}Ga_{0.333})_2$ phases.

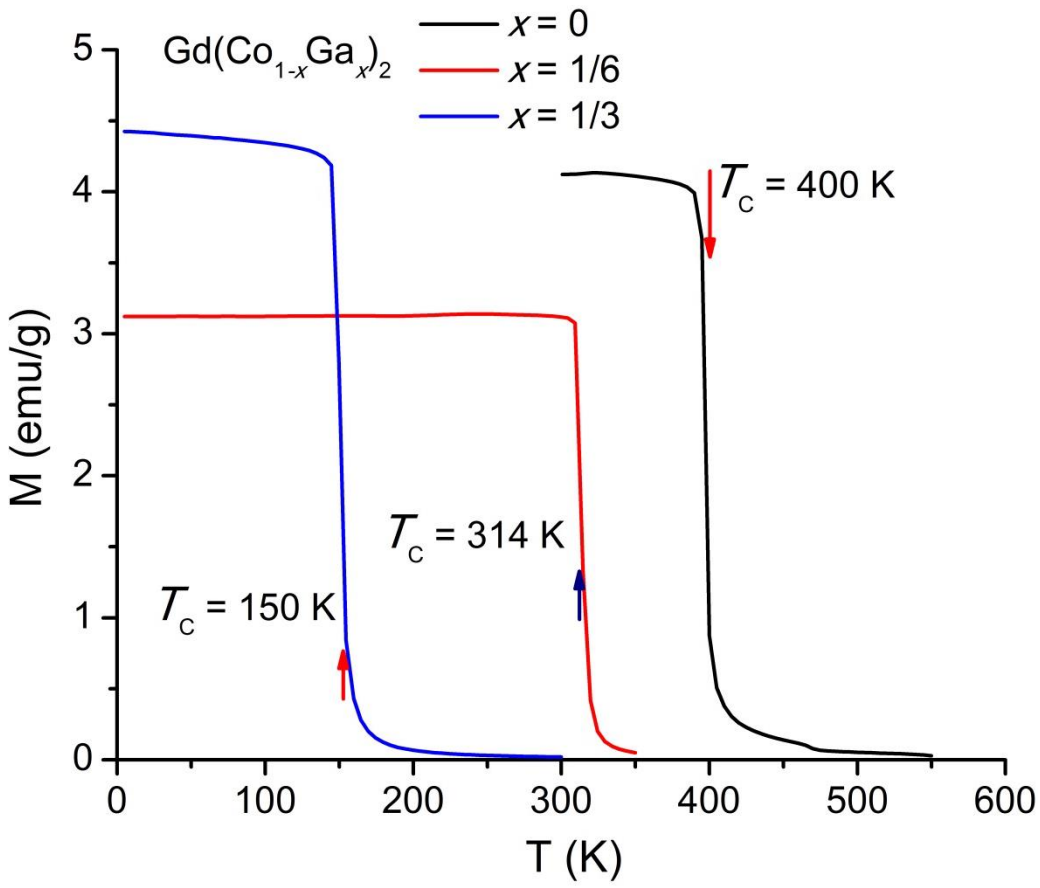

Figure 6.2. Magnetization vs. temperature for annealed annealed $Gd(Co_{1-x}Ga_x)_2$ (x = 0, 1/6, and 1/3).

In terms of room-temperature (RT) MCE, the $Gd(Co_{1-x}Ga_x)_2$ alloys with $1/6 \leq x \leq 1/3$ are very interesting. As shown in **Figure 6.2**, T_C of $Gd(Co_{1-x}Ga_x)_2$ with x = 0, 1/6 and 1/3 is 400, 314 and 150K, respectively. Therefore, T_C is very sensitive to the Ga content in the $Gd(Co_{1-x}Ga_x)_2$ system. The novel $Gd(Co_{1-x}Ga_x)_2$ ($1/6 \leq x \leq 1/3$) phases will be

prepared to explore RT magnetocaloric materials. Additionally, $Gd(Co_{1-x}Ga_x)_2$ ($1/6 \leq x \leq 1/3$) phases may undergo interesting structural changes since $Gd(Co_{1-x}Ga_x)_2$ with $x = 1/6$ and 1/3 adopts a cubic and hexagonal structure, respectively. While still quite rare, a coupled first-order magnetostructural transition may yield a giant magnetocaloric effect (GMCE).

Appendix 1. Structure and Physical Properties of Cr_5B_3-type Ta_5Si_3 and Ta_5Ge_3

This chapter contains the material covered in the manuscript "Structure and Physical Properties of Cr_5B_3-type Ta_5Si_3 and Ta_5Ge_3", which was published in Journal of Alloys and Compounds (*J. Alloys Compd.* **2015,** 65, 712-717). The experimental procedures, structure determinations, data interpretations, and manuscript preparation were performed by the candidate. Dr. Scott Forbes assisted with the electronic structure calculations, and Dr. Krishna Kumar Ramachandran carried out electrical resistivity measurement.

The Cr_5B_3-type Ta_5Si_3 phase was prepared by arc-melting, while the Cr_5B_3-type Ta_5Ge_3 one was synthesized through sintering at 1000℃. X-ray single crystal diffraction was employed to elucidate their structure. According to the magnetization measurements, both Ta_5Si_3 and Ta_5Ge_3 are Pauli paramagnets, with Ta_5Ge_3 showing a Curie-Weiss-like paramagnetic behavior at low temperatures likely due to presence of paramagnetic impurity. Both Ta_5Si_3 and Ta_5Ge_3 display a very low electrical resistivity from 2 to 300 K. The resistivity is constant below 20K, but displays a positive temperature coefficient above 20K. Electronic structure calculations with the TB-LMTO-ASA method support the metallic character of the two phases and suggest that the bonding is optimized in both phases.

A1.1 Introduction

Sulphides, selenides and tellurides have a relatively low stability at high temperatures. On the other hand, germanides and silicides formed by transition metals usually exhibit excellent thermal stability, oxidation resistance, high stress and compressive strength, which is quite favourable for the applications at elevated temperatures.[125–127] For example, these materials may be used for thermoelectric power-generation at temperatures close to 1000^{o}C. Although the resistivity of some metallic germanides and silicides increases with temperature, the decreasing thermal conductivity and increasing Seebeck coefficient may compensate for it.[128] So far, study of the structure and physical properties of germanides and silicides appears not very systematic, and in general, the factors governing their stability are not well understood.

Since Si and Ge belong to the same group and have similar atomic sizes, germanides formed by transition metals are closely related to silicides in respect to their compositions, structures and properties. For example, Ti_5Ge_3 and Mn_5Ge_3 were reported to be isostructural with analogous silicides[129–134]. Additionally, some silicides and germanides are known to have different polymorphs. E.g., Ta_5Si_3 was reported to have three different structures: Mn_5Si_3, W_5Si_3 and Cr_5B_3 type[135–138]. The Mn_5Si_3-type Ta_5Si_3 phase with the $P6_3/mcm$ symmetry was found to be metastable but could be stabilized through metalloid substitution. The two other polymorphs have the $I4/mcm$ symmetry; the W_5Si_3-type Ta_5Si_3 phase with $a = 7.47$ Å and $c = 5.23$ Å ($a > c$) is a high-temperature form, while the Cr_5B_3-type Ta_5Si_3 with $a = 6.52$ Å and $c = 11.87$ Å ($a < c$) is a low-temperature form. The W_5Si_3-to-Cr_5B_3 structural transformation was reported to occur at 2160°C. The formation enthalpies decrease in the following order: Mn_5Si_3-, W_5Si_3-, Cr_5B_3-type, making the Cr_5B_3-type structure the most stable[135]. In our present work, we will focus on the most stable Cr_5B_3-type modification of Ta_5Si_3.

The Mn_5Si_3-type Ta_5Ge_3 has been reported by E. Parth*é* and W. Jeitschko[139,140]. Parth*é* also reported on the W_5Si_3-type Ta_5Ge_3 phase, but the Cr_5B_3-type Ta_5Ge_3 has not been observed. In 1956, H. Nowotny *et al*. reported on the stabilization of the W_5Si_3-type and Cr_5B_3-type structures for the $TaGe_{0.5}$ (Ta_2Ge) stoichiometry, but crystallographic parameters and exact compositions were not given[141]. Intermetallic compounds containing Ta are usually prepared by special techniques due to the high melting point of Ta, e.g. by hot-pressing in graphite dies above 1000°C. In our present study, the high-purity Cr_5B_3-type Ta_5Si_3 and Ta_5Ge_3 phases were synthesized by simple methods, either

arc-melting or sintering. Since the structures of transition metal germanides and silicides are sensitive to impurities, in particular carbon and oxygen[129,139,141], high purity argon or high vacuum were used. To explore the structural and physical properties of the two phases systematically, single crystal diffraction, electronic band structure calculations, magnetic and resistivity measurements were performed.

A1.2 Experimental

A1.2.1 Synthesis

Pieces of Ta (99.999 wt. %, Alfa Aesar) and Si (99.9999 wt. %, Alfa Aesar) with the target sample mass of 1 gram were arc-melted under pure argon atmosphere, and the resulting button was re-melted 3 times to improve homogeneity. Excess of 30 % Si was added to compensate for the Si loss. The synthesis of Ta_5Ge_3 proceeded from the Ta powder (99.9999 wt. %, Alfa Aesar) and Ge (99.9999 wt. %, Alfa Aesar) pieces. Ge pieces were ground and mixed with the Ta powder in the 3:5 molar ratio in an Ar-filled glovebox. The mixture was pressed, sealed in an evacuated silica tube, heated to 600^{o}C at 20^{o}C /hour, kept at this temperature for 24 hours, then heated to 1000^{o}C at 50^{o}C /hour, kept at this temperature for 48 hours, and subsequently quenched in cold water. To improve the homogeneity and crystallinity, the Ta_5Ge_3 sample was reground, pressed into pellet, sealed in an evacuated silica tube, heated to 1000^{o}C at 100^{o}C/hour, kept at this temperature for 1 week, and subsequently quenched in cold water. During sintering, no weight losses were detected.

A1.2.2 X-ray Analysis

Phase analyses of the polycrystalline Ta_5Si_3 and Ta_5Ge_3 samples at room-temperature were performed on a PANalytical X'Pert Pro diffractometer with a linear X'Celerator detector, Cu$K\alpha_1$ radiation and in the 2θ range from 20 to 70 or 80°. The lattice parameters were derived from a full-profile Rietveld refinement (*Rietica* program)[89]. The Ta_5Si_3 and Ta_5Ge_3 phases adopt the Cr_5B_3-type structure with the space group *I*4/mcm. The Ta atoms sit on the 16*l* and 4*c* sites, while Si or Ge atoms are on the 4*a* and 8*h* sites. The refined powder patterns are shown in **Figure A1.1** and **Figure A1.2** and their crystallographic data are summarized in **Table A1.1**. As shown in Fig.1, there are some extra weak peaks (2θ = 20-40°) from the $TaSi_2$ impurity, while the extra peaks in **Figure A1.2** result from pure Ta phase. The weight percent of the impurities is about 1%.

Table A1.1. Crystallographic data for the Ta_5Si_3 and Ta_5Ge_3 samples determined from the powder X-ray diffraction.

Composition	treatment	Str. type	*a*, Å	*c*, Å	*V*, Å^3
Ta_5Si_3	cast	Cr_5B_3	6.51718(8)	11.8765(2)	504.44(1)
Ta_5Ge_3	annealed	Cr_5B_3	6.62144(6)	12.0284(2)	527.37(1)

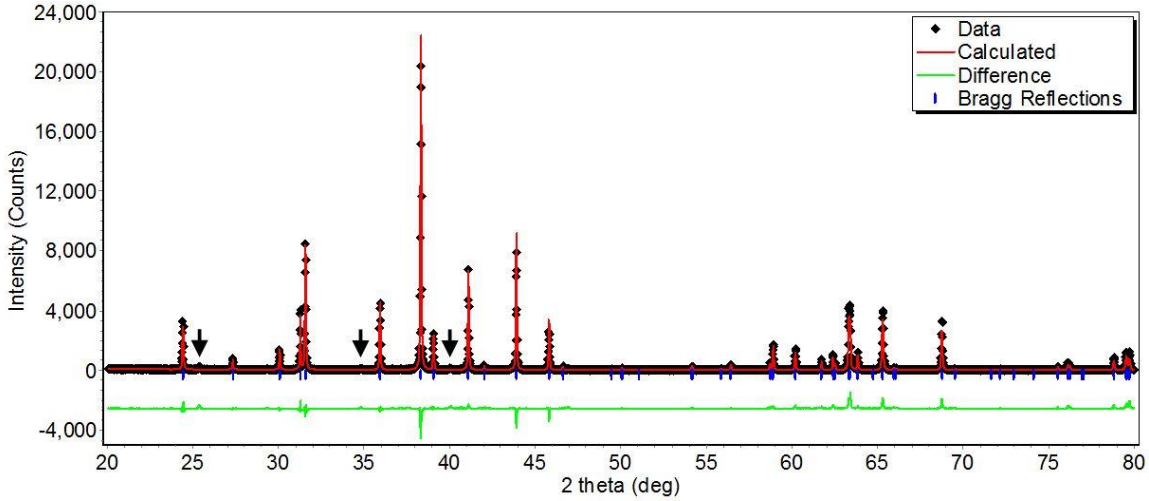

Figure A1.1. Powder X-ray diffraction patterns and Rietveld refinements of Cr_5B_3-type Ta_5Si_3. The $TaSi_2$ impurity is indicated with arrows.

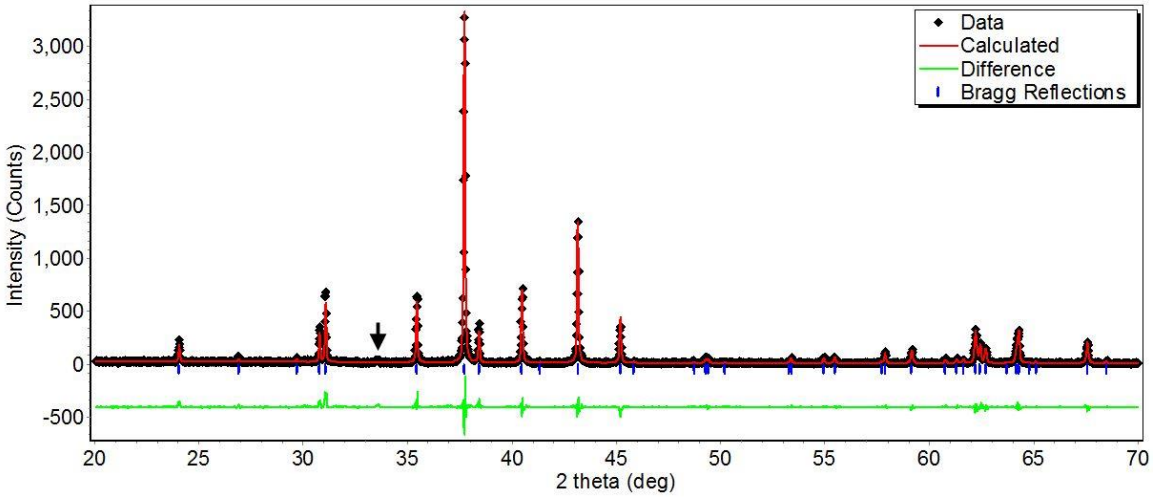

Figure A1.2. Powder X-ray diffraction patterns and Rietveld refinements of Cr_5B_3-type Ta_5Ge_3. The Ta impurity is indicated with an arrow.

The single crystals extracted from the Ta_5Si_3 and Ta_5Ge_3 samples were analyzed on a STOE IPDS II diffractometer with the Mo*K*α radiation. Numerical absorption corrections were based on the crystal shapes derived from optical face indexing and later

optimized against equivalent reflections using the STOE *X*-Shape software[66]. Structural solution and refinement were performed using the *SHELXS* and *SHELXL* software packages, respectively[67]. Significant crystallographic results are summarized in **Table A1.2** and **A1.3**. The crystallographic and atomic parameters derived from the single crystal agree with those from the X-ray powder diffraction. No deficiencies were detected on the crystallographic sites, therefore, both the Ta_5Si_3 and Ta_5Ge_3 compositions are assumed stoichiometric.

Table A1.2. Crystallographic data and refinement results for Ta_5Si_3 and Ta_5Ge_3 (MoK_α radiation, 293K).

	Ta_5Si_3	Ta_5Ge_3
Refined composition	Ta_5Si_3	Ta_5Ge_3
Space group	*I* 4/*mcm*	*I* 4/*mcm*
Crystal size (mm)	0.0458 x 0.0782 x 0.0588	0.0620 x 0.0476 x 0.0362
***a* (Å)**	6.5071(9)	6.6094(9)
***c* (Å)**	11.860(2)	12.023(2)
Volume (Å^3)	502.2(1)	525.2(2)
ρ_{calc} (g/cm^3)	7.878	8.549
Z	4	4
Index ranges	$-8 \le h \le 8$, $-8 \le k \le 8$, $-12 \le l \le 16$	$-9 \le h \le 9$, $-9 \le k \le 9$, $-16 \le l \le 14$
2θ range (°)	8.86 to 58.22	6.78 to 58.28
Meas. Refl.	2458	2555
Ind. Refl.	194 (R_{int} = 0.1054)	214 (R_{int} = 0.0520)
Extinction coefficient	0.0006(1)	0.00147(7)
Number of param.	16	16
Largest peak / hole (e/Å^3)	2.578/-3.307	1.790/-2.033
Goodness-of-fit on $\|F^2\|$	1.089	1.159
R indices ([$I > 2\sigma(I)$])	R_1 = 0.0355, wR_2 = 0.0541	R_1 = 0.0185, wR_2 = 0.0302

Table A1.3. Atomic and isotropic temperature (U_{eq}, Å^2) parameters for Ta_5Si_3 and Ta_5Ge_3 from single crystal diffraction data.

Atom	Site	Occupancy	x/*a*	y/*b*	z/*c*	U_{eq} (Å^2)
			Ta_5Si_3			
Ta1	16*l*	1	0.1645(1)	0.3355(1)	0.1503(1)	0.004(1)
Ta2	4*c*	1	0	0	0	0.003(1)
Si1	4*a*	1	0	0	1/4	0.006(2)
Si2	8*h*	1	0.3705(9)	0.1295(9)	0	0.003(2)
			Ta_5Ge_3			
Ta1	16*l*	1	0.1607(1)	0.3393(1)	0.1538(1)	0.004(1)
Ta2	4*c*	1	0	0	0	0.003(1)
Ge1	4*a*	1	0	0	1/4	0.004(1)
Ge2	8*h*	1	0.3638(2)	0.1362(2)	0	0.003(1)

A1.2.3 Magnetic Properties Measurements.

Magnetic measurements were performed using a Superconducting Quantum Interference Device (SQUID) on the Magnetic Property Measurement System (MPMS) magnetometer. The temperature dependence of magnetization in a field-cooled (FC) mode for the Cr_5B_3-type Ta_5Si_3 and Ta_5Ge_3 phases was measured in 1 T field from 350 to 5K.

A1.2.4 Electrical Resistivity Measurements

Four-probe AC electrical resistivity for pellets of Ta_5Si_3 and Ta_5Ge_3 was measured on a Quantum Design Physical Properties Measurement System (PPMS) equipped with an ac transport controller (model 7100) in the temperature interval of 2-300K. All the contacts from pellet to the gold wires were made with silver paste (DuPont

4929N). The current was 100 μA, and the frequency was 16 Hz. Resistivity measurements were repeated twice to verify the data.

A1.2.5 Electronic Band Structure Calculations

The electronic structures of Cr_5B_3-type Ta_5Si_3 and Ta_5Ge_3 were calculated using the tight-binding, linear-muffin tin orbital method[142] with the atomic sphere approximation (TB-LMTO-ASA) as implemented in the Stuttgart program[70]. A scalar relativistic approximation[73] was used to account for all relativistic effects except spin-orbit coupling. Overlapping Wigner-Seitz (WS) cells were constructed with radius making the overlapping potential to be the best approximation to the full potential, according to the atomic sphere approximation (ASA). Space-filling empty spheres were constructed and included in the unit cell to satisfy the overlap criteria of the TB-LMTO-ASA model by the automatic sphere generation[74]. The lattice parameters and atomic coordinates for Cr_5B_3-type Ta_5Si_3 and Ta_5Ge_3 extracted from the X-ray single crystal data were used for calculations. The radii for the WS cell were generated automatically and the radii used for Ta_5Si_3 and Ta_5Ge_3 were: Ta = 1.56-1.60 Å, Si = 1.37-1.50 Å, Ta = 1.55-1.61 Å, Ge = 1.40-1.52 Å. The basis set included 6s and 5d orbitals for Ta, 4s and 4p orbitals for Ge, 3s and 3p orbitals for Si. The orbitals were treated using the Löwdin downfolding technique[143]. The Ta 4*f* orbitals were treated as core ones that do not participate in bonding. The orbital interactions were analyzed via density of states (DOS) and crystal orbital Hamilton population (COHP) calculations using the tetrahedron method[144]. For the COHP calculations, the maximum distance considered between two Ta atoms was 2.840 Å and 2.852 Å for Ta_5Si_3 and Ta_5Ge_3, respectively.

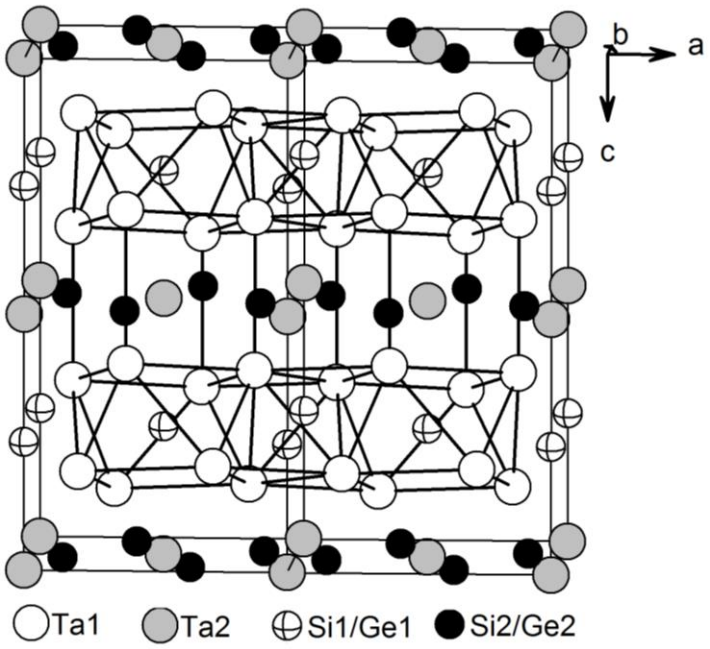

Figure A1.3. Crystal structures of Cr_5B_3-type $Ta_5Si_3$and Ta_5Ge_3 phases.

A1.3 Results and Discussion

A1.3.1 Compositions and Stability of Ta_5Si_3 and Ta_5Ge_3

Both the arc-melted Ta_5Si_3 and sintered Ta_5Ge_3 phases adopt a Cr_5B_3-type structure. The Cr_5B_3-type structure (*I*4/*mcm*) has two independent Ta and Si (or Ge) sites. The Ta1 atoms form two 3^2434 layers that are rotated by 45^o with respect to each other and alternate along the *c* direction. Stacking of these layers produces trigonal (occupied by Si2 or Ge2) and tetragonal (occupied by Ta2) prisms, tetragonal antiprisms (filled with Si1 or Ge1) and empty tetrahedra. (**Figure A1.3**)

The Ta_5Si_3 phase could not be synthesized by sintering at 1000^oC. X-ray powder diffraction analysis of the Ta_5Si_3 sample sintered at 1000^oC indicated presence of the

$TaSi_2$ phase, suggesting that 1000°C was not high enough to complete reaction between the Ta and Si powders. Since temperatures higher than the melting temperature of Si (T_m = 1414°C) could not be reached in silica tubes, arc-melting was used instead. However, the melting point of Ta (T_m = 3017°C) is close to the boiling point of Si (T_b = 3265°C), and significant amounts of Si were lost during the arc-melting. To compensate for the Si losses, excess of 30% Si was added to the sample. In contrast, Ta_5Ge_3 cannot be synthesized by arc-melting as the boiling point of Ge (T_b = 2833°C) is lower than the melting point of Ta, and almost all the Ge was lost during arc-melting. The Ta_5Ge_3 phase was synthesized by sintering at 1000°C, which is a higher than the melting point of Ge (T_m = 938°C). During sintering, no weight losses were observed. Based on X-ray powder diffraction analysis, both arc-melted Ta_5Si_3 and sintered Ta_5Ge_3 were of high purity and adopted the Cr_5B_3-type structure.

Similar to other reported silicides and germanides, the Cr_5B_3-type Ta_5Si_3 and Ta_5Ge_3 phases were stable in air, and no decomposition could be detected after several-day exposure in air. Compared with Ta_5Ge_3, the lattice parameters of Ta_5Si_3 are smaller (**Table A1.1)**, which is due to the smaller Si atomic radius. Atomic distances between the Ta and Si/Ge atoms, obtained from the single crystal refinements, are listed in **Table A1.4**. There are short Si2−Si2 and Ge2−Ge2 bonds indicative of the dimer formation, on the other hand, the Si1 and Ge1 atoms can be treated as isolated anions. Following the Zintl−Klemm formalism for valence compounds[145], an electronic formula for Ta_5Si_3 and Ta_5Ge_3 can be written as $(Ta^{3+})_5(T^{4-})(T_2^{6-})$ $(5e^-)$ (T = Si, Ge). This simple counting scheme suggests that the two phases should be metallic. We can also argue that the five

free electrons will populate the Ta *d* orbitals and thus participate in the Ta-Ta and Ta-*T* bonding.

Table A1.4. Interatomic distances in Ta_5Si_3 and Ta_5Ge_3. Number of bonds per unit cell is given in parentheses.

Ta_5Si_3		Ta_5Ge_3	
Atoms	Distance (Å)	Atoms	Distance (Å)
Si1-Ta1(×8)	2.7035(6)	Ge1-Ta1(×8)	2.7375(4)
Si1-Ta2(×2)	2.9650(6)	Ge1-Ta2(×2)	3.0058(6)
Si2-Si2(×1)	2.38(2)	Ge2-Ge2(×1)	2.543(3)
Si2-Ta1(×1)	2.605(7)	Ge2-Ta1(×1)	2.651(1)
Si2-Ta1(×4)	2.624(4)	Ge2- Ta1 (×4)	2.7013(8)
Si2-Ta2(×4)	2.555(4)	Ge2-Ta2(×1)	2.5677(7)

As mentioned in the Introduction, there are three possible structures for Ta_5Si_3 and Ta_5Ge_3 phases: Mn_5Si_3, W_5Si_3, and Cr_5B_3-type. However, the factors governing their stability have not been analyzed systematically. Based on the literature data[139,141], Mn_5Si_3-type structure may be stabilized by small impurity atoms, such as carbon or oxygen. More specifically, in 1956, H. Nowotny mentioned that the Mn_5Si_3-type Nd_5Ge_3 and Mo_5Si_3 could be stabilized by carbon[141]. Later, E. Parth*é et al.* reported that the W_5Si_3-type Ta_5Ge_3, prepared from the tantalum hydride and germanium, can be transformed into a Mn_5Si_3-type structure through addition of 5 at.% carbon[139]. On the

other hand, temperature was seen as a key for stabilizing the W_5Si_3- and Cr_5B_3-type structures in the absence of impurities. E.g. a W_5Si_3-type structure was obtained at high temperature, while a Cr_5B_3-type structure was observed at low temperatures for Nd_5Si_3 and $TaGe_{0.5}$[141]. The low and high temperature polymorphs of Ta_5Si_3 are Cr_5B_3-type and W_5Si_3-type, respectively, and the high to low temperature transformation was reported to occur at 2160 °C[137]. Since the temperature of arc-melting is very high and cooling rate is very fast during arc-melting, one can speculate that we should have been able to quench the high-temperature W_5Si_3-type structure of Ta_5Si_3 to room temperature. Provided that W_5Si_3-type structure indeed exists for Ta_5Si_3, it is likely that the W_5Si_3-type structure forms first and then it transforms to the Cr_5B_3-type one below 2160^{o}C. Unfortunately, our experiments could not verify or rebut such scenario. In case of Ta_5Ge_3, the sintering temperature of 1000^{o}C is relatively low, and likely the W_5Si_3-type polymorph exist at higher temperatures.

A1.3.2 Electronic Structures

Using the Zintl−Klemm formalism of $(Ta^{3+})_5(T^{4-})(T_2^{6-})$ $(5e^-)$ (T = Si, Ge), we can predict that the electron-rich Ta_5Si_3 and Ta_5Ge_3 should be metallic. However, this formalism ignores interactions between the cations and anions and between the cations themselves. In case of Ta_5Si_3 and Ta_5Ge_3 strong Ta-Si and Ta-Ta bonds are expected, also the full electron transfer from Ta to T (T = Si or Ge) will not occur, and thus the charge counting approach used above is not justifiable. Nevertheless in the electronic structure calculated, we expect to see features indicative of the $T2$-$T2$ dimer formation, and the

transition from the bonding to antibonding character should take place at more than 12 but less than 22 electrons per 3 *T* atoms since the Ta-to-*T* charge transfer is not complete.

The TB-LMTO-ASA calculations support the arguments presented above. The density of states (DOS) and crystal orbital Hamilton population (COHP) for Ta_5Si_3 and Ta_5Ge_3 are presented in **Figure A1.4**. There is strong resemblance between the electronic structures of Ta_5Si_3 and Ta_5Ge_3 and our DOS results are in agreement with those of Tao et al. who performed electronic structure calculations on Cr_5B_3-type Ta_5Si_3[146]. Significant hybridization between the Ta and *T* (*T* = Si or Ge) orbitals can be observed in the DOS curves. The Ta states are present at all the energies and become dominant above -4 eV. The COHP analysis shows that the character of the *T*2-*T*2 bonds change from bonding to antibonding around -4 and -3.3 eV, which corresponds to 13.8 and 17.1 electrons per 3 Si and Ge atoms, respectively (the higher population of the Ge states is due both to the lower energy of the Ge *s* states and higher energy of the bonding-to-antibonding transition). The contribution of the *T*2-*T*2 bonds to the overall bonding is rather weak, which is due to the low number of the *T*2-*T*2 bonds in the unit cell. Remarkably, in Ta_5Si_3 and Ta_5Ge_3 there is a pseudogap just below the Fermi level, and the Ta-Ta and Ta-Si bonds become antibonding in this energy range. Clearly, the electronic structure calculations suggest that the bonding in the Cr_5Si_3-type Ta_5Si_3 and Ta_5Ge_3 is close to being optimized.

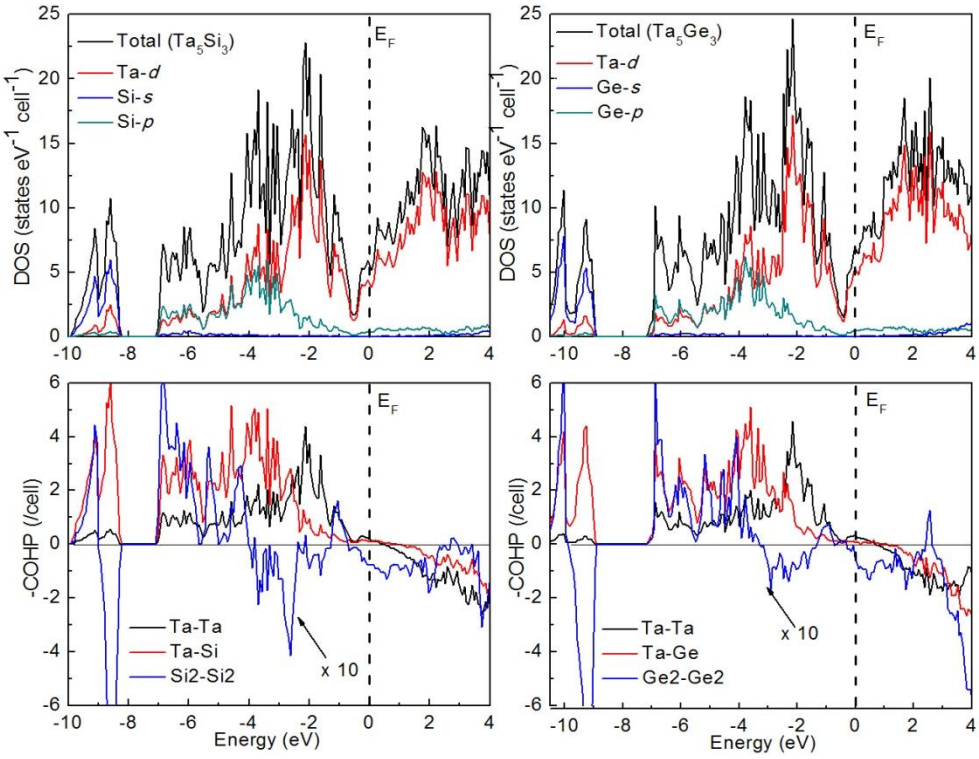

Figure A1.4. Density of States (DOS) and Crystal Orbital Hamilton Population (COHP) for Ta_5Si_3 (left) and Ta_5Ge_3 (right).

A1.3.3 Magnetic Properties of Ta_5Si_3 and Ta_5Ge_3

Since the Cr_5B_3-type Ta_5Si_3 and Ta_5Ge_3 contain no magnetic active elements, a Pauli-paramagnetic response can be predicted. Since the magnetic signals of Ta_5Si_3 and Ta_5Ge_3 were weak, the samples with the mass of 100 mg and magnetic field of 1 T were used for the measurement. The Pauli paramagnetism of Ta_5Si_3 is confirmed by the *M*-*T* data in **Figure A1.5**. However, the Ta_5Ge_3 shows a more complex behavior with three distinct regions: (1) a steep increase in *M* below 50K; (2) almost temperature-independent behaviour between 100 and 250K; (3) a decrease with temperature in *M* above 250K. While the first point can be attributed to the presence of identified paramagnetic impurity,

the last point suggests changes in the filling of the "up" and "down" spin subbands with temperature. Potentially, all three regions can be attributed to the variable filling of the spin subbands with temperature. While small Ta impurity were identified in Cr_5B_3-type Ta_5Ge_3, we doubt that it has any noticeable effect on the magnetic behaviour of Ta_5Ge_3.The mid-temperature magnetic data on Ta_5Ge_3 agree with those published by Kolotun et al[147].

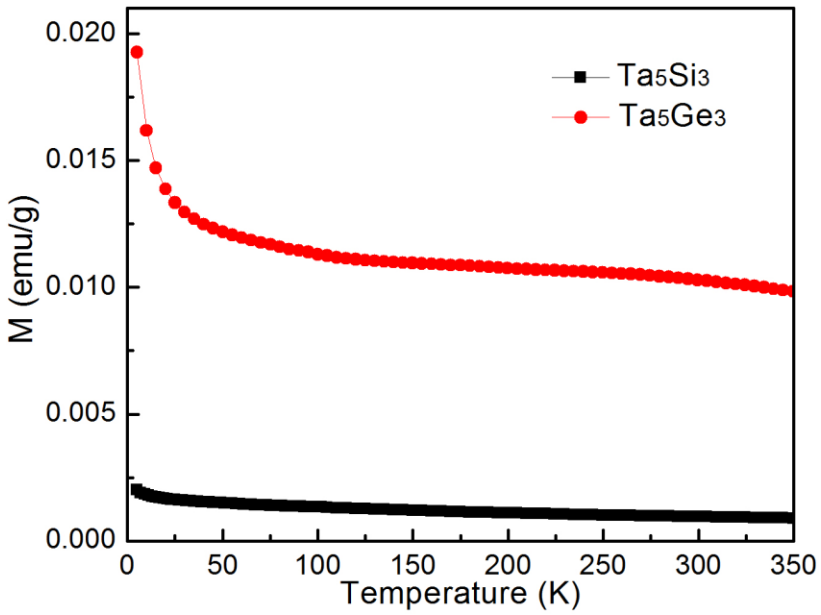

Figure A1.5. Magnetization vs. temperature for Ta_5Si_3 and Ta_5Ge_3.

A1.3.4 Electrical Resistivity

The metallic behavior of Ta_5Si_3 and Ta_5Ge_3 were previously reported by Neshpor et al. and Bondarev et al., respectively[148,149]. In our study, electrical resistivity measured on the PPMS for Ta_5Si_3 and Ta_5Ge_3 samples exhibited small values at the temperature

between 2 to 300 K. Firstly, a positive temperature coefficient was observed in **Figure A1.6**. Therefore, we can deduce that Cr_5B_3-type Ta_5Si_3 and Ta_5Ge_3 phases are metallic, which agrees with the LMTO calculations. Secondly, the resistivity of Ta_5Si_3 is always higher than that of Ta_5Ge_3. Lastly, the resistivity of the Ta_5Si_3 and Ta_5Ge_3 samples is almost constant between 2 and 20K, which can be attributed to the impurity scattering. In 1976, Cruceanu et al. reported the superconductivity in Mn_5Si_3-type Ta_5Si_3 with a transition temperature of 2.10K and a decrease in the resistivity was observed below 12 K[150]. We saw no indication of the superconductivity in our Ta_5Si_3 sample till 2K and thus could not verify this finding.

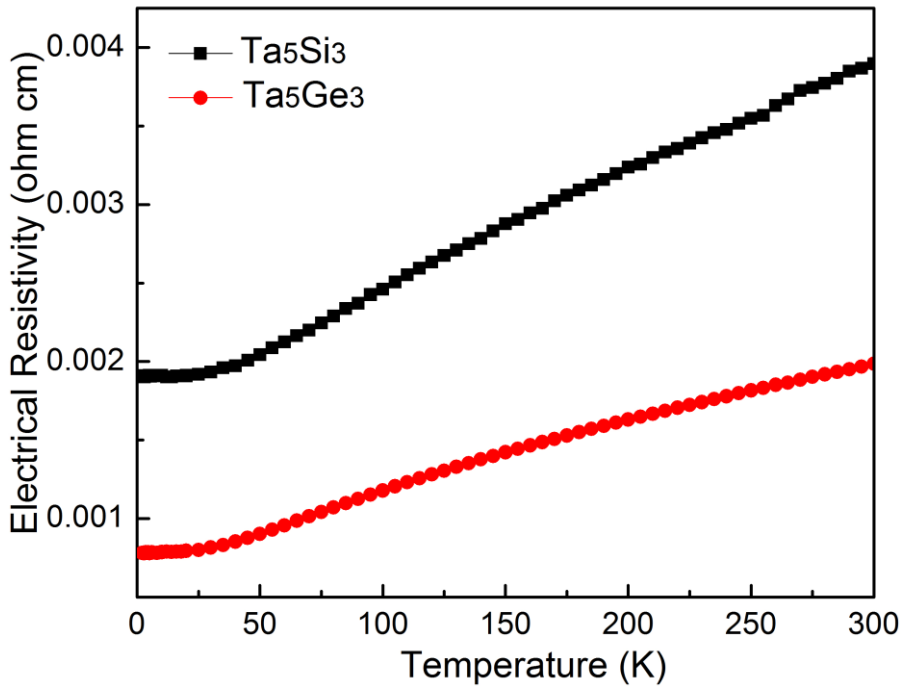

Figure A1.6. Electrical resistivity of the Ta_5Si_3 and Ta_5Ge_3 samples.

A1.4 Conclusions

The Cr_5B_3-type Ta_5Si_3 and Ta_5Ge_3 phases can be prepared by arc-melting and sintering at 1000°C, respectively. As discussed in this work, temperature appears to be a key factor in stabilization of the TM_5T_3 structures (*TM* = transition metals, *T* = Si, Ge). According to the magnetization data, the Ta_5Si_3 phase is a Pauli paramagnet while the Ta_5Ge_3 phase shows a more complex paramagnetic behavior. The Ta_5Si_3 and Ta_5Ge_3 phases are both metallic with a positive temperature coefficient in the temperature range from 20 to 300K.

Appendix 2. A Neutron Diffraction Study on the Site Preference of Co/Ga and Magnetic Properties of the Hexagonal $Ho(Co_{0.667}Ga_{0.333})_2$ and $Er(Co_{0.667}Ga_{0.333})_2$ Laves Phases

This chapter contains the material covered in the manuscript "A Neutron Diffraction Study on the Site Preference of Co/Ga and Magnetic Properties of the Hexagonal $Ho(Co_{0.667}Ga_{0.333})_2$ and $Er(Co_{0.667}Ga_{0.333})_2$ Laves Phases", which is currently unpublished, but will be submitted to a peer reviewed scientific journal. The synthetic experiments, structure determinations, electronic structure calsulations, and writing of the manuscript were accomplished by the candidate. Dr. Chad Boyer collected the neutron powder diffraction data. Neutron data interpretations were completed with the assiatnce of Dr. John E. Greedan.

RE($Co_{0.667}Ga_{0.333}$)$_2$ (*RE* = Ho, Er) were characterized by neutron powder diffraction (NPD). Rietveld refinement of the NPD data at 280K confirms the hexagonal $MnZn_2$-type structure, in accordance with the previous XRD results. Co/Ga occupancies on the 2*a* and 6*h* sites were refined to be 0.46/0.54(2) and 0.74/0.26(2), respectively, indicating a preference of Ga for the 2*a* site and of Co for the 6*h* site. This contrasts with the case of iso-structural *RE*CoAl for which no site preferences were found. Both materials are ferromagnetic with moments only on the *RE* site. Co moments were refined to ~ 0 within 2σ. The Er moments are parallel to the *c* axis and refined to be 6.07(8) μ_B at 3.5K, while the Ho moments have components along both the *a* and *c* axes with a refined value of 6.3(1) μ_B at 3.5K. Compared with the free ion values, both Er and Ho moments are much reduced, which could be attributed to crystal field effects. In addition, the Ho moment angle with the *c* axis is roughly constant just below T_C to ~25K but bends away with decreasing temperature to an angle of 44(1)^o at 3.5K. Magnetic small angle neutron scattering (SANS) was observed over a Q-range from 0.14Å^{-1} to 0.50 Å^{-1} in both samples. The integrated SANS of the Er phase peaks near T_C = 18.5K, then decreases monotonically with decreasing temperature, which is typical for a simple ferromagnet. On the other hand, the integrated SANS for the Ho phase exhibits a weak peak around T_C ~ 31K, followed by a plateau to 25K and a strong increase with decreasing temperatures, which tracks the evolution of the Ho moment angle with the *c* axis. These Curie temperatures are different from those estimated from bulk magnetization data, ~ 15K for Er and ~ 36K for Ho.

A2.1 Introduction

The *RE*Co_2 (*RE* = rare earth) compounds have been well studied.[56,151–154] While all *RE*Co_2 adopt the same cubic $MgCu_2$-type structure, their magnetic properties are quite different with regard to the rare-earth elements. A novel type of short-range order, an exchange enhanced paramagnetism, has been identified in nonmagnetic $ScCo_2$, YCo_2, and $LuCo_2$, while a long-range magnetic order is found in *RE*Co_2 with magnetic rare-earth elements.[155] In the latter case, the Co sublattice is driven into a ferromagnetic state by an *f-d* exchange field and the moment in the ordered state is between 0.8 and 1 μ_B. The light *RE*Co_2 phases are ferromagneic with the Co and *RE* sublattice coupled parallel. On the other hand, the heavy *RE*Co_2 phases are best characterized as ferrimagnetic wherein the *RE* moments couple anti-parallel to the Co moments.[7] The magnetic phase transition for at least some members of the series, *RE* = Dy, Ho and Er, is apparently first order and thus, these have been evaluated recently as potential magneto-caloric materials.[55,56] Therefore, the heavy *RE*Co_2-based phases have been attracting increasing attention.

While the *RE*Co_2 materials adopt the cubic ($Fd\bar{3}m$) Laves structure, substitution of Ga for Co induces the formation of the hexagonal ($P6_3/mmc$) $MgZn_2$-type structure in the *RE*$(Co_{0.667}Ga_{0.333})_2$ series.[chapter 4: Structural and Magnetic Studies on the New Laves Phases *RE*$(Co_{0.667}Ga_{0.333})_2$ (*RE* = Gd, Tb, Dy, Ho, and Er). Magnetocaloric effect of Gd$(Co_{0.667}Ga_{0.333})_2$] All studied *RE*$(Co_{0.667}Ga_{0.333})_2$ (*RE* = Gd, Tb, Dy, Ho and Er) phases show a long-range order but the Curie temperatures are reduced by a factor of ~2.5 from the parent *RE*Co_2 phases.[56] (**Figure A2.1**) Apparent ferromagnetic behaviour is observed for *RE* = Gd, Tb and Dy, whose Weiss temperature/Curie temperature ratios are near unity,

which is typical for ferromagnets. Also, the effective magnetic moments, μ_{eff} were equal to the *RE* only values, suggesting zero contribution from the Co/Ga sublattice in the paramagnetic region. Exceptions to this trend occur for *RE* = Ho and Er, whose Weiss temperature/Curie temperature ratios are 0.66 and -0.65, respectively (the Weiss temperature is negative for Er). As well, μ_{eff} values exceeded those for the *RE* ions only, suggesting a non-zero Co/Ga contribution and the possibility of a moment on that sublattice.

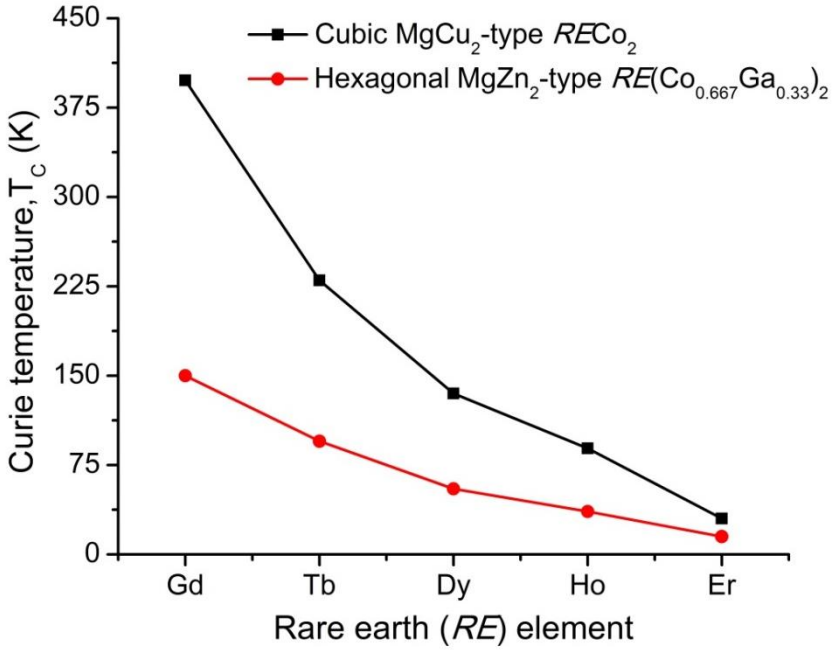

Figure A2.1. The Curie temperature of cubic *RE*Co_2 and hexagonal *RE*$(Co_{0.667}Ga_{0.333})_2$ (*RE* = Gd, Tb, Dy, Ho, and Er).

There are two Co/Ga sites in the $MgZn_2$-type structure, and the Co/Ga occupancies, could not be refined due to their similar X-ray atomic scattering factors. On the other hand, there are significant difference between the neutron scattering length, *b*, of Co (*b* = 2.49 fm) and Ga (*b* = 7.29 fm), and thus they are readily distinguished by neutron

diffraction.[156] In this work, neutron powder diffraction (NPD) was used to determine the magnetic structures and the magnetic moments at each site of the hexagonal $MgZn_2$-type $RE(Co_{0.667}Ga_{0.333})_2$ (*RE* = Ho, Er) phases and the Co/Ga occupancies.

A2.2 Experimental Section

A2.2.1 Synthesis

The starting materials of $RE(Co_{0.667}Ga_{0.333})_2$ (*RE* = Ho, and Er) phases are *RE* (99.9 wt.%, distilled grade, Metal Rare Earth Limited, China), Co (99.98 wt.%, Alfa Aesar), and Ga (99.999 wt.%, Alfa Aesar) pieces. The $RE(Co_{0.667}Ga_{0.333})_2$ alloys with a total mass of ~3 g were arc-melted 3 times to ensure homogeneity. During re-melting process, the samples were turned over as fast as possible to prevent sample cracking during cooling. The cast $RE(Co_{0.667}Ga_{0.333})_2$ (*RE* = Ho, and Er) alloys were wrapped in Ta foil, sealed in evacuated silica tubes, heated to 1000^{o}C at 100^{o}C/hour in the box furnaces and annealed for 72 hours before being quenched in cold water.

A2.2.2 Neutron Powder Diffraction

Neutron powder diffraction was performed on the C2 diffractometer at the Canadian Neutron Beam Centre at Chalk River, Ontario. The samples of ~2 g were mounted in a cylindrical vanadium container with a top-loading closed-cycle refrigerator. The data were collected using the neutron beams with a wavelength of 2.369 (1) Å at 3.5 K, 280K, and other temperatures between 3.5K and Curie temperature (T_C) for 2θ = 3.0-83.1°, and with a wavelength of 1.327 (1) Å at 3.5K and 280K for 2θ = 36.9-117.0°. The

2θ step size was 0.1° for all the data collection. The FullProf program [157] was used to refine the crystal and magnetic structures.

A2.2.3 Electronic Band Structure Calculatons

To study the band structure of hexagonal $MgZn_2$-type $Er(Co_{0.667}Ga_{0.333})_2$ phase and understand the absence of Co moments, tight-binding, linear-muffin tin orbital calculations with the atomic sphere approximation[142] (TB-LMTO-ASA) as implemented in the Stuttgart program[70] were used. The lattice parameters and atomic coordinates were taken from the previous single crystal X-ray refinements. All 4*f* electrons were treated as core electrons. Exchange and correlation were treated by the local density approximation (LDA).[71] A scalar relativistic approximation[73] was used to account for all relativistic effects except spin-orbit coupling. According to the atomic sphere approximation (ASA), overlapping Wigner-Seitz (WS) cells were constructed with radii making the overlapping potential to be the best approximation to the full potential. To satisfy the overlap criteria of the TB-LMTO-ASA model, space-filling empty spheres were included in the unit cell by the automatic sphere generation[74]. The basis set included 6*s*, 6*p* and 5*d* orbitals for Er, 3*d* orbitals for Co, 3*s* and 3*p* orbitals for Ga.

A2.3 Results and Discussion

A2.3.1 Crystal Structure

Rietveld refinement of the neutron powder diffraction data of $RE(Co_{0.667}Ga_{0.333})_2$ (*RE* = Ho, and Er) are consistent with the $MgZn_2$-type structure, in agreement with the

previous X-ray diffraction results. (**Table A2.1**) There are three crystallographic sites in the hexagonal $MgZn_2$-type structure: 2*a*, 4*f* and 6*h*. The *RE* atoms occupied the 4*f* site, while Co/Ga are distributed over 2*a* and 6*h* sites but their occupancies could not be previously refined due to their similar X-ray atomic scattering factors (Z_{Co} = 27 and Z_{Ga} = 31). However neutron scattering length, *b* = 2.49 fm for Co and 7.29 fm for Ga, provide significant contrast.[156] Herein, the Co/Ga occupancies were refined employing the neutron powder diffraction with a wavelength of 1.327(1) Å at 280K.

Table A2.1. Unit cell parameters of the $MgZn_2$-type $RE(Co_{0.667}Ga_{0.333})_2$ phases (*RE* = Ho and Er, XRD and NPD were collected at room temperature and 280K, respectively).

Annealed sample	Measurement method	Wavelength, Å	Structure	a, Å	c, Å
$Ho(Co_{0.667}Ga_{0.333})_2$	XRD	1.5406(1)	$MgZn_2$-type	5.2064(1)	8.4228(1)
$Ho(Co_{0.667}Ga_{0.333})_2$	NPD	1.327 (1)	$MgZn_2$-type	5.2027(3)	8.4248(7)
$Ho(Co_{0.667}Ga_{0.333})_2$	NPD	2.369 (1)	$MgZn_2$-type	5.2048(6)	8.429(1)
$Er(Co_{0.667}Ga_{0.333})_2$	XRD	1.5406(1)	$MgZn_2$-type	5.1851(1)	8.4115(1)
$Er(Co_{0.667}Ga_{0.333})_2$	NPD	1.327 (1)	$MgZn_2$-type	5.1853(4)	8.4159(9)
$Er(Co_{0.667}Ga_{0.333})_2$	NPD	2.369 (1)	$MgZn_2$-type	5.1871(6)	8.418(1)

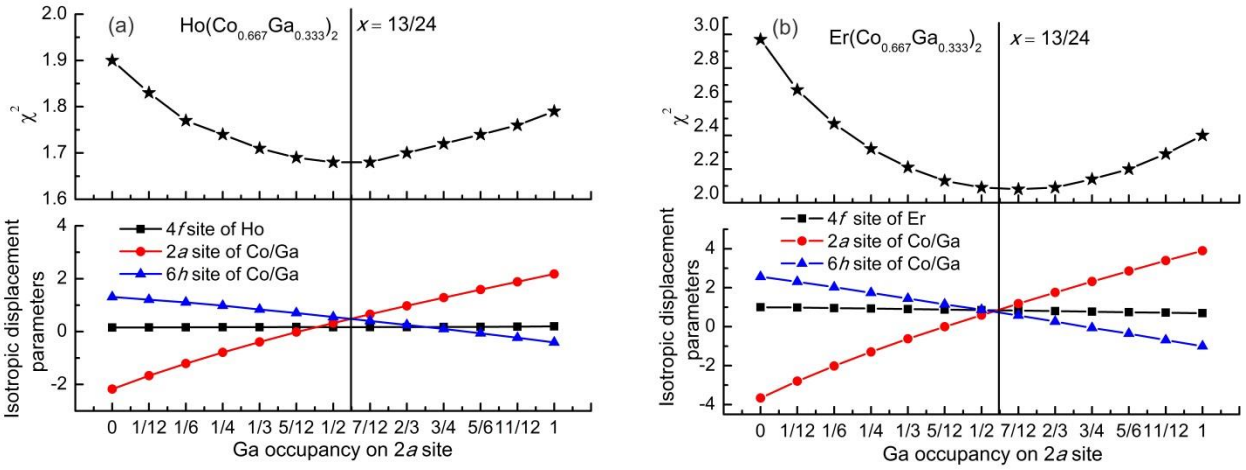

Figure A2.2. Refinement of Co/Ga occupancy based on χ^2: a) $Ho(Co_{0.667}Ga_{0.333})_2$, b) $Er(Co_{0.667}Ga_{0.333})_2$.

Due to strong correlations, the site occupancy and displacement parameter were not refined simultaneously. Instead, displacement parameters for the three sites were varied for a set of fixed occupancies for the 2*a* and 6*h* sites, which spanned the full range of possibilities. The results for both materials in terms of the Ga fraction, *x*, of the 2*a* site are shown in **Figure A2.2.** The χ^2 value is minimized when the isotropic displacement parameters on the 2*a* and 6*h* sites are roughly equal. At the point of intersection, *x* is about 13/24, i.e. Ga occupies 13/24 (0.54) of the 2*a* sites, while the remaining 11/24 (0.46) fraction is taken by Co. Because the total Co/Ga ratio is 2, the Co and Ga occupancies on 6*h* sites are 53/72 (0.74) and 19/72 (0.26), respectively. (**Table A2.2**) Note that the results are essentially the same for Ho and Er and that, while Co and Ga occupy the 2*a* site at roughly the same rate, Co has a ~ 3/1 preference for the 6*h* site.

Although Ga and Al belong to the same main group and have identical atomic size (r_{Co} = 1.25 Å and r_{Ga} = 1.26 Å),[109] the site occupancy in the pseudobinary *RE*Co_2-*RE*Ga_2

systems is different from that in the pseudobinary *RE*Co_2-*RE*Al_2 systems. Er$(Co_{1-x}Al_x)_2$ pseudobinary phases have a random distribution of Co and Al on the 2*a* and 6*h* sites at lower Al concentration, i.e. $x \leq 0.5$. When $x > 0.5$, Co seems to occupy 2*a* sites exclusively, and Al and Co coexist on 6*h* site.[104] Co content is twice of Ga content in *RE*$(Co_{0.667}Ga_{0.333})_2$ (*RE* = Ho, and Er), however, Co prefers the 6*h* site, while Ga slightly the 2*a* site. Compared with the random distribution (ratio Co/Ga = 0.667/0.333 = 2), the Co/Ga ratio is smaller on the 2*a* site (~1) and larger on the 6*h* sites (~3).

Table A2.2. Atomic coordinates and isotropic displacement parameters (B_{eq}) for annealed *RE*$(Co_{0.667}Ga_{0.333})_2$ (*RE* = Er, and Ho).

Atom	Site	Occupancy	x/*a*	y/*b*	z/*c*	B_{eq} (Å^2)
			Ho$(Co_{0.667}Ga_{0.333})_2$			
Ho1	4*f*	1	1/3	2/3	0.0631(4)	0.17(9)
Co1/Ga11	2a	0.46/0.54(2)	0	0	0	0.5(1)
Co2/Ga22	6*h*	0.74/0.26(2)	0.830(2)	0.660(3)	1/4	0.5(1)
			Er$(Co_{0.667}Ga_{0.333})_2$			
Er1	4*f*	1	1/3	2/3	0.0626(1)	0.8(1)
Co1/Ga11	2a	0.46/0.54(2)	0	0	0	0.9(2)
Co2/Ga22	6*h*	0.74/0.26(2)	0.828(2)	0.657(5)	1/4	0.7(1)

A2.3.2 Magnetic Structures

Selected neutron diffraction data are shown in **Figure A2.3a and A2.3b** for *RE*$(Co_{0.667}Ga_{0.333})_2$ (*RE* = Er, and Ho) at the base temperature of the cryostat, 3.5K, and at temperatures just above the estimated Curie temperatures**.** There are at least two features to note. First, the 3.5K data contain several new reflections of significant intensity,

indicating that they are magnetic in origin. Secondly, there is very strong scattering below 10 degrees which can be assigned as magnetic small angle neutron scattering (SANS). As shown later, no such low angle scattering exists in the 280K data.

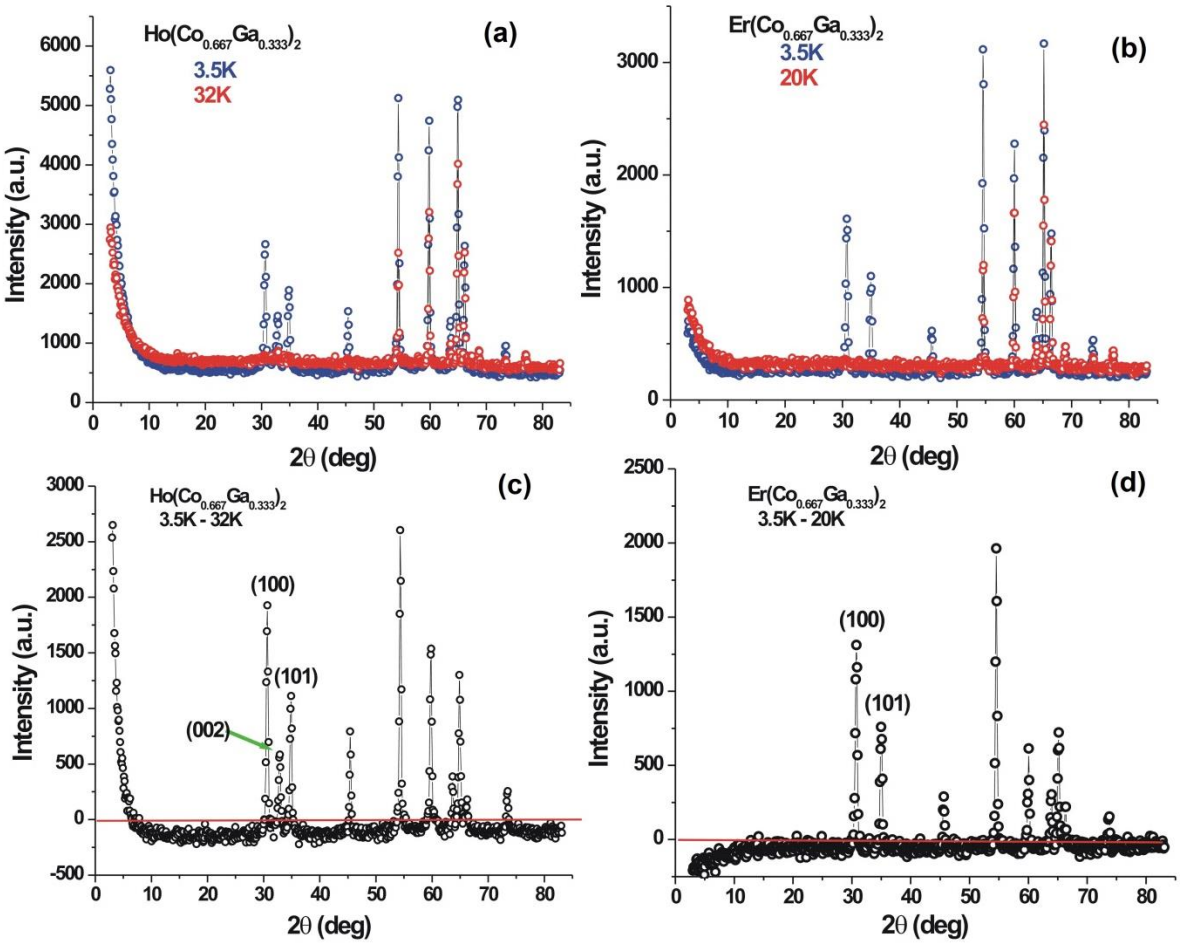

Figure A2.3. (a) Comparison of neutron diffraction (ND) patterns for $Ho(Co_{0.667}Ga_{0.333})_2$ at 32K (red) and 3.5K (blue). **(b)** Comparison of ND patterns for $Er(Co_{0.667}Ga_{0.333})_2$ at 20K (red) and 3.5K (blue). **(c)** Difference ND pattern (3.5K – 32K) with some low angle peaks indexed for $Ho(Co_{0.667}Ga_{0.333})_2$. **(d)** Difference ND pattern (3.5K – 20K) with some low angle peaks indexed for $Er(Co_{0.667}Ga_{0.333})_2$. In all cases λ = 2.369(1) Å.

In **Figure A2.3c** and **A2.3d**, differences between the intesnsities at 3.5K and higher temperatures isolate the magnetic reflections. Some of the low angle reflections,

which provide information regarding the direction of the magnetic moments, are indexed. For the Ho phase there are three such peaks, (100), (002) and (101), while in the Er case, the (002) is absent. Clearly, the ordering wave vector is $\boldsymbol{k}$ = (0, 0, 0) for both. **Figure A2.4** shows the simulation of NPD patterns for $Ho(Co_{0.667}Ga_{0.333})_2$ with an ordered moment of 8 μ_B and a ferromagnetic model, F_z or $F_{x,y.}$ As verified by the simulations in **Figure A2.4**, the $Er(Co_{0.667}Ga_{0.333})_2$ moment must be parallel to the *c* axis, while the $Ho(Co_{0.667}Ga_{0.333})_2$ moment likely has components in both the *ab* plane and along the *c* axis. The agreement between the observed and simulated NPD patterns with ferromagnetic models strongly suggest ferromagnetic ground states for $RE(Co_{0.667}Ga_{0.333})_2$ (*RE* = Er, and Ho).

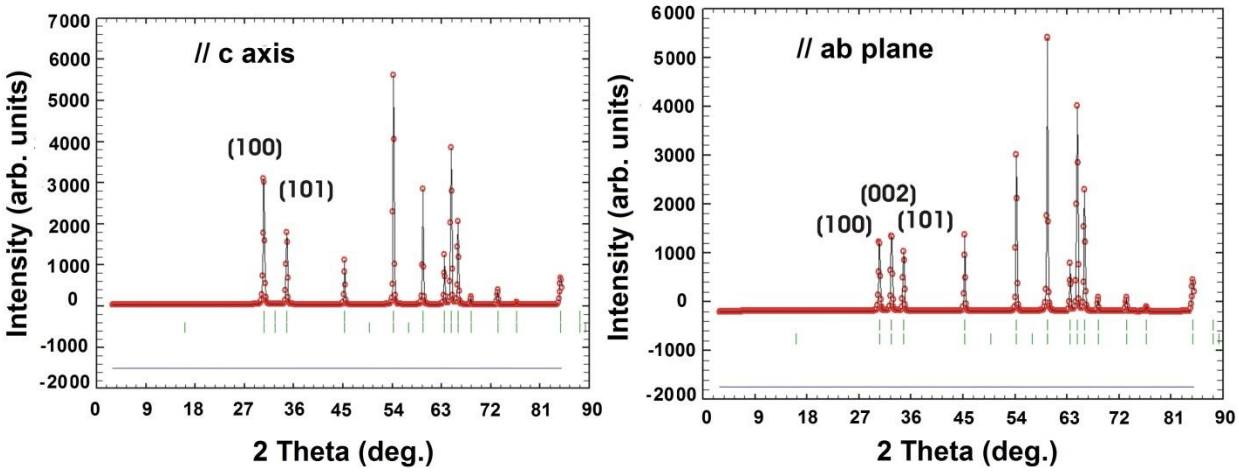

Figure A2.4. Simulation of powder neutron diffractions patterns for $Ho(Co_{0.667}Ga_{0.333})_2$ with an ordered moment of 8 μ_B and a ferromagnetic model, F_z or $F_{x,y}$. **(left)** M_{Ho} // *c* axis, and **(right)** $M_{Ho} \perp c$ axis.

A2.3.3 $Er(Co_{0.667}Ga_{0.333})_2$

The magnetic structure of $Er(Co_{0.667}Ga_{0.333})_2$ was refined at 3.5K using the data from both wavelengths. Initially, a F_z model for the Er moments with no contribution

from the Co/Ga lattice was refined. The results are shown in **Figure A2.5** and **Table A2.3**. The Er moment is indeed along the *c* axis and its refined value is 6.24(9) and 6.07(8) μ_B for λ = 1.327(1) Å and λ = 2.369(1) Å, respectively. This is significantly reduced from the free ion value of $g_J J$ = 9 μ_B expected for Er^{3+}, indicating that crystal field effects are important in $Er(Co_{0.667}Ga_{0.333})_2$. A model with moments on both the 2*a* and 6*h* sites and antiparallel to the Er moment on the 4*f* site was also refined. There was no change in the agreement indices, χ^2 or R_{mag}, and the moments on the Co/Ga sites were refined to 0.12(6) μ_B, which is in fact 0 within 2σ. The Er moment was reduced to 5.8(1) μ_B, which is within 3σ from the value obtained by excluding any Co contribution. The conclusion is that there is no compelling evidence for a moment on the Co/Ga sites in this material. This is in contrast to the situation for $ErCo_2$, where a Co moment is ~ 1 μ_B[158].

Table A2.3. Results of the various magnetic structure refinements at 3.5K for $Er(Co_{0.667}Ga_{0.333})_2$.

parameter	λ = 1.327(1) Å	λ = 2.369(1) Å
lattice parameter *a* (Å)	5.1720(2)	5.1756(2)
lattice parameter *c* (Å)	8.3798(5)	8.3847(4)
$M_T(\mu_B)$	6.24(9)	6.07(8)
R(Bragg); *R*(F)	7.21; 5.64	3.81; 4.26
R(Mag)	7.15	2.54
R(p); *R*(wp); *R*(exp); χ^2	4.16; 5.34; 3.89; 1.89	4.73; 6.15; 5.43; 1.28

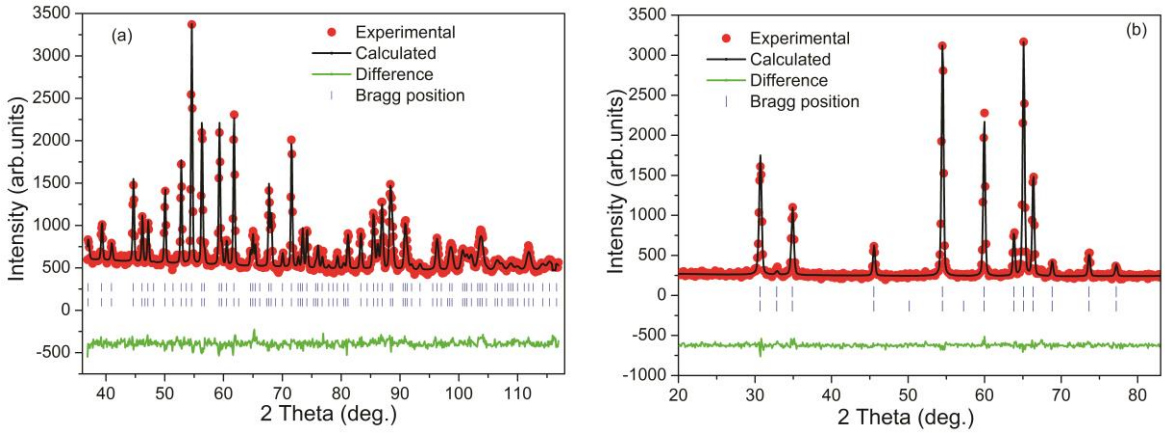

Figure A2.5. Rietveld refinement of NPD data for $Er(Co_{0.667}Ga_{0.333})_2$ at 3.5K with a F_z model for the Er moments and zero moment on the Co/Ga sites. (a) λ = 1.327(1) Å. (b) λ = 2.369(1) Å. Details are given in Table 3.

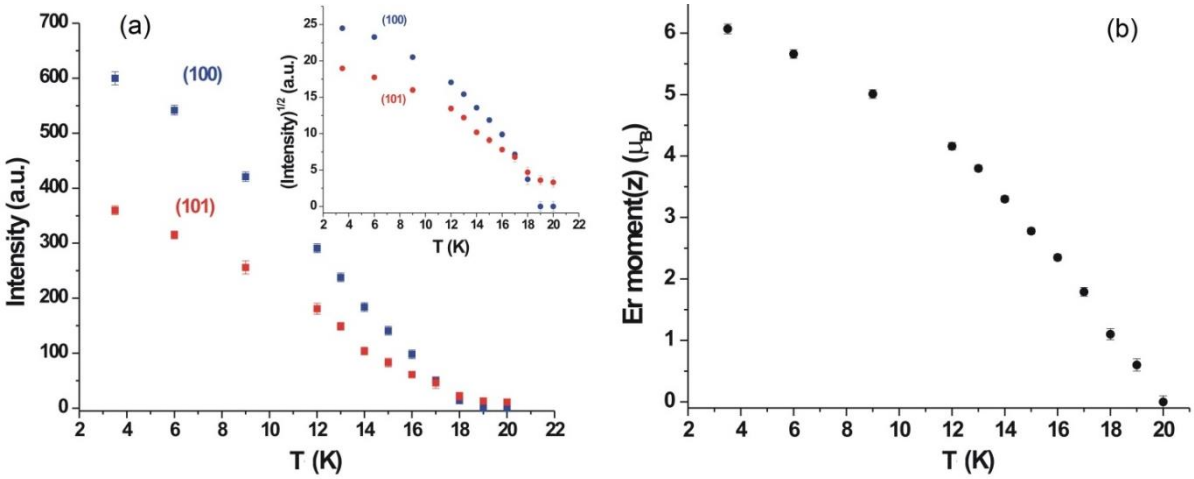

Figure A2.6. (a) The temperature variation of the intensities of the (100) and (101) magnetic reflections and the $(intensity)^{1/2}$ (inset) and **(b)** the refined Er moment for $Er(Co_{0.667}Ga_{0.333})_2$.

NPD patterns were also obtained using the λ = 2.369(1) Å wavelength for several temperatures and the Er moment was refined within the F_z model. The results are shown

in **Figure A2.6b** along with the observed intensities for the (100) and (101) magnetic reflections of **Figure A2.6a**. Note the very gradual decrease in the intensities (**Figure A2.6a**) and ordered moment (**Figure A2.6b**) up to T_C~18.5K, which is 23% higher than T_C of 15K estimated from the magnetization data. There are uncertainties in the determination of T_C from **Figure A2.6**. First, both "magnetic" reflections, (100) and (101), have small structural components, that for the latter are somewhat greater than for the former. Secondly, the magnetic component builds rather slowly with decreasing temperature. The (100) reflections is not detectable above 18K while the (101) reflection attains a small but constant value. This is best seen from the inset, **Figure A2.6a**, which shows the (Intensity)$^{1/2}$ for both reflections. While a small Er moment is refined at 19K, this may result from difficulties in accounting for the weak structural contributions to these reflections. For example, *R*(Mag) at 19K is 47% while it is 2.5% at 3.5K and 16% at 17K. Thus, an assignment of T_C = 18.5K appears to be the best choice, given the quality of the refinement at 19K. Finally, the very gradual temperature variation of the moment suggests a large value for the critical exponent, β, in $M(Er)/M(Er)_{sat} = \{[T_C - T]/T_C\}^{\beta}$. Although there are insufficient data to determine β properly, an estimate was made using data from 18K to 13K. The fit yielded β = 0.51(2) with T_C = 18.5K, which is consistent with the mean field theory (MFT) value of 1/2. (**Figure A2.7**). The fact that the MFT appears to hold is in turn consistent with an exchange coupling mechanism such as RKKY that extends over several sets of neighbors in direct space.[2,1,3]

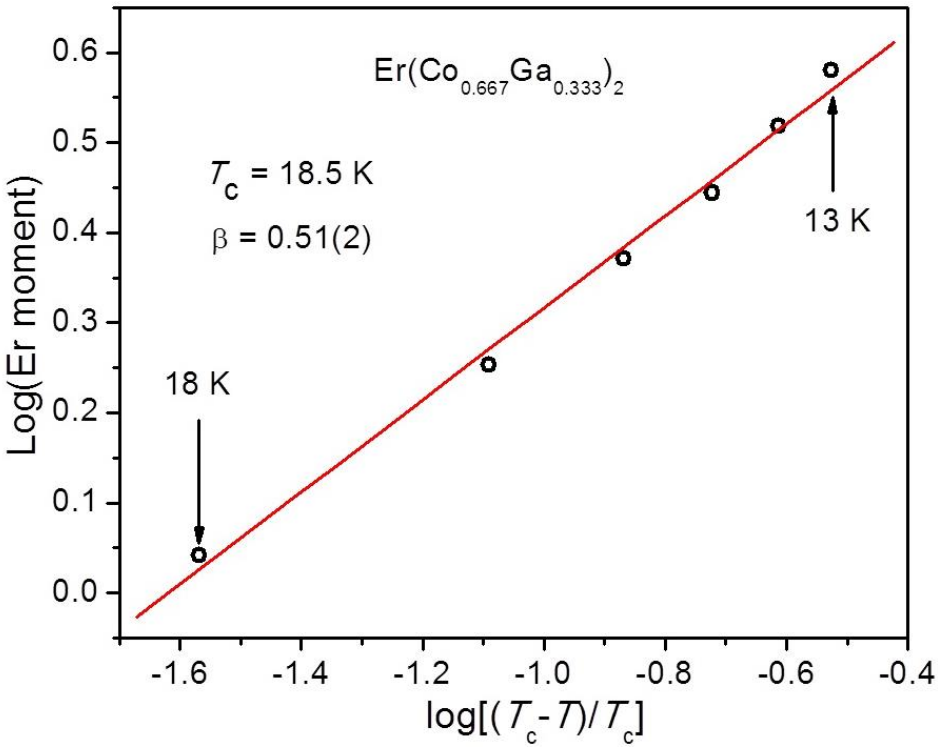

Figure A2.7. The relationship between Log[(T_C –T)/T_C] and Log(Er moment), where β is the critical exponent and equals the slop of the integrated line (red).

A2.3.4 $Ho(Co_{0.667}Ga_{0.333})_2$

Figure A2.8 shows the refinement of neutron diffraction pattern for $Ho(Co_{0.667}Ga_{0.333})_2$ at 3.5K using the data from both wavelengths and the results are listed in **Table A2.4**. The initial model involved components of the Ho moment in the *ab* plane and along the *c* axis, i.e. an F_{xz} configuration. At 3.5K the Ho moment components were refined as M_z = 4.6(1) μ_B and M_x = 4.4(1) μ_B yielding a total Ho moment of 6.3(1) μ_B for λ = 2.369(1) Å. Thus, the Ho moment is tilted 44(1)^o from the *c* axis. As with the Er material, inclusion of moments on the Co/Ga sites did not improve the agreement indices and the Co moments were refined to 0.3(1) μ_B, i.e. ~ 0 within 2σ and there was no change

in the Ho moment, 6.3(1) μ_B. For λ = 1.327(1) Å, the refined magnetic moments are slightly higher than those values for λ = 2.369(1) Å, i.e. M_x = 4.4(2) μ_B, M_z = 4.8(2) μ_B, and M_T = 6.45((9) μ_B. The Ho moment is much reduced from the free ion value of 10 μ_B due to the quenching effects of the crystal field, similar to the case for Er.

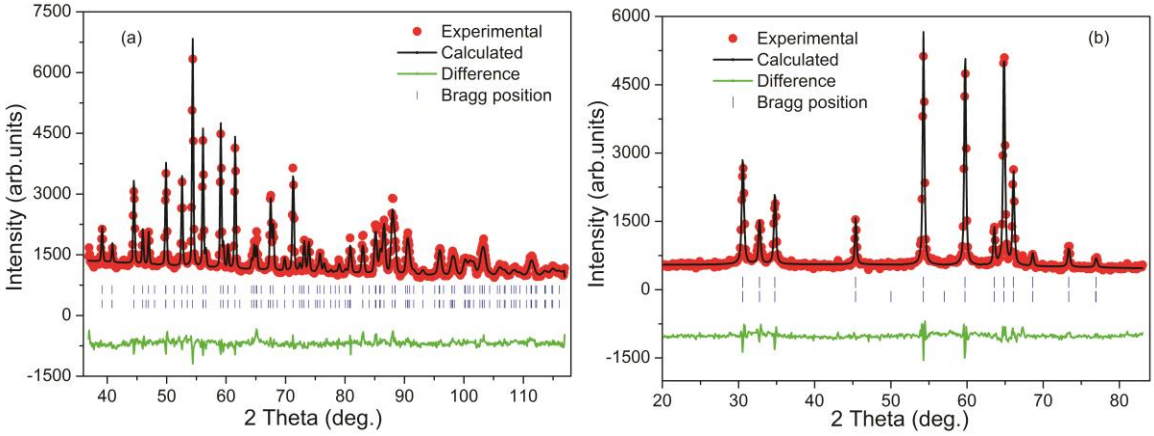

Figure A2.8. Rietveld refinement of NPD data for $Ho(Co_{0.667}Ga_{0.333})_2$ at 3.5K with a F_{xz} model for the Ho moments and zero moment on the Co/Ga sites. **(a)** λ = 1.327(1) Å. **(b)** λ = 2.369(1) Å. Details are given in Table 4.

Table A2.4. Results of the various magnetic structure refinements at 3.5K for $Ho(Co_{0.667}Ga_{0.333})_2$

parameter	λ = 1.327(1) Å	λ = 2.369(1) Å
lattice parameter *a* (Å)	5.1912(2)	5.1950(3)
lattice parameter *c* (Å)	8.4011(5)	8.4085(6)
M_x; M_z (μ_B)	4.4(2); 4.8(2)	4.4(1); 4.6(1)
M_T (μ_B)	6.45((9)	6.3(1)
R(Bragg); *R*(F)	8.10; 5.30	5.98; 5.14
R(Mag)	9.00	7.69
R(p); *R*(wp); *R*(exp); χ^2	3.92; 4.94; 2.68; 3.38	5.68; 7.20; 3.74; 3.71

The temperature variation of the intensities (*I*) of the magnetic reflections (100), (002) and (101), the refined magnetic components, M_x and M_z, and the total Ho moment,

M_T, along with its angle with respect to the *c* axis are all displayed in **Figure A2.9**. Note first in **A2.9a**, from the temperature dependence of the purely magnetic (100) and (101) peaks, that the apparent T_C is 31K, 14% smaller than T_C of 36K, estimated from the magnetization data. The (002) reflection has a clear structural component and *I*(002) does not change within error between 25K and 40K, but increases sharply below 25K. As the magnetic component of (002) tracks the bending of the total Ho moment away from the c axis, it is clear that Ho_{tot} is parallel to the *c* axis from 29K to 25K, but tilts significantly during further cooling to 3.5K. This is reflected in the behavior of the refined components, M_x and M_z (**Figure A2.9b**), and the inset shows the temperature variation of the tilt angle, which reaches $44(1)^o$ at 3.5K as mentioned previously. The value of the tilt angle equals $\tan^{-1}(M_x/M_z)$. As can be seen from 9b, the errors on M_x are quite large just below T_C = 31K. As M_x is largely determined by the relative intensities of *I*(002) with respect to *I*(100) and *I*(101), there may again be difficulties in separating the structural and magnetic contributions associated with (002) during the refinement, thus the large uncertainties in the angle just below T_C. However, reasonable uncertainties are reached by 25K-27K and it is fair to conclude that the data are consistent with a tilt angle of ~ $24(3)^o$ which remains constant from 25K to near T_C. This feature is important in the interpretation of the SANS data to be discussed in the next section, however, given the issues discussed above, the actual angle is best determined from magnetization measurements on a single crystal. Finally, the difference in magnetic anisotropy between Ho^{3+} and Er^{3+} in this axial crystal system is consistent with observations in other axial materials, for example in the *RE*Co_5

series, *P*6/*mmm*, $ErCo_5$ has easy *c* axis anisotropy while for $HoCo_5$ the Ho moment is 50^o from the *c* axis at 4.2K.[159,160]

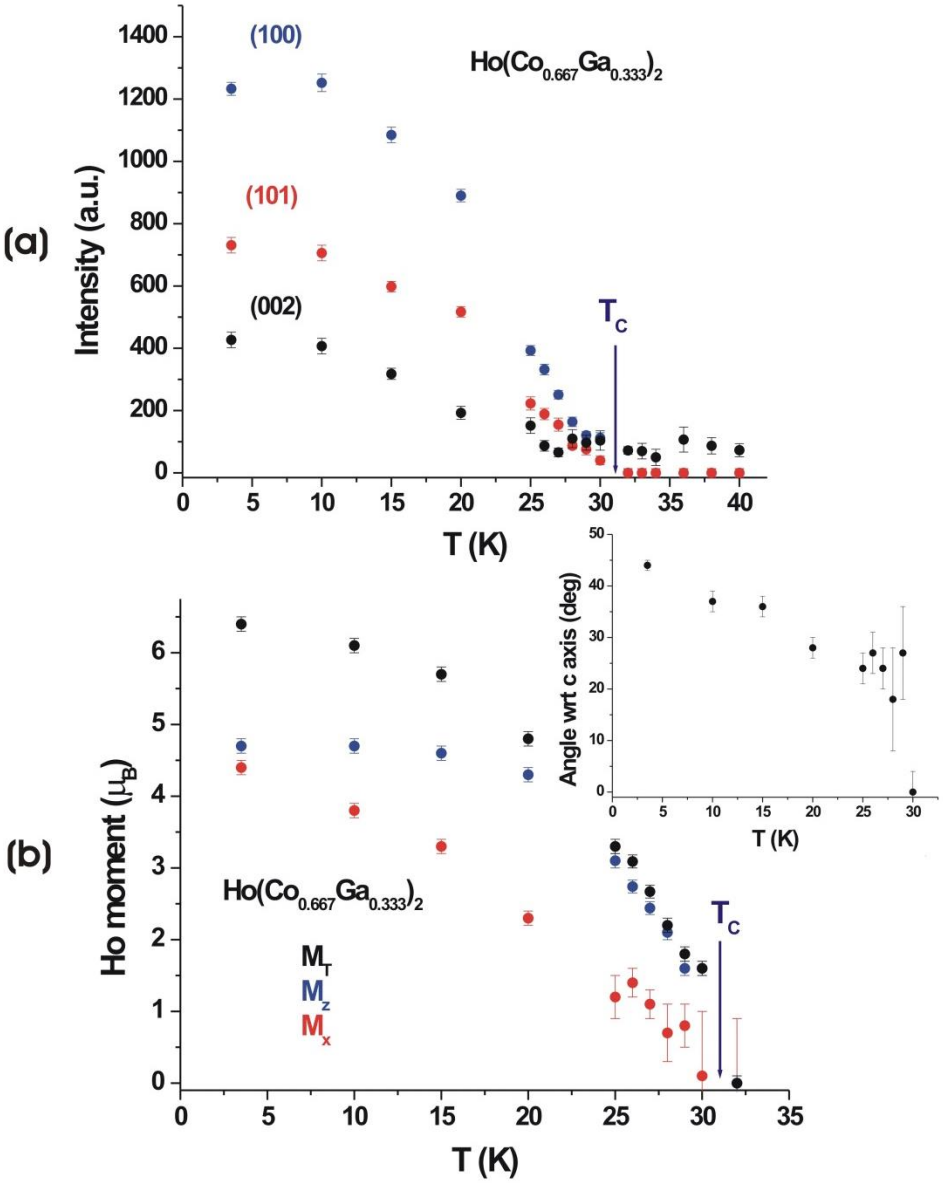

Figure A2.9. (a) The temperature variation of the intensities of the (100), (002) and (101) magnetic reflections and **(b)** the refined Ho_x (M_x), Ho_z (M_z) and Ho_{total} (M_T) moments for $Ho(Co_{0.667}Ga_{0.333})_2$ and **(inset)** the angle made by the Ho moment with respect to the *c* axis.

A2.3.5 Magnetic Small Angle Neutron Scattering (SANS)

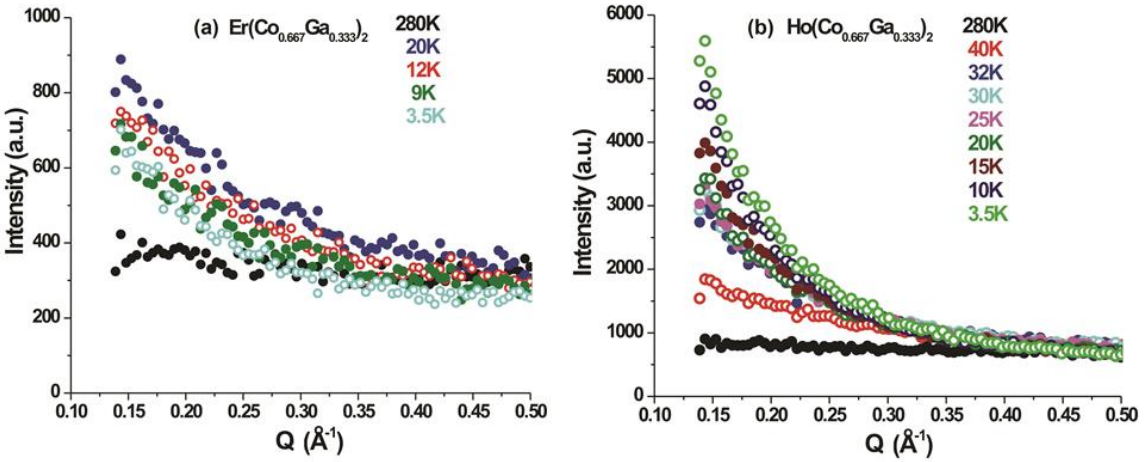

Figure A2.10. Magnetic SANS data at selected temperatures for **(a)** $Er(Co_{0.667}Ga_{0.333})_2$ and **(b)** $Ho(Co_{0.667}Ga_{0.333})_2$. The data are not scaled to the counting times actually used.

Somewhat by accident, magnetic SANS data are also available for both materials (**Figure A2.3**). Normally, magnetic SANS is seen only at very small Q(2θ) values, where $Q = 4/\lambda \sin\theta$, but the ordered moments on Ho and Er are so large that it can be seen easily in our data which extend to Q = 0.14 $Å^{-1}$. Magnetic SANS is a feature of ferromagnets as there is a very strong peak in the magnetic scattering at Q(2θ) = 0. A detailed view is provided in **Figure A2.10** for both materials. Note that the scattering at 280 K is flat in this Q-range, which confirms the magnetic origin of the signals near T_C for both materials. Note a surprising feature of the data, namely, that for the $Ho(Co_{0.667}Ga_{0.333})_2$ phase, the SANS signal increases with decreasing temperature, opposite to the case for Er material. The counting time for data collection of $Ho(Co_{0.667}Ga_{0.333})_2$ and $Er(Co_{0.667}Ga_{0.333})_2$ phase is 3.5 and 4 hours respectively, and 1.4 grams versus 2.1 grams with regard to weight. If

the data are scaled to the counting times and weight actually used, the SANS signal for the former is significantly greater than for the latter.

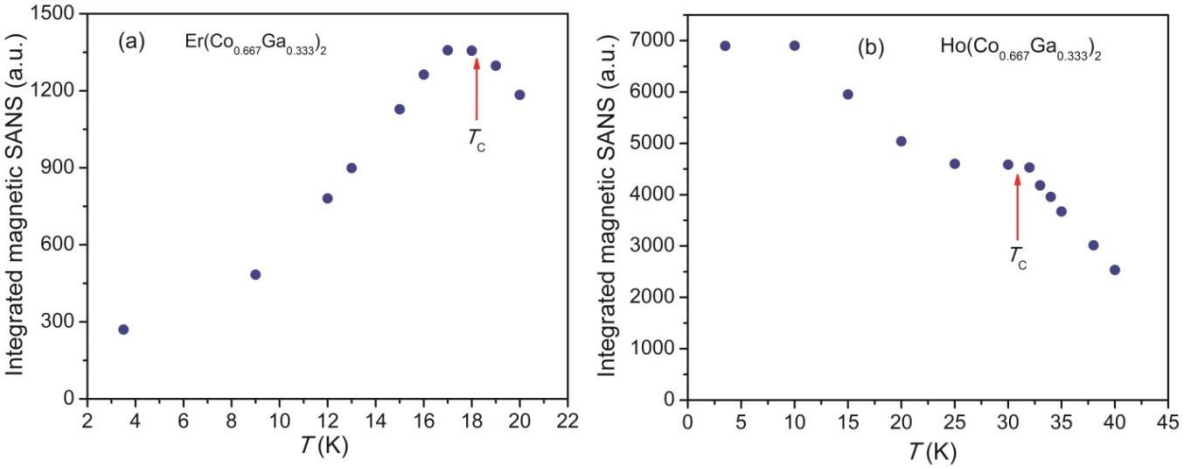

Figure A2.11. The temperature dependence of the integrated magnetic SANS data over the range (0.14 $Å^{-1}$ < Q < 0.50 $Å^{-1}$) for $Er(Co_{0.667}Ga_{0.333})_2$ **(a)** and $Ho(Co_{0.667}Ga_{0.333})_2$ **(b)**. T_C for both materials is indicated.

The magnetic component of the SANS signal (MagSANS) is acquired by subtraction of the 280K contribution and integration over the Q range (0.14$Å^{-1}$ < Q < 0.50 $Å^{-1}$) indicated for each temperature. The temperature dependence of the MagSANS obtained in this manner is displayed in **Figure A2.11**. The very different behavior of the MagSANS component for the two materials is now clearly evident.

The results for $Er(Co_{0.667}Ga_{0.333})_2$ (**Figure A2.11a**) are those expected for a simple ferromagnet, for which there are no changes in magnetic structure, MagSANS peaks near T_C and then gradually decrease as the ferromagnetic clusters grow in size and pass out of the SANS window. This is consistent with the strong *c* axis anisotropy for the $Er(Co_{0.667}Ga_{0.333})_2$ phase, which does not change with decreasing temperature. On the

other hand, the behavior of the Ho MagSANS (**Figure A2.11b**) is quite remarkable, showing a weak peak at T_C, followed by a plateau and then by a strong increase leading to another plateau below 10K. This profile tracks roughly the variation of the Ho moment angle with respect to the *c* axis, **Figure A2.9b**, and suggests an explanation for the anomalous behavior, i.e the magnetic structure just below T_C to ~ 25K involves a constant Ho tilt angle, giving rise to the SANS plateau, but below 25K the angle changes continuously during cooling inducing an increasing SANS signal.

A2.3.6 The Absence of Co Magnetic Moments

The absence of Co magnetic moments in *RE*$(Co_{0.667}Ga_{0.333})_2$ contrasts with the case of the cubic Laves *RE*Co_2 phases, where Co magnetic moment was refined to be ca. 1 μ_B in $HoCo_2$ and $ErCo_2$. In an attempt to understand the absence of the Co magnetic moments in *RE*$(Co_{0.667}Ga_{0.333})_2$, the electronic structure was calculated at the LMTO level with no spin polarization or correlation effects included for *RE* = Er. As the observed Co/Ga distribution cannot be handled within LMTO program, the Ga atoms were assigned to the 2*a* sites and Co atoms the 6*h* sites, i.e. for a *RE*$(Co_{0.75}Ga_{0.25})_2$ composition, which is not too distant from that observed. Additionally, Co has a clear preference for the 6*h* sites. As seen in **Figure A2.12**, the majority of the Co *d* states are below the Fermi level, E_F, while the Ga states, particularly the *p* states, and the Er *d* states are well above. Such a distribution is expected due to the much lower energy of the Co *d* orbitals as compared to those of the Ga 4*p* orbitals[161,162] and Er 5*d* orbitals. As well, the Co *d* orbitals will be more localized than the Ga 4*p* states. As a result, the Co *d* states are almost fully

occupied, E_F falls at a very low density of states (DOS) and the magnetic moment, originating from the *d* electrons, is expected to be relatively small or non-existent. Given that the actual Ga concentration is greater and the Co concentration is smaller than calculated, the Co d-states are likely to be filled to a greater extent than shown in **Figure A2.12**. This situation is consistent with a very small, perhaps zero, Co moment as derived from the neutron scattering.

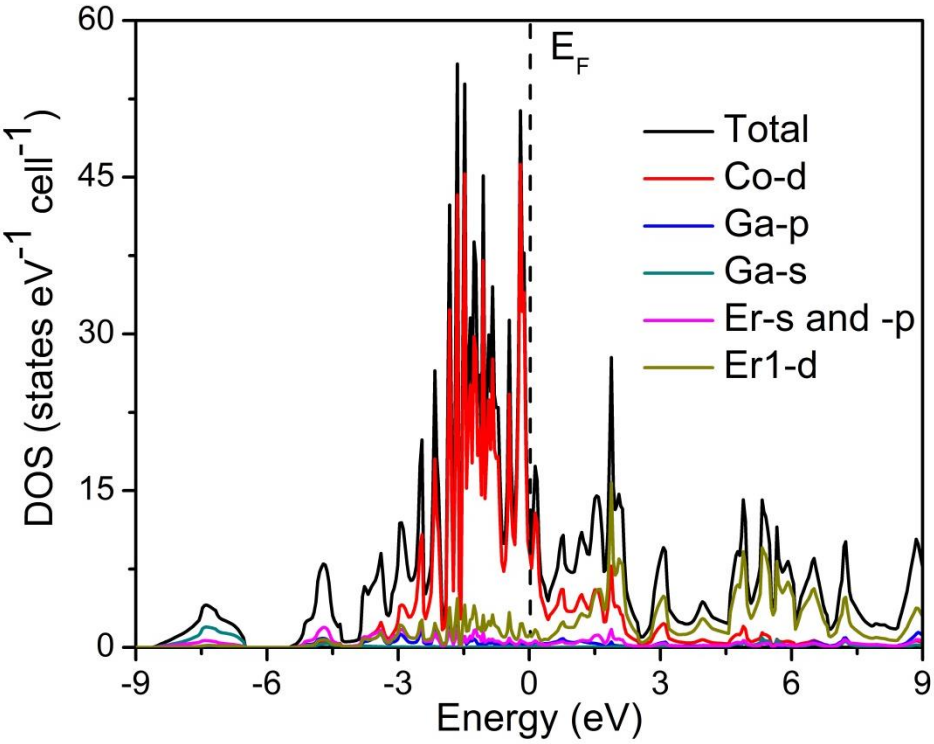

Figure A2.12. Density of states (DOS) for $Er(Co_{0.75}Ga_{0.25})_2$.

A2.4 Conclusions

Variable temperature NPD were collected to clarify the Co/Ga distribution over the 2*a* and 6*h* site and the ground magnetic state of $RE(Co_{0.667}Ga_{0.333})_2$ (*RE* = Ho, and Er).

Co and Ga occupy the 2*a* site in roughly the same proportion, while Co has a much higher preference, ~ 3/1, for the 6*h* site. Both materials order ferromagneticly and the Curie temperatures are 31 and 18.5K for Ho and Er, respectively, which differ from those inferred from magnetization data, 36K (Ho) and 15K (Er). At 3.5K, the Co magnetic moments are ~ zero in both materials, and the Er, 6.07(1)μ_B, and Ho, 6.3(1)μ_B, magnetic moments are much smaller than the free ion values, 9 and 10μ_B, respectively, due to crystal field effects. The Er moments are parallel to the *c* axis and there is no change in the magnetic structure as temperature decreases. On the other hand, the Ho moment angle with respect to the *c* axis remains constant between near T_C and 25K but tilt away during cooling, and reach an angle of 44(1)^o at 3.5K. Magnetic small angle neutron scattering peaks near T_C for Er($Co_{0.667}Ga_{0.333}$)$_2$ and decreases smoothly with decreasing temperature, behavior typical for a ferromagnet with no change in magnetic structure, while for Ho($Co_{0.667}Ga_{0.333}$)$_2$ it increases to a plateau from T_C to 25K and then increases further during cooling, which tracks the observed change in the Ho tilting angle.

Reference

(1) Kasuya, T. *Prog. Theor. Phys.* **1956**, *16*, 45–57.

(2) Ruderman, M. A.; Kittel, C. *Phys. Rev.* **1954**, *96*, 99–102.

(3) Yosida, K. *Phys. Rev.* **1957**, *106*, 893–898.

(4) De Gennes, P. G. *J. Phys. Radium* **1962**, *23*, 510–521.

(5) Chol-Lyong, J.; Lei, X.; Ding, D.; Yuan-Da, D.; Gracien, E. *J. Alloys Compd.* **2008**, *458*, 18–21.

(6) Phan, M.-H.; Yu, S.-C. *J. Magn. Magn. Mater.* **2007**, *308*, 325–340.

(7) Franco, V.; Blázquez, J. S.; Ingale, B.; Conde, A. *Annu. Rev. Mater. Res.* **2012**, *42*, 305–342.

(8) Warburg, E. *Ann. Phys.* **1881**, *13*, 141.

(9) Zimm, C. J.; Sternberg, A.; Pecharsky, V. K.; Gschneidner Jr., K. A.; Osborne, M.; Anderson, I. *Adv. Cryog. Eng.* **1998**, *43*, 1759–1766.

(10) Miller, G. J. *Chem. Soc. Rev.* **2006**, *35*, 799–813.

(11) Tegus, O.; Brück, E.; Buschow, K. H. J.; de Boer, F. R. *Nature* **2002**, *415*, 150–152.

(12) Pecharsky, V. K.; Gschneidner Jr., K. . *Phys. Rev. Lett.* **1997**, *78*, 4494–4497.

(13) Trung, N. T.; Zhang, L.; Caron, L.; Buschow, K. H. J.; Brück, E. *Appl. Phys. Lett.* **2010**, *96*, 172504.

(14) Li, Z.; Zhang, Y.; Sánchez-Valdés, C. F.; Sánchez Llamazares, J. L.; Esling, C.; Zhao, X.; Zuo, L. *Appl. Phys. Lett.* **2014**, *104*, 44101.

(15) Du, J.; Cui, W. B.; Zhang, Q.; Ma, S.; Xiong, D. K.; Zhang, Z. D. *Appl. Phys. Lett.* **2007**, *90*, 42510.

(16) von Ranke, P. J.; de Oliveira, N. a.; Plaza, E. J. R.; de Sousa, V. S. R.; Alho, B. P.; Carvalho, a. M. G.; Gama, S.; Reis, M. S. *J. Appl. Phys.* **2008**, *104*, 93906.

(17) Mozharivskyj, Y.; Choe, W.; Pecharsky, A. O.; Miller, G. J. *J. Am. Chem. Soc.* **2003**, 15183–15190.

(18) Svitlyk, V.; Mozharivskyj, Y.; Miller, G. J. *J. Am. Chem. Soc.* **2009**, *131*, 2367–2374.

(19) Pecharsky, a O.; Gschneidner, K. a.; Pecharsky, V. K.; Schindler, C. E. *J. Alloys Compd.* **2002**, *338*, 126–135.

(20) Mozharivskyj, Y.; Alexandra, O. T.; Miller, G. J. *Zeitschrift für Krist.* **2006**, *221*, 493–501.

(21) Svitlyk, V.; Campbell, B. J.; Mozharivskyj, Y. *Inorg. Chem.* **2009**, *48*, 10364–10370.

(22) Svitlyk, V.; Cheung, Y. Y. J.; Mozharivskyj, Y. *J. Magn. Magn. Mater.* **2010**, *322*, 2558–2566.

(23) Hu, F. X.; Shen, B. G.; Sun, J. R.; Zhang, X. X. *Chin. Phys.* **2000**, *9*, 550–553.

(24) Hu, F. X.; Shen, B. G.; Sun, J. R.; Cheng, Z. H.; Rao, G. H.; Zhang, X. X. *Appl. Phys. Lett.* **2001**, *78*, 3675–3677.

(25) Miller, G. J. *Chem. Soc. Rev.* **2006**, *35*, 799–813.

(26) Fujita, A.; Akamatsu, Y.; Fukamichi, K. *J. Appl. Phys.* **1999**, *85*, 4756.

(27) Shen, B. G.; Sun, J. R.; Hu, F. X.; Zhang, H. W.; Cheng, Z. H. *Adv. Mater.* **2009**, *21*, 4545–4564.

(28) Wang, G. jun; Wang, F.; Di, N. li; Shen, B. gen; Cheng, Z. hua. *J. Magn. Magn. Mater.* **2006**, *303*, 84–91.

(29) Wen, G. H.; Zheng, R. K.; Zhang, X. X.; Wang, W. H.; Chen, J. L.; Wu, G. H. *J. Appl. Phys.* **2002**, *91*, 8537.

(30) Pecharsky, V. K.; Gschneidner Jr., K. A.; Tsokol, A. O. *Reports Prog. Phys.* **2005**, *68*, 1479–1539.

(31) Hu, F. X.; Ilyn, M.; Tishin, A. M.; Sun, J. R.; Wang, G. J.; Chen, Y. F.; Wang, F.; Cheng, Z. H.; Shen, B. G. *J. Appl. Phys.* **2003**, *93*, 5503–5506.

(32) Shen, B.-G.; Hu, F.-X.; Dong, Q.-Y.; Sun, J.-R. *Chinese Phys. B* **2013**, *22*, 17502.

(33) Chen, Y.; Chen, Y.; Wang, F.; Shen, B.; Hu, F.; Sun, J.; Wang, G.; Cheng, Z. *J. Phys. Condens. Matter* **2003**, *15*, L161–L167.

(34) Palstra, T. T. M.; Mydosh, J. A.; Nieuwenhuys, G. J.; van der Kraan, A. M.; Buschow, K. H. J. *J. Magn. Magn. Mater.* **1983**, *36*, 290–296.

(35) Hu, F. X. PhD Thesis, Chinese Academy of Sciences, 2002.

(36) Ouladdiaf, B.; Ziebeck, K. R. A. *J. Phys. Condens. Matter* **2002**, *14*, 10159–10171.

(37) Hu, F.; Shen, B.; Sun, J. *Appl. Phys. Lett.* **2000**, *76*, 3460.

(38) Hu, F.; Shen, B.; Sun, J.; Wu, G. *Phys. Rev. B* **2001**, *64*, 132412.

(39) Ingale, B.; Gopalan, R.; Raja, M. M.; Chandrasekaran, V.; Ram, S. *J. Appl. Phys.* **2007**, *102*, 22–27.

(40) Wada, H.; Tanabe, Y. *Appl. Phys. Lett.* **2001**, *79*, 3302.

(41) Wada, H.; Taniguchi, K.; Tanabe, Y. *Mater. Trans.* **2002**, *43*, 73–77.

(42) Wada, H.; Morikawa, T.; Taniguchi, K.; Shibata, T.; Yamada, Y.; Akishige, Y. *Phys. B* **2003**, *328*, 114–116.

(43) Tegus, O.; Bruck, E.; Zhang, L.; Dagula; Buschow, K. H. J.; De Boer, F. R. *Phys. B* **2002**, *319*, 174–192.

(44) Gschneider Jr., K. A.; Pecharsky, V. K.; Tsokol, A. O. *Reports Prog. Phys.* **2005**, *68*, 1479–1539.

(45) Brück, E.; Tegus, O.; Li, X. W.; de Boer, F. R.; Buschow, K. H. J. *Phys. B* **2003**, *327*, 431–437.

(46) Gribanov, I. F.; Golovchan, A. V.; Varyukhin, D. V.; Val'kov, V. I.; Kamenev, V. I.; Sivachenko, A. P.; Mityuk, V. I.; Sidorov, S. L. *Low Temp. Phys.* **2009**, *35*, 786–791.

(47) Budzyński, M.; Valkov, V. I.; Golovchan, A. V.; Mitsiuk, V. I.; Sivachenko, A. P.; Surowiec, Z.; Tkachenka, T. M. *Phys. B* **2014**, *452*, 37–41.

(48) Val'kov, V. I.; Golovchan, A. V.; Varyukhin, D. V.; Mitsiuk, V. I.; Ryzhkovskii, V. M. *J. Magn. Magn. Mater.* **2012**, *324*, 3043–3051.

(49) Cam Thanh, D. T.; Brück, E.; Tegus, O.; Klaasse, J. C. P.; Gortenmulder, T. J.; Buschow, K. H. J. *J. Appl. Phys.* **2006**, *99*, 08Q107.

(50) Cam Thanh, D. T.; Brück, E.; Trung, N. T.; Klaasse, J. C. P.; Buschow, K. H. J.; Ou, Z. Q.; Tegus, O.; Caron, L. *J. Appl. Phys.* **2008**, *103*, 07B318.

(51) Trung, N. T.; Ou, Z. Q.; Gortenmulder, T. J.; Tegus, O.; Bus chow, K. H. J.; Bruck, E. *Appl. Phys. Lett.* **2009**, *94*, 102513.

(52) Gutfleisch, O.; Willard, M. a; Brück, E.; Chen, C. H.; Sankar, S. G.; Liu, J. P. *Adv. Mater.* **2011**, *23*, 821–842.

(53) Stein, F.; Palm, M.; Sauthoff, G. *Intermetallics* **2004**, *12*, 713–720.

(54) Duc, N. H.; Kim Anh, D. T.; Brommer, P. E. *Phys. B* **2002**, *319*, 1–8.

(55) Duc, N. H.; Anh, D. T. K. *J. Magn. Magn. Mater.* **2002**, *242–245*, 873–875.

(56) Khmelevskyi, S.; Mohn, P. *J. Phys. Condens. Matter* **2000**, *12*, 9453–9464.

(57) de Oliveira, N. A.; von Ranke, P. J. *J. Magn. Magn. Mater.* **2003**, *264*, 55–61.

(58) de Oliveira, N. A.; von Ranke, P. J.; Troper, A. *Phys. Rev. B* **2004**, *69*, 64421.

(59) Wang, D. H.; Liu, H. D.; Tang, S. L.; Tang, T.; Wen, J. F.; Du, Y. W. *Solid State Commun.* **2002**, *121*, 199–202.

(60) Liu, H. D.; Wang, D. H.; Tang, S. L.; Cao, Q. Q.; Tang, T.; Gu, B. X.; Du, Y. W. *J. Alloys Compd.* **2002**, *346*, 314–319.

(61) Sichevich, O. M.; Gladyshevskii, R. E.; Hrin', Y. N.; YarMolyuk, Y. P. *Dopovidi Akad. Nauk Ukr. RSR, Seriya B Geol. Khimichni ta Biol. Nauk.* **1982**, *11*, 57–59.

(62) Liang, L.; Zeng, L.; Liu, S.; He, W. *Phys. B* **2013**, *426*, 35–39.

(63) Ouyang, Z. W.; Rao, G. H.; Yang, H. F.; Liu, W. F.; Liu, G. Y.; Feng, X. M.; Liang, J. K. *Phys. B* **2004**, *344*, 436–442.

(64) Zhao, J.-T.; Corbett, J. D. *J. Alloys Compd.* **1994**, *210*, 1–7.

(65) Pecharsky, V. K.; Zavalij, P. Y. *Fundamentals of Powder Diffraction and Structural Characterization of Materials*; 2nd ed.; Springer Science and Business Media Kluwer Academic: New York, 2009.

(66) *STOE & Cie GmbH, Darmstadt : Germany*; 2004.

(67) G.M. Sheldrick. *SHELXS-97 - Program for the Solution of Crystal Structures, University of Gottingen, Germany*; 1997.

(68) Hunter, B. A.; Howard, C. J. Australian Nuclear Science and Technology a Computer Program for Rietveld Analysis of X-Ray and Neutron, 2000, 27.

(69) Yuan, F.; Morozkin, A. V.; Mozharivskyj, Y. *J. Alloys Compd.* **2015**, *620*, 376–382.

(70) Jepsen, O.; Burkhardt, A.; Andersen, O. K. *The TB-LMTO-ASA Program*; 4.7.; Stuttgart, Germany, 1999.

(71) Andersen, O. K.; Jepsen, O. *Phys. Rev. Lett.* **1984**, *53*, 2571–2574.

(72) Gunnarsson, 0.; Lundqvist, B. I. *Phys. Rev. B* **1976**, *13*, 4274–4298.

(73) Andersen, O. K.; Jepsen, O.; Glotzel, D. In *Highlights of Condensed- Matter Theory*; Bassani, F.; Fumi, F.; Tosi, M. P., Eds.; 1985.

(74) Jepsen, O.; Andersen, O. K. *Phys. B Condens. Matter* **1995**, *97*, 35–47.

(75) Svitlyk, V.; Campbell, B. J.; Mozharivskyj, Y. *Inorg. Chem.* **2009**, *48*, 10364.

(76) Misra, S.; Mozharivskyj, Y.; Tsokol, A. O.; Schlagel, D. L.; Lograsso, T. A.; Miller, G. J. *J. Solid State Chem.* **2009**, *182*, 3031.

(77) Wu, L.; Kim, S.; Seo, D. *J. Am. Chem. Soc.* **2005**, *127*, 15682–15683.

(78) Cheung, Y. Y. J.; Svitlyk, V.; Mozharivskyj, Y. *Inorg. Chem.* **2012**, *51*, 10169–10175.

(79) Roger, J.; Yahia, M. B.; Babizhet'sky, V.; Bauer, J.; Cordier, S. *J. Solid State Chem.* **2006**, *179*, 2310.

(80) Canepa, F.; Cirafici, S.; Merlo, F.; palenzona, A. *J. Magn. Magn. Mater.* **1993**, *118*, 182.

(81) Tchernev, D. I.; Narasimhan, K. S. V. L.; Steinfink, H. *IEEE Trans. Magn.* **1969**, *5*, 222.

(82) Mayer, I.; Felner, I. *J. Less Common Met.* **1974**, *37*, 171.

(83) Palenzona, A.; Franceschi, E. *J. Less Common Met.* **1968**, *14*, 47.

(84) Cirafici, S.; Franceschi, d E. *J. Less Common Met.* **1979**, 66.

(85) Buschow, K. H. J.; Hoogenhof, W. W. v. d. *J. Less Common Met.* **1976**, *45*, 309–313.

(86) Yatsenko, S. P. *J. Chem. Phys.* **1977**, *74*, 836.

(87) Janson, K.; Schifer, H.; Weiss, A.; Naturforsch, Z. *Tl. B* **1966**, *21*, 287.

(88) KONGUETSOF, H.; YAKINTHOS, J. K. *phys. stat. sol.* **1982**, *69*, K157-161.

(89) Hunter, B. A.; Howard, C. J. Australia Nuclear Science and Technology. *Organization: Menai, Australia*, 2000.

(90) Lv, B.; Zhu, X. Y.; Lorenz, B.; Wei, F. Y.; Xue, Y. Y.; Yin, Z. P.; Kotilar, G.; Chu, C. W. *Phys. Rev. B* **2013**, *88*, 132520.

(91) Mozharivskyj, Y.; Franzen, H. F. *J. Solid State Chem.* **2000**, *152*, 478–485.

(92) Mozharivskyj, Y.; Franzen, H. F. **2001**, *327*, 78–81.

(93) Tkachuk, A. V; Bie, H.; Mar, A. *Intermetallics* **2008**, *16*, 1185.

(94) Verbovytsky, Y.; Latka, K. *J. Alloys Compd.* **2007**, *438*, L4.

(95) Hohnke, D.; Parthe, E. *J. Less Common Met.* **1969**, *17*, 291.

(96) Abdusalyamova, M. N.; Burnashev, O. R.; Mirono, K. Y. *J. Less Common Met.* **1986**, *125*, 1.

(97) Rieger, W.; Parthe, E. *Acta Crystallogr.* **1968**, *24*, 456.

(98) Liu, J.; Gottschall, T.; Skokov, K. P.; Moore, J. D.; Gutfleisch, O. *Nat. Mater.* **2012**, *11*, 620–626.

(99) Tishin, A. M. *Cryogenics (Guildf).* **1990**, *30*, 720–725.

(100) Hu, F. X.; Shen, B. G.; Sun, J. R. *Appl. Phys. Lett.* **2002**, *80*, 826–828.

(101) Oesterreicher, H.; Wallance, W. E. *J. Less Common Met.* **1967**, *13*, 91–102.

(102) Duc, N. H.; Goto, T. *Handbook on the Physics and Chemistry of Rare Earths*; Gschneidner Jr., K. A.; Eyring, L., Eds.; Elsevier B.V., 1999; Vol. 26.

(103) Yartys', V. A.; Bubyk, I. I. *Coord. Chem.* **1992**, *18*, 445–448.

(104) Oesterreicher, H. *J. Less-common Met.* **1973**, *33*, 25–41.

(105) Stein, F.; Palm, M.; Sauthoff, G. *Intermetallics* **2005**, *13*, 1056–1074.

(106) Eatough, N. L.; Tracy Hall, H. *Inorg. Chem.* **1972**, *11*, 2608–2609.

(107) Johannes, R. L.; Haydock, R.; Heine, V. *Phys. Rev. Lett.* **1976**, *36*, 372–376.

(108) Nei, J.; Young, K.; Salley, S. O.; Ng, K. Y. S. *Mater. Chem. Phys.* **2012**, *136*, 520–527.

(109) Pauling, L. C. *The Nature of the Chemical Bond and the Structure of Molecules and Crystals: An Introduction to Modern Structural Chemistry*; 3rd ed.; Cornell University Press: Ithaca, NY, 1960.

(110) Wallace, W. E. *Rare Earth Intermetallics*; ALPER, A. M.; Margrave, J. L.; Nowick, A. S., Eds.; first.; A subsidiary of Harcourt Brace Jovanovich: New York and London, 1973.

(111) Farrell, J.; Wallace, W. E. *Inorg. Chem.* **1966**, *5*, 105–109.

(112) Moon, R. M.; Koehler, W. C.; Farrell, J. *J. Appl. Phys.* **1965**, *36*, 978–979.

(113) Harris, I.; Mansey, R.; Raynor, G. *J. Less Common Met.* **1965**, *9*, 270–280.

(114) Talik, E.; Heimann, J.; Chelkowski, A. *J. Less-common Met.* **1986**, *124*, L13–L16.

(115) Andersen, O. K.; Pawlowska, Z.; Jepsen, O. *Phys. Rev. B* **1986**, *34*, 5253–5269.

(116) Koelling, D. D.; Harmon, B. N. *J. Phys. C Solid State Phys.* **1977**, *10*, 3107–3114.

(117) Dronskowski, R.; Blöchl, P. E. *J. Phys. Chem.* **1993**, *97*, 8617–8624.

(118) Kresse, G.; Furthmüller, J. *Phys. Rev. B* **1996**, *54*, 11169–11186.

(119) Kresse, G.; Furthmüller, J. *Comput. Mater. Sci.* **1996**, *6*, 15–50.

(120) Barandiaran, J. M.; Gignoux, D.; Rodriguez-Fernandez, J. *Phys. B Phys. Condens. Matter* **1989**, *154*, 293–299.

(121) Zegaou, B.; Benkhettou, N.; Rached, D.; Reshak, A. H.; Benalia, S. *Comput. Mater. Sci.* **2014**, *87*, 172–177.

(122) Saini, S. M.; Singh, N.; Nautiyal, T.; Auluck, S. *J. Phys. Condens. Matter* **2007**, *19*, 176203.

(123) Bonilla, C. M.; Paudyal, D.; Herrero-Albillos, J.; Pecharsky, V. K.; Gschneidner, K. A.; Garcia, L. M.; Bartolome, F. *IEEE Trans. Magn.* **2014**, *50*, 4–7.

(124) Buschow, K. H. J.; Hoogenhof, W. W. *J. Less Common Met.* **1976**, *45*, 309.

(125) Nesohor, V. S.; Samsonov, G. V. *Sov. Phys* **1961**, *5*, 877–880.

(126) Thom, A. J.; Summers, E.; Akinc, M. *Intermetallics* **2002**, *10*, 555–570.

(127) Meyer, M. K.; Akinc, M. J. *J. Am. Chem. Soc.* **1996**, *79*, 2763–2766.

(128) Brixner, L. H. *J. Inorg. Nucl. Chem.* **1963**, *25*, 257–260.

(129) Pietrokowaky, P.; Duwez, P. *J Mets* **1951**, *8*, 772.

(130) Bondarev, V. N.; Podergin, V. A.; Perminov, V. P. *Inorg. Mater.* **1968**, *4*, 1473–1476.

(131) Colinet, C.; Tedenac, J. C. *Intermetallics* **2010**, *18*, 1444–1454.

(132) Gladyshevskii, E. I.; Markiv, V. Y.; Efimov, V. Y.; Savitskii, E. M.; Baron, V. V. *Inorg. Mater.* **1965**, *1*, 1023–1027.

(133) Gottschlich, M.; Gourdon, O.; Persson, J.; Cruz, C. de la; Petricek, V.; Brueckel, T. J. *J. Mater. Chem.* **2012**, *22*, 15275–15284.

(134) Forsyth, J. B.; Brown, P. J. *J. Phys. Condens. Matter* **1990**, *2*, 2713–2720.

(135) Tillard, M. *J. Alloys Compd.* **2014**, *584*, 385–392.

(136) Parthe, E.; Lux, B.; Nowotny, H. *Monatshefte für Chemie* **1955**, *86*, 859–867.

(137) Kocherzhinskii, Y. A.; Kulik, O. G.; Shishkin, E. A. *Dokl. Chem.* **1981**, *261*, 464–465.

(138) Nowotny, H.; Lux, B.; Kudielka, H. *Monatshefte für Chemie* **1956**, *87*, 447–470.

(139) Parthé, E.; Norton, J. T. *Acta Crystallogr.* **1958**, *11*, 14–17.

(140) Jeitschko, W.; Nowotny, H.; Benesovsky, F. *Monatshefte für Chemie* **1963**, *94*, 844–850.

(141) Nowotny, H.; Searcy, A.; Orr, J. E. *J. Phys. Chem. A* **1956**, *60*, 677–678.

(142) Andersen, O. K.; Pawlowska, Z.; Jepsen, O. *Phys. Rev. B Condens. Matter Mater. Phys.* **1986**, *34*, 5253–5269.

(143) Lambrecht, W. R. L.; Andersen, O. K. *Phys. Rev. B* **1986**, *34*, 2439.

(144) Blöchl, P. E.; Jepsen, O.; Andersen, O. K. *Phys. Rev. B* **1994**, *49*, 16223.

(145) *Chemistry, Structure and Bonding of Zintl Phases and Ions*; Kauzlarich, S. M., Ed.; VCH Publishers: New York, 1996.

(146) Tao, X.; Jund, P.; Colinet, C.; Tedenac, J.-C. *Phys. Rev. B* **2009**, *80*, 1–10.

(147) Kolotun, V. F.; Mima, L. S. Naukova Dumka, 1976; p. 158.

(148) Neshpor, V. S.; Samsonov, G. V. *Fiz. Tverd. Tela* **1960**, *2*, 2202–2209.

(149) Bondarev, V. N.; Podergin, V. A.; Grechko, O. G.; Perminov, V. P. Kornilov, A. A., Ed.; Nauka, 1972; p. 65.

(150) Cruceanu, E.; Popa, M.; Ivanciu, O. *Rev. Roum. Phys.* **1976**, *21*, 771–773.

(151) HARRIS, I. R.; MANSEY, R. C.; RAYNOR, G. V. *J. Less-Common Met.* **1965**, *9*, 270.

(152) Duc, N. H.; Hien, T. D.; Brommer, P. E.; Franse, J. J. M. *J. Magn. Magn. Mater.* **1992**, *104–107*, 1252–1256.

(153) Bash, E. *J. Less-common Met.* **1968**, *14*, 329–336.

(154) Singh, N. K.; Suresh, K. G.; Nigam, A. K.; Malik, S. K.; Coelho, A. A.; Gama, S. *J. Magn. Magn. Mater.* **2007**, *317*, 68–79.

(155) Gratz, E.; Markosyan, A. S. *J. Phys. Condens. Matter* **2001**, *13*, 385–413.

(156) SEARS, V. F. *Neutron News* **1992**, *3*, 29–37.

(157) Carvajal-Rodríguez. *J. Phys. B* **1993**, *192*, 55−69.

(158) Oesterreicher, H.; Corliss, L. M.; Hastings, J. M. *J. Appl. Phys.* **1970**, *41*, 2326.

(159) Yakinthos, J. K. *Conf. Ser. - Inst. Phys.* **1978**, *37*, 315–318.

(160) Katsuraki, H.; Yoshii, S. *J. Phys. Soc. Japan* **1968**, *24*, 1171–1172.

(161) Mann, J. B.; Meek, T. L.; Allen, L. C. *J. Am. Chem. Soc.* **2000**, *122*, 2780–2783.

(162) Mann, J. B.; Meek, T. L.; Knight, E. T.; Capitani, J. F.; Allen, L. C. *J. Am. Chem. Soc.* **2000**, *122*, 5132–5137.